Centro de Investigaciones en Óptica, A.C.

División de Fotónica

Loma del Bosque 115, León, Guanajuato, 37150, México

# Optical response in semiconductors

by

José Luis Cabellos Quiroz

A thesis submitted in partial fulfillment of the requirements for the degree of Doctor of Science (Optics).

Supervisor:
Dr. Bernardo Mendoza Santoyo

December 15, 2009

*I think I can safely say that nobody understand quantum mechanics.*

Richard P. Feynman

# Dedication

---

To my parents: Amada Quiroz Ocón and Felix Cabellos Tejeda

---

# Acknowledgements

A lot of people have been helping me in this research then I am afraid I could forget to mention somebody. First of all I would like to acknowledge to my supervisor Dr. Bernardo Mendoza Santoyo for his invaluable teaching, advice, guidance and support without that, this thesis could not have been accomplished. I would like to thank him for all arrangements that make me possible to visit the University of Toronto, on summer 2005. Also I would like to thank Professor John Sipe and doctoral student Fred Nastos from the Department of Physics of the University of Toronto.

I would also like to thank Dr. Norberto Arzate Plata and Dr. Raúl Alfonso Vázquez Nava for many fruitful discussions in physics and support with the computing aspects which were very important for the well ending of this thesis.

I would like to thank Dr. Rafael Espinoza Luna for his support and advice in hard times.

I would like to thank Dr. Brenda Esmeralda Martínez Zérega, Professor Mario Alberto Ruíz Berganza and Dr. Luis Armando Díaz Torres for their support and advice during my stay at the Centro de Investigaciones en Óptica, A.C.

I would like to thank Dr. Cesar Castillo Quevedo from Universidad de Guadalajara for all his interest in my professional success and his support in hard times.

I would like to thank M. en C. Juan Cuauhtémoc Salazar González with whom I shared the office, and discussed topics in physics and beyond, I thank him for his help and support in hard times, the office will never be the same without him.

I am specially grateful to M. en C. Noé González Baquedano for his help and support in hard times.

I would like to thank Lic. Guillermina Muñiz Palancares and Lic. Laura González Ochoa for all their help since I arrived to this institution.

I would like to thank all my classmates Haggeo De Sirena, Cornelio Alvarez, Mauricio Flores, Claudio Ramírez and Trinidad Guillen with whom I shared problems and discuss topics in physics.

I would like to thank Sra. Carmen Ortiz Mendez for all her help.

I would like to express special gratitude to my mother, father and all my siblings, specially to Angel, Edelmira, Felix and his wife Estella Velasco for encouraging me to study, without their help this would have been almost impossible.

I acknowledge the economic support of Consejo Nacional de Ciencia y Tecnología under scholarship number 143220.

# Abstract

In this thesis we present an *ab initio* study of the optical response in bulk semiconductors and their surfaces using the local density approximation to the density functional theory under the approach of pseudopotentials and all-electron schemes.

In the first part of the thesis we present a study of the nonlocal effects in the optical response due the use of density functional theory within local density approximation and the errors introduced by the use of pseudopotentials. We obtain the linear and nonlinear optical susceptibility tensors including the *scissors approximation* within the formalisms of velocity-gauge and length-gauge by solving the density matrix equation of motion and using a perturbative technique. These two formalisms are equivalent and they are related by a gauge transformation. When the calculation is done under the velocity-gauge formalism, we show that new terms coming from the nonlocal scissors correction appear. These terms, not considered before in the literature, are crucial in order to obtain gauge invariance.

In the second and third part of the thesis we present the study of the optical injection of electric current and the optical injection of spins, for several semiconductor surfaces. We present new expressions that describe both phenomena that take into account the layer-by-layer contribution of any surface.

The last part of this work is devoted to the study of optical spin injection in stressed bulk Si and bulk GaAs. This is of great technological importance since Si is nowdays the quintessential semiconductor of the electronic industry. It is shown that one can inject up to 75% of spins with the appropriate stress. This means that Si could be used to build spintronic devices.

# Contents


**1 Introduction** **1**

1.1 Nonlocal effects of the scissors operator . . . 2
1.2 Optical injection current . . . 3
1.3 Optical spin injection . . . 4
1.4 Organization of this thesis . . . 4

**2 Gauge invariance** **5**

2.1 Summary . . . 5
2.2 Introduction . . . 6
2.3 Theory . . . 8
2.3.1 Perturbation approach . . . 8
2.3.2 Velocity gauge formalism . . . 10
2.3.3 Length gauge formalism . . . 20
2.4 Results . . . 22
2.5 Conclusions . . . 27
2.6 Appendix . . . 29

**3 Optical injection current at semiconductor surfaces** **33**

3.1 Summary . . . 33
3.2 Introduction . . . 34
3.3 Theory . . . 36
3.4 Computational details . . . 41
3.5 Results . . . 42
3.5.1 Si(111) surfaces . . . 44
3.5.2 GaAs(110) surfaces . . . 45
3.5.3 Surface vs. bulk experimental detection estimate . . . 46
3.6 Conclusions . . . 47
3.7 Appendix . . . 48

**4 Optical spin injection at semiconductor surfaces** **55**

4.1 Summary . . . 55
4.2 Introduction . . . 56
4.3 Theory . . . 57
4.3.1 Surface responses . . . 61

4.4 Computational details . . . . . 63
4.5 Results . . . . . 65
4.6 Conclusions . . . . . 73

**5 Stress modulated optical spin-injection** **75**
5.1 Summary . . . . . 75
5.2 Introduction . . . . . 75
5.3 Theory . . . . . 76
5.4 Results . . . . . 78
5.5 Conclusions . . . . . 85

**6 General conclusions** **87**

**A Curriculum Vitae** **89**

**Bibliography** **91**

# List of Figures


2.1 $\chi^{xyz}_{\mathrm{v},L}(-2\omega;\omega,\omega)$ for the length and the velocity gauge schemes. 25
2.2 Comparison of different formulas for $\chi^{xyz}(-2\omega;\omega,\omega)$. . . . . . . 26
2.3 All-electron vs. pseudopotential $|\chi^{xyz}(-2\omega;\omega,\omega)|$. . . . . . . . 27
2.4 Theoretical vs. experimental $|\chi^{xyz}(-2\omega;\omega,\omega)|$. . . . . . . . . . 28

3.1 Top and side views of the studied surfaces for current injection 42
3.2 $\eta_2^{(S,\ell),yyx}(0;\omega,-\omega)$ for the clean Si(111)(2 $\times$ 1) surface. . . . . . 43
3.3 $\eta_2^{S,yyx}(0;\omega,-\omega)$ vs. $N$. . . . . . . . . . . . . . . . . . . . . . . 44
3.4 $\eta_2^{(S,\ell),yyx}(0;\omega,-\omega)$ for the clean and Sb-covered GaAs(110) surfaces. . . . . . . . . . . . . . . . . . . . . . . . . . . . . . . 46

4.1 Top and side views of the studied surfaces for spin injection. . . 66
4.2 $\tilde{\zeta}^{\ell,\mathrm{zxy}}(\omega)$ and $\hbar\tilde{\xi}^{\ell,\mathrm{xx}}(\omega)$ for the As-terminated Si(111) surface. . 68
4.3 $\zeta^{\ell,\mathrm{zxy}}(\omega)$ for the H-covered Si(111) surface. . . . . . . . . . . . 69
4.4 $\mathcal{D}^{\mathrm{z}}_s(\omega)$ for the clean Si(111) surface. . . . . . . . . . . . . . . . . 70
4.5 $\mathcal{D}^{S,\mathrm{z}}(\omega)$ for the As-covered Si(111) surface. . . . . . . . . . . . . 71
4.6 $\mathcal{D}^{S,\mathrm{z}}(\omega)$ for the In-covered Si(111) surface. . . . . . . . . . . . . 72
4.7 Analysis of $\zeta^{S,\mathrm{zxy}}(\omega)$. . . . . . . . . . . . . . . . . . . . . . . . 73

5.1 $\mathcal{D}^{\mathrm{z}}$ vs. stress for bulk silicon. . . . . . . . . . . . . . . . . . . . 79
5.2 $\zeta^{\mathrm{zxy}}(\omega)$ and $\hbar\xi(\omega)$ for Si. . . . . . . . . . . . . . . . . . . . . . . 80
5.3 $\mathcal{D}^{\mathrm{z}}$ for GaAs. . . . . . . . . . . . . . . . . . . . . . . . . . . . 81
5.4 Analysis of $\zeta^{\mathrm{zxy}}(\omega)$. . . . . . . . . . . . . . . . . . . . . . . . . 82
5.5 Energy bands for Si and GaAs. . . . . . . . . . . . . . . . . . . . 84

# List of Tables

2.1 Parameters used in the SHG calculation. . . . . . . . . . . . . . . 23

3.1 Number of atomic layers and scissors correction. . . . . . . . . . . 47

4.1 Convergence parameters of the DSP at surfaces. . . . . . . . . . . 64
4.2 Non-zero components of $\zeta^{\ell,\mathrm{abc}}(\omega)$. . . . . . . . . . . . . . . . . . . 65

Chapter 1

# Introduction

## Contents


**1.1 Nonlocal effects of the scissors operator . . . . . . . . . 2**
**1.2 Optical injection current . . . . . . . . . . . . . . . . . . . . 3**
**1.3 Optical spin injection . . . . . . . . . . . . . . . . . . . . . 4**
**1.4 Organization of this thesis . . . . . . . . . . . . . . . . . . 4**


A semiconductor can be characterized using its response when we apply a external stimulus, for example an electronic circuits can be characterized by using its output voltage when we apply an input voltage, the resulting function is known as transfer function, this function provides all the information that is needed to understand the circuit.

In a crystalline semiconductor the same thing happens, the crystal semiconductor can be characterized using its response function. The question that arises is how the crystal behave under external influence or stimuli? The disturbance could be electrical fields , magnetic fields, temperature, light, etc. If the stimulus is light, the absorption, reflection and dispersion give us information about the interaction of the electromagnetic wave with the semiconductor. Examining the effects of the stimuli it is possible to determine the properties of the semiconductor.

In this scheme the input could be an electromagnetic field and the output would be the electric polarization of the semiconductor. The response is known as the susceptibility, $\chi$, and it contains the information needed to determine the optical properties of the semiconductor. In general we can write

$$\mathbf{P} = \chi^{(1)} \cdot \mathbf{E} + \chi^{(2)} : \mathbf{EE} + \chi^{(3)} \vdots \mathbf{EEE} + \ldots \tag{1.1}$$

where $\chi^{(1)}$ is the linear susceptibility tensor, $\chi^{(2)}$ is the second order susceptibility tensor, which describes processes such as second harmonic generation, and $\chi^{(3)}$ is the third order susceptibility tensor which describes processes as third

harmonic generation and the intensity-dependent refractive index. In equation above **P** is the polarization and **E** is the applied electric field. Depending on the strength of the electromagnetic field the polarization will depend either linearly or non-linearly on the applied electromagnetic field. In this thesis the electromagnetic field will be treated as a classical field and the material system will be treated quantum mechanically.

The general goal of this thesis is the development of quantum mechanical expressions for $\chi^{(1)}$ and $\chi^{(2)}$, and two other optical responses. The first is the spin tensor $\zeta$, associated to the first order response, and the second one is the current injection tensor, $\eta_2$, related to second-order response. The interest in studying nonlinear optical susceptibilities is that they can be used to obtain information about reconstructions of surface semiconductors, electronic energy levels, surface states, etc. But more importantly, these effects could be used to coherently manipulate the spin of the electron and the electronic current.

## 1.1 Nonlocal effects of the scissors operator

As it is well known in the literature, one of the main failures of the density functional theory (DFT), within the local density approximation (LDA), is the underestimation of the band gap. The Schrödinger equation within the one-electron approximation contains a self-energy term that describes the many-body interactions. The solution to such equation is an ongoing theoretical and numerical challenge. Within LDA one neglects such many-body effects and this leads to the band gap miscalculation. The solution of the self-energy term is known to lead to the calculation of the energy gap in agreement with the experimental values. To first order, the many body effects are introduced through the so call "GW" approximation, where "G" stands for the electron Green function and "W" for the screened Coulomb interaction. The GW solution produces electron wavefunctions that are very similar to the LDA wavefunctions, and conduction energy bands that have the same dispersion in the Brillouin zone as the LDA bands. However, the GW conduction bands are shifted upwards in energy almost rigidly with respect to the LDA bands in such a way that the GW gap is very similar to the experimental gap. The problem is that the GW scheme is computationally very demanding and for our purposes is not feasible. To overcome this, the so-called *scissors approximation* is widely used. Within this approximation the conduction bands are rigidly shifted in energy so the energy gap matches the experimental value. Thus, the formulation of linear and nonlinear optical susceptibility with and

without the scissors approximation and under the formalisms of velocity-gauge and length-gauge, is the first goal of this thesis. The expressions for $\chi^{(1)}$ and $\chi^{(2)}$ are obtained by solving the density matrix equation of motion and using a perturbative technique. We show that new terms, not considered before in the literature, appear when the calculation is done under the velocity-gauge and that these terms are crucial for gauge invariance.

## 1.2 Optical injection current

The generation of currents in semiconductor surfaces is studied. There are basically three types of currents that can be generated with photo-excitation: rectification, shift and injection current. Optical generation and control of currents in semiconductors can be described within the standard framework of nonlinear optics using susceptibilities. In general $\chi^{(2)}$ can be written as the sum of a non-divergent term and two diverging terms as

$$\begin{aligned}\chi^{(2)}(-\omega_D;\omega_1,-\omega_2) &= \chi_R^{(2)}(-\omega_D;\omega_1,-\omega_2) \\ &+ \frac{\sigma_2(-\omega_D;\omega_1,-\omega_2)}{-i\omega_D} \\ &+ \frac{\eta_2(-\omega_D;\omega_1,-\omega_2)}{(-i\omega_D)^2},\end{aligned} \tag{1.2}$$

where the $\omega_1$ and $\omega_2$ are the frequencies of the excitation optical pulses and $\omega_D = \omega_1 - \omega_2$. $\chi_R^{(2)}$ is rectification current tensor, $\sigma_2$ is the shift current tensor and $\eta_2$ the injection current tensor. The last two terms in Eq. (1.2) diverge as $\omega_D \to 0$. In this thesis we are interested in $\eta_2$ which originates from the quantum interference between absorption pathways associated with orthogonal components of the beam polarization. A study of optical coherent control of injection currents at surfaces of cubic semiconductors is presented. To obtain the surface contribution to $\eta_2$ a formalism that allows to get the "layer-by-layer" response also is presented. This optical effect will serve as a surface sensitive probe of crystals with bulk inversion symmetry or $\bar{6}m2$, $\bar{6}$, and $\bar{4}\bar{3}m$ (zinc-blende) symmetry. In crystals with any of these symmetries, this effect vanishes in bulk, but it is allowed in the surface region owing to the local break of symmetry. We present the results of *ab initio* calculations for injected currents at prototypical Si and GaAs surfaces, hydrogenated and As-covered Si(111)$(1\times1)$, clean Si(111)$(2\times1)$, as well as clean and Sb-covered GaAs(110)$(1\times1)$. The effects are shown to be sensitive to the surface structure and these effects should be experimentally mesurable.

## 1.3 Optical spin injection

Spin is a quantum mechanical property associated with the intrinsic angular momentum of many elementary particles. In particular for the electrons, it explains magnetism in matter. Electron spin can have two possible values: $1/2$ and $-1/2$; they are colloquially refered to as “spin up” and “spin down”. This dichotomy between the values of the spin is the basis of the emerging field of spintronics, which is a new branch of electronics where the spin degree of freedom is controlled to carry information. Thus, information can be encoded via electron spin, and transported from one part of the device to another using electron currents. In order to build a useful device, the field of spintronics has three main challenges: spin injection, spin transport and spin detection. Spin injection in semiconductors can be optically or electrically achieved. In this thesis only optical spin injection will be presented, which is produced by the use of circularly polarized light. A previously introduced formalism to study optically injected spins in stressed bulk semiconductors is used, like Si and GaAs, and extend the theoretical formalism to study optical spin injection at the surfaces of semiconductors. This extension is similar to the layer-by-layer scheme developed for the injection current. For the surfaces we study optical spin-injection at several Si(111) and GaAs(110) surfaces. The theoretical results predict that both semiconductor surfaces are good candidates to be used for optical injection of spins. Thus the quintessential element of the electronic industry, bulk Si, and its surfaces, could be a good choice to be used for spintronic devices.

## 1.4 Organization of this thesis

This thesis is organized as follows: Chapter 2 presents a formal derivation of the linear and nonlinear response with and without the scissors approximation in bulk semiconductors using both length-gauge and velocity-gauge formalism; Chapter 3 is devoted to the study of current injection in semiconductor surfaces; Chapters 4 and 5 are dedicated to the study of optical spin injection in surfaces and bulk, respectively, and in Chapter 6 the general conclusions of the thesis are given.

Chapter 2

# Gauge invariance

## Contents


**2.1 Summary** . . . . . . . . . . **5**

**2.2 Introduction** . . . . . . . . . . **6**

**2.3 Theory** . . . . . . . . . . **8**

2.3.1 Perturbation approach . . . . . . . . . . 8

2.3.2 Velocity gauge formalism . . . . . . . . . . 10

2.3.3 Length gauge formalism . . . . . . . . . . 20

**2.4 Results** . . . . . . . . . . **22**

**2.5 Conclusions** . . . . . . . . . . **27**

**2.6 Appendix** . . . . . . . . . . **29**


## 2.1 Summary


Calculations of the second harmonic susceptibility tensor $\chi^{abc}(-2\omega;\omega,\omega)$ are presented for bulk semiconductors within both the velocity and the length gauge. The description of the semiconductor states incorporates the "scissors" Hamiltonian commonly used to obtain the correct band gap. The non-locality of the scissors correction leads to additional terms in $\chi^{abc}(-2\omega;\omega,\omega)$ that were not considered before within a sum-over-states approach in the velocity gauge. Using this new expression, we show that the calculations of $\chi^{abc}(-2\omega;\omega,\omega)$ with both gauges match within very good numerical accuracy.[1] As part of the derivation, we clarify the well known result for the linear optical response, which states that the scissors correction rigidly shifts the spectrum along the energy axis, keeping the line-shape intact. The calculation for GaAs is presented using an *all-electron* and a *pseudopotential* scheme.


[1] 1 part in approximately $10^5$

## 2.2 Introduction

The development of new nonlinear optical materials is an active area of research, with works ranging from the study and growth of new nonlinear crystals to the design of novel metamaterials. Perhaps the simplest nonlinear process, second harmonic generation (SHG), is one of the most used for generation of new frequencies, as a spectroscopic probe, and because its reverse process, spontaneous parametric downconversion, which is described by the same nonlinear susceptibility, it can be used to generate entangled photons for application in quantum information processing.

The numerical calculation of any nonlinear optical response is a nontrivial task, and different methodologies and numerical approaches have been employed. Our interest is focused in strategies that can be applied to study the nonlinear optical response of a material over a wide frequency range, and in a regime where a perturbative treatment is appropriate. The first attempt along this line is the work of Butcher and McLean [BM63], where the resulting equations appeared to be plagued of divergences that appear in the DC (static) limit. Aspnes [Asp72] showed that, in the static limit, these divergences are only apparent, since the coefficients that multiply the divergent terms vanish; however his proof was only limited to cubic crystals. Ghahramani, Moss and Sipe [GMS91], gave a more general proof of the disappearance of these apparent divergences for cold ($T = 0$ K), undoped semiconductors of any crystal class. Levine [Lev94], presented a formula for the nonlinear second order susceptibility tensor where the scissors approximation is properly introduced, unfortunately the expressions are difficult to compute. These studies used what is called the “velocity gauge” or “$\mathbf{v}\cdot\mathbf{A}$ gauge” for the treatment of the coupling of an electron to the electromagnetic field, where $\mathbf{v}$ is the velocity operator of the electron and $\mathbf{A}$ is the vector potential specifying the electromagnetic field. Later, Aversa and Sipe [AS95] showed that a divergence free expression for the nonlinear second order susceptibility tensor $\chi^{abc}(-2\omega;\omega,\omega)$ could be more easily obtained by using what is called the “length gauge” or “$\mathbf{r}\cdot\mathbf{E}$ formulation”. Here $\mathbf{r}$ is the position operator and $\mathbf{E}$ is the electric field.

In the works of Rashkeev et al. [RLS98], and Hughes and Sipe [HS96], the length-gauge formulation was used to evaluate $\chi^{abc}(-2\omega;\omega,\omega)$ for several zinc-blende semiconductors within an *ab initio* scheme. The more recent work of Leitsmann et al. [LSHB05], extends the velocity-gauge approach to include excitonic and local field interactions in GaAs. Quasi-particle effects, at the scissors correction level, have been correctly incorporated by Nastos

et al. [NOSS05] in the length-gauge approach. Before this Adolph and Bechstedt [AB98] discussed how to include these effects, even beyond the scissors approximation, within the velocity-gauge approach. Surface second harmonic generation has also been studied within the velocity-gauge scheme with success fully [MPODS01, MGDS98, RDSCP94], and $\chi^{abc}(-2\omega;\omega,\omega)$ spectra have been calculated for superlattices within both the length-gauge approach [SDAD03] and the velocity-gauge approach [GMS91].

A full comparison between calculations using these two different approaches has not been done. One goal of this chapter is to establish the equivalence between the length-gauge and velocity-gauge schemes. It is well known that measurable quantities must be gauge invariant. We thus show in this chapter that the expressions for $\chi^{abc}(-2\omega;\omega,\omega)$ evaluated through these two different approaches lead to the same result. In order to do so, we derive a new expression for $\chi^{abc}(-2\omega;\omega,\omega)$ within the velocity-gauge, that properly takes into account the non-local nature of the scissors Hamiltonian. In all previous calculations of $\chi^{abc}(-2\omega;\omega,\omega)$, within the velocity-gauge, the scissors implementation was carried out by following the same method used for the linear optical response. It can be shown that this naïve procedure, of shifting the conduction energies and renormalizing the velocity matrix elements, which works for the linear response, does not work properly for the nonlinear response. The new expression derived for $\chi^{abc}(-2\omega;\omega,\omega)$ contains two terms directly obtained from the scissors Hamiltonian that are clearly required to obtain gauge invariance within the scissors implementation. Earlier, Nastos et al. [NOSS05] showed the correct way of calculating $\chi^{abc}(-2\omega;\omega,\omega)$ using the scissors Hamiltonian within the length-gauge. In this chapter a unified approach to $\chi^{abc}(-2\omega;\omega,\omega)$, is presented with and without the scissors correction, that matches for the velocity-gauge and length-gauge. While we can verify this analytically for the linear response [AS95], for the SHG response coefficient this could only be confirmed numerically. Nonetheless, with this confidence acquired our approach can serve as a model for the gauge-invariant calculation of other nonlinear optical response coefficients.

The chapter is organized as follows. In Section 2.3 we present the most important steps involved in the derivation of second order susceptibility tensor $\chi^{abc}(-2\omega;\omega,\omega)$, within the length-gauge and velocity-gauge approaches. In Section 2.4 we show the results of the numerical evaluation of $\chi^{abc}(-2\omega;\omega,\omega)$, taking as an example the zinc-blende bulk semiconductor GaAs, and discuss them. We calculate the expressions for $\chi^{abc}(-2\omega;\omega,\omega)$ with *ab initio* programs based on Density Functional Theory within the Local Density Approximation

(DFT-LDA), using all-electron and pseudopotential schemes.

## 2.3 Theory

In this section we present the strategy used to calculate the second-order nonlinear response. Although this has already been discussed in earlier studies, we consider both the velocity gauge and the length gauge response within a common formalism. this derivation includes new terms not included before in the velocity gauge, for both the linear and the nonlinear response. For the nonlinear response, the new terms are crucial for establishing numerically that both gauges give the same result.

### 2.3.1 Perturbation approach

We use the independent particle approximation, neglect both the local field and the excitonic effects, and treat the electromagnetic field classically, while the matter is described quantum-mechanically. We can describe the system using a scaled one electron density operator $\rho$, with which we can calculate the expectation value of a single-particle observable $\mathcal{O}$ as $\langle\mathcal{O}\rangle = \mathrm{Tr}(\rho\mathcal{O})$, with $\mathcal{O}$ the associated quantum mechanical operator and Tr the trace. The density operator satisfies $i\hbar(d\rho/dt) = [H(t), \rho]$, with $H(t)$ as the total single electron Hamiltonian, written as

$$H(t) = H_0 + H_I(t),$$

where $H_0$ is the unperturbed time-independent Hamiltonian, and $H_I(t)$ is the time-dependent potential energy due to the interaction of the electron with the electromagnetic field; $H_0$ has eigenvalues $\hbar\omega_n(\mathbf{k})$ and eigenstates $|n\mathbf{k}\rangle$ (Bloch states) labeled by a band index $n$ and crystal momentum $\mathbf{k}$. To proceed with the solution of $\rho$ it is convenient to use the interaction picture, where a unitary operator $U = \exp(iH_0t/\hbar)$ transforms any operator $\mathcal{O}$ into $\tilde{\mathcal{O}} = U\ \mathcal{O}U^\dagger$. Even if $\mathcal{O}$ does not depend on $t$, $\tilde{\mathcal{O}}$ does through the explicit time dependence of $U$. The dynamic equation for $\tilde{\rho}$ is given by

$$i\hbar\frac{d\tilde{\rho}}{dt} = [\tilde{H}_I(t), \tilde{\rho}],$$

with solution

$$i\hbar\tilde{\rho}(t) = i\hbar\tilde{\rho}_0 + \int_{-\infty}^{t} dt'[\tilde{H}_I(t'), \tilde{\rho}(t')], \tag{2.1}$$

where $\tilde{\rho}_0 = \tilde{\rho}(t = -\infty)$ is the unperturbed density matrix. We look for the standard perturbation series solution, $\tilde{\rho}(t) = \tilde{\rho}^{(0)} + \tilde{\rho}^{(1)} + \tilde{\rho}^{(2)} + \cdots$, where the superscript denotes the order (power) with which each term depends on the perturbation $H_I(t)$. From Eq. (2.1) the $N$-th order term is

$$\tilde{\rho}^{(N)}(t) = \frac{1}{i\hbar}\int_{-\infty}^{t} dt'[\tilde{H}_I(t'), \tilde{\rho}^{(N-1)}(t')]. \tag{2.2}$$

The series is generated by the unperturbed density operator $\tilde{\rho}^{(0)} \equiv \tilde{\rho}_0$, assumed to be the diagonal Fermi-Dirac distribution, $\langle n\mathbf{k}|\tilde{\rho}_0|n\mathbf{k}\rangle = f(\hbar\omega_n(\mathbf{k})) \equiv f_n$. For a clean, cold semiconductor, $f_n = 1$ for $n$ a valence ($v$) or occupied band, and $f_n = 0$ for $n$ a conduction ($c$) or empty band. We will use this assumption throughout.

The expectation value of the macroscopic current density $\mathbf{J}$ is given by

$$\langle\mathbf{J}\rangle = \frac{e}{\Omega}\mathrm{Tr}(\rho\dot{\mathbf{r}}), \tag{2.3}$$

where $\dot{\mathbf{r}}$ is the time derivative of the position operator of an electron of charge $e$. The velocity operator of the electron is given by

$$\mathbf{v} \equiv \dot{\mathbf{r}} = \frac{1}{i\hbar}[\mathbf{r}, H], \tag{2.4}$$

with $\Omega$ the normalization volume. The macroscopic polarization density $\mathbf{P}$ is related to $\langle\mathbf{J}\rangle$ by $\langle\mathbf{J}\rangle = d\mathbf{P}/dt$. For a perturbing (Maxwell macroscopic) electromagnetic field, $\mathbf{E}(t) = \mathbf{E}(\omega)e^{-i\tilde{\omega}t} + c.c.$, where $\tilde{\omega} = \omega + i\eta$, and $\eta > 0$ is used to adiabatically turn on the interaction. We write the second order nonlinear polarization as,

$$P^{a(2)}(2\omega) = \chi^{abc}(-2\omega;\omega,\omega)E^b(\omega)E^c(\omega), \tag{2.5}$$

where $\chi^{abc}(-2\omega;\omega,\omega)$ is the second order susceptibility. The superscripts in Eq. (2.5) denote Cartesian components, if repeated are to be summed over. Without loss of generality we can always define $\chi^{abc}(-2\omega;\omega,\omega)$ to satisfy intrinsic permutation symmetry, $\chi^{abc}(-2\omega;\omega,\omega) = \chi^{acb}(-2\omega;\omega,\omega)$; if it does not, the part that does not satisfy the intrinsic permutation symmetriy would make no contribution to the second order polarization. This part could be dropped since it would have no physical significance.

The unperturbed Hamiltonian is given by

$$H_0 = \frac{p^2}{2m_e} + V(\mathbf{r}), \tag{2.6}$$

with $m_e$ the mass of the electron, $\mathbf{p}$ its canonical momentum, and $V(\mathbf{r})$ the local periodic crystal potential, where we neglect spin-orbit terms. This Hamiltonian is used to solve the Kohn-Sham equations [KS65] of DFT, within the LDA. The use of these solutions as single particle states leads to an underestimation of the band gap. A standard procedure to correct this is to use the so-called "scissors approximation", by which one rigidly shifts the conduction bands in energy so that the band gap value corresponds to the experimental one; this value is often in fairly good agreement with the GW[2] band gap based on a more sophisticated calculation [HL86]. Concurrently, one uses the LDA wave functions, since they produce band structures with dispersion relations similar to those predicted by the GW approximation. Mathematically, one adds the scissors (non-local) term $S(\mathbf{r}, \mathbf{p})$, to the unperturbed or unscissored Hamiltonian $H_0$, i.e.

$$H_0^S = H_0 + S(\mathbf{r}, \mathbf{p}),$$

where

$$S(\mathbf{r}, \mathbf{p}) = \hbar\Delta \sum_n \int d^3k(1 - f_n)|n\mathbf{k}\rangle\langle n\mathbf{k}|, \tag{2.7}$$

with $\hbar\Delta$ the rigid ($\mathbf{k}$-independent) energy correction to be applied, and $f_n$ is occupation factor taken to be one for occupied bands and zero for unoccupied bands, the underlying physics that this operator describe is shift only the conduction band energies when it operate over all conductions and valence states. Several properties of $S(\mathbf{r}, \mathbf{p})$ are shown in the appendix. The unscissored and scissored Hamiltonians satisfy respectively the relations:

$$\begin{aligned} H_0\psi_{n\mathbf{k}}(\mathbf{r}) &= \hbar\omega_n(\mathbf{k})\psi_{n\mathbf{k}}(\mathbf{r}), \\ H_0^S\psi_{n\mathbf{k}}(\mathbf{r}) &= \hbar\omega_n^S(\mathbf{k})\psi_{n\mathbf{k}}(\mathbf{r}), \end{aligned}$$

where

$$\omega_n^S(\mathbf{k}) = \omega_n(\mathbf{k}) + (1 - f_n)\Delta, \tag{2.8}$$

and $\psi_{n\mathbf{k}}(\mathbf{r}) = \langle\mathbf{r}|n\mathbf{k}\rangle$ is the coordinate representation of the ket $|n\mathbf{k}\rangle$.

### 2.3.2 Velocity gauge formalism

To calculate the optical response in the velocity gauge, we use the minimal substitution through which, in the presence of an electromagnetic field, the Hamiltonian is written as

$$H^S = \frac{1}{2m_e}(\mathbf{p} - \frac{e}{c}\mathbf{A})^2 + V(\mathbf{r}) + S(\mathbf{r}, \mathbf{p} - \frac{e}{c}\mathbf{A}), \tag{2.9}$$

[2] *One Particle Green Function (G) with Screened Coulomb Interaction (W)*

where $\mathbf{A}$ is the vector potential; one obtains the magnetic field as $\mathbf{B} = \nabla \times \mathbf{A}$ and the electric field as $\mathbf{E} = -(1/c)\dot{\mathbf{A}}$, with $c$ the speed of light in vacuum. In general these electric and magnetic fields are taken to be the macroscopic Maxwell fields. We assume the long-wavelength limit, in which $\mathbf{A}$ is uniform and only depends on time. Furthermore, we take a harmonic perturbation of the form $\mathbf{A}(t) = \mathbf{A}(\omega)e^{-i\tilde{\omega}t} + \mathbf{A}^*(\omega)e^{i\tilde{\omega}^*t}$, where only the "positive frequency" term will be kept in the following calculations. Expanding the scissors operator according to [NOSS05],

$$S(\mathbf{r}, \mathbf{p} - \frac{e}{c}\mathbf{A}) = S(\mathbf{r}, \mathbf{p}) + \frac{e}{c}\frac{i}{\hbar}\mathbf{A}\cdot[\mathbf{r}, S(\mathbf{r}, \mathbf{p})] + \frac{1}{2!}\left(\frac{e}{c}\frac{i}{\hbar}\right)^2 [\mathbf{A}\cdot\mathbf{r}, [\mathbf{A}\cdot\mathbf{r}, S(\mathbf{r}, \mathbf{p})]] + \cdots ,$$

leads to the following scissored Hamiltonian up to second order in $\mathbf{A}$

$$H^S = H_0^S + H_{I,1} + H_{I,2},$$

where

$$H_{I,1} = -\frac{e}{c}\mathbf{A} \cdot \mathbf{v}^{\Sigma}, \tag{2.10}$$

$$H_{I,2} = -\frac{ie^2}{2\hbar c^2}[r^b, v^{S,c}]A^b A^c + \frac{e^2}{2m_e c^2}A^2, \tag{2.11}$$

are the linear and nonlinear (second order) interaction Hamiltonians. The last term in Eq. 2.11 is only a function of time. It contributes to a global phase factor of the electron wave function which has no effect on expectation values. Therefore it can be neglected. We have defined

$$\mathbf{v}^S = -\frac{i}{\hbar}[\mathbf{r}, S(\mathbf{r}, \mathbf{p})], \tag{2.12}$$

as the contribution to the velocity operator due to the non-local scissors term, and

$$\mathbf{v}^{\Sigma} = \frac{\mathbf{p}}{m_e} + \mathbf{v}^S, \tag{2.13}$$

as the scissored velocity operator. From Eq. (2.4) the current operator $\mathbf{j} = e\dot{\mathbf{r}}$, up to second order in $\mathbf{A}$, is

$$j^a = j_0^a + j_1^a + j_2^a,$$

with

$$j_0^a = ev^{\Sigma,a},$$

$$j_1^a = -\frac{e^2}{cm_e}A^a + \frac{ie^2}{\hbar c}[r^a, v^{S,b}]A^b,$$

$$j_2^a = -\frac{e^3}{2\hbar^2 c^2}[r^a, [r^b, v^{S,c}]]A^b A^c,$$

being the operators of zero, first and second order in $\mathbf{A}$, respectively. From Eq. (2.3), we have that

$$\langle J^{(1)a}\rangle = \frac{1}{\Omega}\mathrm{Tr}(j_0^a\rho^{(1)}) + \frac{1}{\Omega}\mathrm{Tr}(j_1^a\rho^{(0)}) \tag{2.14}$$

is the linear macroscopic current density, and

$$\langle J^{(2)a}\rangle = \frac{1}{\Omega}\mathrm{Tr}(j_0^a\rho^{(2)}) + \frac{1}{\Omega}\mathrm{Tr}(j_1^a\rho^{(1)}) + \frac{1}{\Omega}\mathrm{Tr}(j_2^a\rho^{(0)}) \tag{2.15}$$

is the nonlinear (second order) macroscopic current density.

#### 2.3.2.1 Linear response

In this section the linear response is calculated, within the velocity gauge, and it is shown that there is a new term not previously included when the scissored Hamiltonian is used. Indeed, we show that by chance the "usual" way of including the scissor correction leads to the correct result. That is, the scissors correction only gives a rigid shift in the energy axis of the unscissored spectrum by an amount equal to $\Delta$; the line shape of the spectrum is the same for both the scissored and the unscissored Hamiltonians [NOSS05, DSG93, LA91, LA89]. In the following, we show that if the usual procedure is used for the nonlinear response the resulting scissored susceptibility is wrong. The derivation of the linear response here is important for making sense of our later results, and also sets some of the intermediate results that will be used in the calculation of the nonlinear response. Aditionally we also show that the linear response is gauge invariant, since we obtain the same analytic result for the linear susceptibility in both gauges. This agreement holds with and without the scissors correction.

Lets start by taking matrix elements of Eq. (2.2) leads to

$$\tilde{\rho}_{mn}^{(1)}(t) = \frac{ei}{\hbar c}\int_{-\infty}^{t} dt' A^b(t')\sum_{\ell}\left(\tilde{v}_{m\ell}^{\Sigma,b}(t')\tilde{\rho}_{\ell n}^{(0)}(t') - \tilde{\rho}_{m\ell}^{(0)}(t')\tilde{v}_{\ell n}^{\Sigma,b}(t')\right),$$

where the sum over $\ell$ is over all states, and we have used the linear interaction Hamiltonians, Eq. (2.10). Since $U(t) = \exp(iH_0^S t/\hbar)$, we get $\tilde{v}_{m\ell}^{\Sigma,b}(t') = v_{m\ell}^{\Sigma,b}e^{i\omega_{m\ell}^S t'}$, $\tilde{\rho}_{\ell n}^{0}(t') = f_\ell\delta_{\ell n}$, and $\omega_{m\ell}^S = \omega_m^S(\mathbf{k}) - \omega_\ell^S(\mathbf{k})$, where we have omitted the dependence on $\mathbf{k}$. Then $\tilde{\rho}_{mn}^{(1)}(t) = \rho_{mn}^{(1)}e^{i\omega_{mn}^S t}e^{-i\tilde{\omega}t}$, with

$$\rho_{mn}^{(1)}(t) = \frac{e}{\hbar c}\frac{v_{mn}^{\Sigma,b}f_{nm}}{\omega_{mn}^S - \tilde{\omega}}A^b(\omega), \tag{2.16}$$

where $f_{nm} = f_n - f_m$. Using $\mathrm{Tr}(\rho^{(0)})/\Omega = n_0$, with $n_0$ the electronic density, and $d\mathbf{P}/dt = \langle \mathbf{J} \rangle$ to write $P^a(\omega) = (i/\tilde{\omega}) \langle J^a(\omega) \rangle = \chi^{ab}(-\omega;\omega)E^b(\omega)$, we get from Eq. (2.14) that

$$\begin{aligned}
\chi^{ab}(-\omega;\omega) &= \frac{e^2}{\hbar\tilde{\omega}^2}\int \frac{d^3k}{8\pi^3}\sum_{m\neq n}\frac{v^{\Sigma,a}_{nm}v^{\Sigma,b}_{mn}f_{nm}}{\omega^S_{mn}-\tilde{\omega}} - \frac{e^2 n_0}{m_e\tilde{\omega}^2}\delta_{ab} + \frac{ie^2}{\hbar\tilde{\omega}^2}\frac{1}{\Omega}\mathrm{Tr}(\rho^{(0)}\mathcal{F}^{ab}) \\
&= \frac{e^2}{\hbar}\int \frac{d^3k}{8\pi^3}\sum_{m\neq n} f_{nm}v^{\Sigma,a}_{nm}v^{\Sigma,b}_{mn}\Big(\frac{1}{(\omega^S_{mn})^2(\omega^S_{mn}-\tilde{\omega})} + \frac{1}{(\omega^S_{mn})^2\tilde{\omega}} \\
&+ \frac{1}{\omega^S_{mn}\tilde{\omega}^2}\Big) - \frac{e^2 n_0}{m_e\tilde{\omega}^2}\delta_{ab} + \frac{ie^2}{\hbar\tilde{\omega}^2}\frac{1}{\Omega}\mathrm{Tr}(\rho^{(0)}\mathcal{F}^{ab}) \qquad (2.17)
\end{aligned}$$

is the linear susceptibility within the scissored Hamiltonian; we used a partial fraction expansion in the first term after the first equal sign. We have defined

$$\mathcal{F}^{ab} = [r^a, v^{S,b}], \qquad (2.18)$$

and used the fact that the $f_{nm}$ factor allow us to write $m \neq n$ and that in the continuous limit of $\mathbf{k}$ $(1/\Omega)\sum_{\mathbf{k}} \to \int d^3k/(8\pi^3)$.

From time reversal symmetry we have that $v^S_{mn}(-\mathbf{k}) = -v^S_{nm}(\mathbf{k})$ and $\omega^S_{mn}(-\mathbf{k}) = \omega^S_{mn}(\mathbf{k})$ impliying that the contribution to $\chi^{ab}(-\omega;\omega)$, coming from the $1/\tilde{\omega}$, term cancels out. By index manipulation, the third term, combined with the fourth term in the right hand side of Eq. (2.17), gives

$$\frac{e^2}{\hbar}\int \frac{d^3k}{8\pi^3}\sum_{m\neq n} f_n \frac{v^{\Sigma,a}_{nm}v^{\Sigma,b}_{mn} + v^{\Sigma,a}_{mn}v^{\Sigma,b}_{nm}}{\omega^S_{mn}} - \frac{e^2 n_0}{m_e}\delta_{ab} \equiv \zeta^{ab}. \qquad (2.19)$$

The last term on the right hand side of Eq. (2.17) reduces to

$$\frac{ie^2}{\hbar}\int \frac{d^3k}{8\pi^3}\sum_n f_n\mathcal{F}^{ab}_{nn} \equiv \eta^{ab}, \qquad (2.20)$$

where

$$\mathcal{F}^{ab}_{nn} = i\Delta\sum_{m(\neq n)} f_{nm}(r^a_{nm}r^b_{mn} + r^b_{nm}r^a_{mn}). \qquad (2.21)$$

Summing $m$ over all $v$ and $c$ states different from $n$ (see the Appendix). Finally, Eq. (2.17) reduces to

$$\chi^{ab}(-\omega;\omega) = \frac{e^2}{\hbar}\int \frac{d^3k}{8\pi^3}\sum_{m\neq n}\frac{v^{\Sigma,a}_{nm}v^{\Sigma,b}_{mn}f_{nm}}{(\omega^S_{mn})^2(\omega^S_{mn}-\tilde{\omega})} + \frac{\zeta^{ab}}{\tilde{\omega}^2} + \frac{\eta^{ab}}{\tilde{\omega}^2}, \qquad (2.22)$$

which is the linear response coefficient obtained within the velocity gauge, including the scissors correction. Using

$$\mathbf{v}^{\Sigma}_{nm} = \frac{\omega^S_{nm}}{\omega_{nm}}\mathbf{v}_{nm}\,, \quad (n \neq m), \tag{2.23}$$

and $\omega^S_{mn} = \omega_{mn} - f_{mn}\Delta$, from the appendix we get that

$$\chi^{ab}(-\omega;\omega) = \frac{e^2}{\hbar}\int \frac{d^3k}{8\pi^3}\sum_{m\neq n}\frac{f_{nm}v^a_{nm}v^b_{mn}}{\omega^2_{mn}(\omega^S_{mn}-\tilde{\omega})} - \frac{e^2}{\tilde{\omega}^2}\int\frac{d^3k}{8\pi^3}\sum_n f_n\left[\frac{1}{m^*_n}\right]^{ab}, \tag{2.24}$$

where $[1/m^*_n]^{ab}$ is the effective mass tensor given in Eq. (2.54).

For a clean, cold semiconductor $f_n = f_n(\mathbf{k}) = 1$ or 0, independent of $\mathbf{k}$ and the integration over the Brillouin Zone of the term involving the effective mass tensor vanishes identically [GMS91], implying

$$\chi^{ab}(-\omega;\omega) = \frac{e^2}{\hbar}\int \frac{d^3k}{8\pi^3}\sum_{m\neq n}\frac{f_{nm}v^a_{nm}v^b_{mn}}{\omega^2_{mn}(\omega^S_{mn}-\omega-i\eta)}, \tag{2.25}$$

where the energy denominator leads to resonances when $\omega^S_{mn} = \omega$.

A similar calculation neglecting the scissors term in the Hamiltonian leads to

$$\chi^{ab}_{\text{unscissored}}(-\omega;\omega) = \frac{e^2}{\hbar}\int \frac{d^3k}{8\pi^3}\sum_{m\neq n}\frac{f_{nm}v^a_{nm}v^b_{mn}}{\omega^2_{mn}(\omega_{mn}-\omega-i\eta)},$$

where now the resonances are at $\omega_{mn} = \omega$. A naïve procedure to "scissors" the above result would be to take

$$\chi^{ab}_{\text{naïve}}(-\omega;\omega) = \frac{e^2}{\hbar}\int \frac{d^3k}{8\pi^3}\sum_{m\neq n}\frac{f_{nm}v^{\Sigma,a}_{nm}v^{\Sigma,b}_{mn}}{(\omega^S_{mn})^2(\omega^S_{mn}-\omega-i\eta)}, \tag{2.26}$$

an incorrect strategy, since it misses the second and third terms on the right hand side of Eq. (2.22). However, using Eq. (2.23) in Eq. (2.26) leads by coincidence to the correct result of Eq. (2.25). It appears that this has not been appreciated in the literature; Eq. (2.22) shows the correct way to include the scissors Hamiltonian within the velocity gauge, which is not the usual strategy illustrated by Eq. (2.26) [las].

Using Eq. (2.43), Eq. (2.25) can be rewritten as

$$\chi^{ab}(-\omega;\omega) = \frac{e^2}{\hbar}\int \frac{d^3k}{8\pi^3}\sum_{m\neq n}\frac{f_{nm}r^a_{nm}r^b_{mn}}{\omega^S_{mn}-\omega-i\eta},$$

which is identical to the length gauge result for the scissored Hamiltonian [NOSS05]. Again, for the unscissored Hamiltonian [SS00],

$$\chi^{ab}_{\text{unscissored}}(-\omega;\omega) = \frac{e^2}{\hbar}\int\frac{d^3k}{8\pi^3}\sum_{m\neq n}\frac{f_{nm}r^a_{nm}r^b_{mn}}{\omega_{mn}-\omega-i\eta}.$$

As discussed by Nastos et al. [NOSS05], in the length gauge the unscissored linear susceptibility can be "scissored" by simply shifting $\omega_{nm}\rightarrow\omega^S_{nm}$ and keeping the same matrix elements $\mathbf{r}_{nm}$. Thus, as in the velocity gauge, the scissored linear response is simply rigidly shifted in energy form its LDA result, keeping the same line shape. We remark that this constitutes a direct analytical proof of gauge invariance for the linear response. For the nonlinear response, we have not been able to construct any such analytical proof. However, we can at least provide a check on the gauge invariance through a numerical calculation. In order to do this we need expressions for the second order response in the velocity and length gauges, and we now turn to the first of these.

#### 2.3.2.2 Non linear response

Using the results of subsection 2.3.1 and the previous subsection, we find that to second order in $\mathbf{A}$ the density matrix is given by

$$\begin{aligned}
\tilde{\rho}^{(2)}_{mn}(t) &= -\frac{i}{\hbar}\int_{-\infty}^{t}dt'[\tilde{H}_{I,1}(t'),\tilde{\rho}^{(1)}(t')]_{mn} - \frac{i}{\hbar}\int_{-\infty}^{t}dt'[\tilde{H}_{I,2}(t'),\tilde{\rho}^{(0)}(t')]_{mn} \\
&= \frac{e^2}{\hbar^2c^2}\Big[\sum_{\ell(\neq n)}\frac{f_{n\ell}v^{\Sigma,b}_{m\ell}v^{\Sigma,c}_{\ell n}}{\omega^S_{\ell n}-\tilde{\omega}} - \sum_{\ell(\neq m)}\frac{f_{\ell m}v^{\Sigma,c}_{m\ell}v^{\Sigma,b}_{\ell n}}{\omega^S_{m\ell}-\tilde{\omega}} + \frac{i}{2}f_{nm}\mathcal{F}^{bc}_{mn}\Big] \\
&\times \frac{A^b(\omega)A^c(\omega)}{\omega^S_{mn}-2\tilde{\omega}}e^{-i2\tilde{\omega}t}e^{i\omega^S_{mn}t} \\
&= \rho^{(2)}_{mn}e^{i\omega^S_{mn}t},
\end{aligned}$$

where, only the positive frequency terms are used like in the linear response. The $\mathcal{F}^{ab}_{mn}$ term is obtained in the appendix in Eq. (2.49). The macroscopic nonlinear current density can be calculated through Eq. (2.15), where we take

each term separately:

$$\begin{aligned}
\frac{1}{\Omega}\mathrm{Tr}(j_0^a\rho^{(2)}) &= e\int\frac{d^3k}{8\pi^3}\sum_{mn} v_{nm}^{\Sigma,a}\rho_{nm}^{(2)} \\
&= \frac{e^3}{\hbar^2c^2}\Big[\int\frac{d^3k}{8\pi^3}\sum_{mn}\frac{v_{nm}^{\Sigma,a}}{\omega_{mn}^S-2\tilde{\omega}}\Big(\sum_{\ell(\neq n)}\frac{f_{n\ell}v_{m\ell}^{\Sigma,b}v_{\ell n}^{\Sigma,c}}{\omega_{\ell n}^S-\tilde{\omega}} \\
&- \sum_{\ell(\neq m)}\frac{f_{\ell m}v_{m\ell}^{\Sigma,c}v_{\ell n}^{\Sigma,b}}{\omega_{m\ell}^S-\tilde{\omega}}\Big)+\frac{i}{2}\int\frac{d^3k}{8\pi^3}\sum_{m\neq n}\frac{f_{nm}v_{nm}^{\Sigma,a}\mathcal{F}_{mn}^{bc}}{\omega_{mn}^S-2\tilde{\omega}}\Big] \\
&\times A^b(\omega)A^c(\omega)e^{-i2\tilde{\omega}t},
\end{aligned} \tag{2.27}$$

$$\begin{aligned}
\frac{1}{\Omega}\mathrm{Tr}(j_1^a\rho^{(1)}) &= \frac{e^2}{cm_e}\frac{1}{\Omega}\mathrm{Tr}(\rho^{(1)})A^a(\omega)e^{-i\tilde{\omega}t}+\frac{ie^2}{\hbar c}\frac{1}{\Omega}\mathrm{Tr}(\mathcal{F}^{ab}\rho^{(1)})A^b(\omega)e^{-i\tilde{\omega}t} \\
&= \frac{ie^3}{\hbar^2c^2}\int\frac{d^3k}{8\pi^3}\sum_{m\neq n}f_{nm}\frac{\mathcal{F}_{nm}^{ab}v_{mn}^{\Sigma,c}}{\omega_{mn}^S-\tilde{\omega}}A^b(\omega)A^c(\omega)e^{-i2\tilde{\omega}t},
\end{aligned} \tag{2.28}$$

since $\mathrm{Tr}(\rho^{(1)})=0$ (see (2.16)), and finally

$$\begin{aligned}
\frac{1}{\Omega}\mathrm{Tr}(j_2^a\rho^{(0)}) &= -\frac{e^3}{2\hbar^2c^2}\int\frac{d^3k}{8\pi^3}\sum_{mn}\rho_{mn}^{(0)}[r^a,[r^b,v^{S,c}]]_{nm}A^b(\omega)A^c(\omega)e^{-i2\tilde{\omega}t} \\
&= -\frac{e^3}{2\hbar^2c^2}\int\frac{d^3k}{8\pi^3}\sum_{n}f_n[r^a,\mathcal{F}^{bc}]_{nn}A^b(\omega)A^c(\omega)e^{-i2\tilde{\omega}t} \\
&= -\frac{e^3}{2\hbar^2c^2}\int\frac{d^3k}{8\pi^3}\sum_{n}f_n\Big(r_{nm}^a\mathcal{F}_{mn}^{bc}-\mathcal{F}_{nm}^{bc}r_{mn}^a+i\frac{\partial}{\partial k^a}\mathcal{F}_{e,nn}^{bc}\Big) \\
&\times A^b(\omega)A^c(\omega)e^{-i2\tilde{\omega}t},
\end{aligned} \tag{2.29}$$

where we used the expressions for $[r^a,\mathcal{F}^{bc}]_{nn}$ derived in the Appendix. Employing time reversal symmetry, we can take $r_{nm}^a(-\mathbf{k})=r_{mn}^a(\mathbf{k})$, $\mathbf{r}_{mn;\mathbf{k}}(\mathbf{k})=-\mathbf{r}_{nm;\mathbf{k}}(-\mathbf{k})$, $\mathcal{F}_{nm}^{bc}(-\mathbf{k})=\mathcal{F}_{mn}^{bc}(\mathbf{k})$, and $\mathcal{F}_{nm}^{bc*}(\mathbf{k})=-\mathcal{F}_{mn}^{bc}(\mathbf{k})$. If we add the $\mathbf{k}$ and the $-\mathbf{k}$ contribution in Eq. (2.29), we get a perfect cancellation of the terms within the parenthesis, and so the contribution from $\mathrm{Tr}(j_2^a\rho^{(0)})$ vanishes.

Using $\langle\mathbf{J}\rangle^{(2)}=d\mathbf{P}^{(2)}/dt$ for the second harmonic response, we get $\mathbf{P}^{(2)}(2\omega)=$

$(i/2\tilde{\omega})\left\langle \mathbf{J}^{(2)}(2\omega)\right\rangle$, and from Eq. (2.5), Eq. (2.27) and Eq. (2.28) we find

$$\begin{aligned}\chi^{abc}(-2\omega;\omega,\omega) &= \frac{e^3}{2\hbar^2\tilde{\omega}^3}\Big[-i\int\frac{d^3k}{8\pi^3}\sum_{mn}\frac{v^{\Sigma,a}_{nm}\{v^{\Sigma,b}_{m\ell}v^{\Sigma,c}_{\ell n}\}}{\omega^S_{mn}-2\tilde{\omega}} \\ &\times \Big(\sum_{\ell(\neq n)}\frac{f_{n\ell}}{\omega^S_{\ell n}-\tilde{\omega}}-\sum_{\ell(\neq m)}\frac{f_{\ell m}}{\omega^S_{m\ell}-\tilde{\omega}}\Big) \\ &+ \frac{1}{2}\int\frac{d^3k}{8\pi^3}\sum_{m\neq n}f_{nm}\Big(\frac{v^{\Sigma,a}_{nm}\{\mathcal{F}^{bc}_{mn}\}}{\omega^S_{mn}-2\tilde{\omega}}+2\frac{\{\mathcal{F}^{ab}_{nm}v^{\Sigma,c}_{mn}\}}{\omega^S_{mn}-\tilde{\omega}}\Big)\Big],\end{aligned}$$

where $\{\}$ denotes the symmetrization of the Cartesian indices $bc$, i.e. $\{u^b s^c\} = (u^b s^c + u^c s^b)/2$. We take half of this expression and add the corresponding expression to it with $\mathbf{k}$ replaced by $-\mathbf{k}$ in the integrand; this of course yields a result equivalent to our first expression, and using time-reversal symmetry we simplify it to

$$\begin{aligned}\chi^{abc}(-2\omega;\omega,\omega) &= \frac{e^3}{2\hbar^2\tilde{\omega}^3}\Big[\int\frac{d^3k}{8\pi^3}\sum_{(mn)\neq\ell}\frac{\mathrm{Im}[v^{\Sigma,a}_{nm}\{v^{\Sigma,b}_{m\ell}v^{\Sigma,c}_{\ell n}\}]}{\omega^S_{mn}-2\tilde{\omega}} \\ &\times \Big(\frac{f_{n\ell}}{\omega^S_{\ell n}-\tilde{\omega}}-\frac{f_{\ell m}}{\omega^S_{m\ell}-\tilde{\omega}}\Big)+\frac{1}{2}\int\frac{d^3k}{8\pi^3}\sum_{m\neq n}f_{nm} \\ &\times \Big(\frac{\mathrm{Re}[\,v^{\Sigma,a}_{nm}\{\mathcal{F}^{bc}_{mn}\}]}{\omega^S_{mn}-2\tilde{\omega}}+2\frac{\mathrm{Re}[\{\mathcal{F}^{ab}_{nm}v^{\Sigma,c}_{mn}\}]}{\omega^S_{mn}-\tilde{\omega}}\Big)\Big]. \end{aligned} \tag{2.30}$$

Following Ghahramani et al. [GMS91], we use partial fractions to write the energy denominator of the first term on the right hand side of Eq. (2.30) as

$$\frac{A}{\tilde{\omega}^3}+\frac{B}{\tilde{\omega}^2}+\frac{C}{\tilde{\omega}}+F, \tag{2.31}$$

where the odd terms in $\omega$, $A$ and $C$, can be shown to give zero contribution [GMS91]. For the second term on the right hand side of Eq. (2.30) we expand the denominators in partial fractions to obtain

$$\frac{1}{\tilde{\omega}^3(\omega^S_{mn}-\tilde{\omega})}=\frac{1}{\tilde{\omega}(\omega^S_{mn})^3}+\frac{1}{\tilde{\omega}^3\omega^S_{mn}}+\frac{1}{\tilde{\omega}^2(\omega^S_{mn})^2}+\frac{1}{(\omega^S_{mn})^3(\omega^S_{mn}-\tilde{\omega})}, \tag{2.32}$$

and

$$\frac{1}{\tilde{\omega}^3(\omega^S_{mn}-2\tilde{\omega})}=\frac{4}{\tilde{\omega}(\omega^S_{mn})^3}+\frac{1}{\tilde{\omega}^3\omega^S_{mn}}+\frac{2}{\tilde{\omega}^2(\omega^S_{mn})^2}+\frac{8}{(\omega^S_{mn})^3(\omega^S_{mn}-2\tilde{\omega})}. \tag{2.33}$$

Using time reversal symmetry and manipulating band indices, we can show that all the odd terms in $\tilde{\omega}$ coming from Eq. (2.32) and Eq. (2.33) give zero contribution. Collecting the $B$ and $F$ terms of Eq. (2.31), and the non-zero terms of Eq. (2.32) and Eq. (2.33) we obtain

$$\begin{aligned}
\chi^{abc}(-2\omega;\omega,\omega) &= \frac{e^3}{2\hbar^2}\int\frac{d^3k}{8\pi^3}\Big[\sum_{n(m\neq\ell)}\Big(\frac{\mathrm{Im}[v^{\Sigma,a}_{mn}\{v^{\Sigma,b}_{n\ell}v^{\Sigma,c}_{\ell m}\}]}{\omega^S_{nm}-2\omega^S_{\ell m}} \\
&- \frac{\mathrm{Im}[v^{\Sigma,a}_{n\ell}\{v^{\Sigma,b}_{\ell m}v^{\Sigma,c}_{mn}\}]}{\omega^S_{\ell n}-2\omega^S_{\ell m}}\Big)\frac{f_{m\ell}}{(\omega^S_{\ell m})^3(\omega^S_{\ell m}-\tilde{\omega})} \\
&- 16\sum_{\ell(m\neq n)}\frac{f_{mn}}{\omega^S_{\ell m}-2\omega^S_{nm}}\frac{\mathrm{Im}[v^{\Sigma,a}_{m\ell}\{v^{\Sigma,b}_{\ell n}v^{\Sigma,c}_{nm}\}]}{(\omega^S_{\ell m})^3(\omega^S_{\ell m}-2\tilde{\omega})} \\
&- 16\sum_{m(\ell\neq n)}\frac{f_{\ell n}}{\omega^S_{\ell m}-2\omega^S_{\ell n}}\frac{\mathrm{Im}[v^{\Sigma,a}_{m\ell}\{v^{\Sigma,b}_{\ell n}v^{\Sigma,c}_{nm}\}]}{(\omega^S_{\ell m})^3(\omega^S_{\ell m}-2\tilde{\omega})} \\
&+ \sum_{m\neq n}\frac{f_{nm}}{(\omega^S_{mn})^3}\Big(4\frac{\mathrm{Re}[\,v^{\Sigma,a}_{nm}\{\mathcal{F}^{bc}_{mn}\}]}{\omega^S_{mn}-2\tilde{\omega}}+\frac{\mathrm{Re}[\{\mathcal{F}^{ab}_{nm}v^{\Sigma,c}_{mn}\}]}{\omega^S_{mn}-\tilde{\omega}}\Big)\Big],
\end{aligned} \tag{2.34}$$

as the non-divergent contribution, to which the divergent term

$$\begin{aligned}
\chi^{abc}_D(-2\omega;\omega,\omega) &= \frac{e^3}{2\hbar^2\tilde{\omega}^2}\int\frac{d^3k}{8\pi^3}\Big[\sum_{(mn)\neq\ell} b_{\ell mn}\mathrm{Im}[v^{\Sigma,a}_{nm}\{v^{\Sigma,b}_{m\ell}v^{\Sigma,c}_{\ell n}\}] \\
&+ \sum_{m\neq n}\frac{f_{nm}}{(\omega^S_{mn})^2}\Big(\mathrm{Re}[\,v^{\Sigma,a}_{nm}\{\mathcal{F}^{bc}_{mn}\}]+\mathrm{Re}[\{\mathcal{F}^{ab}_{nm}v^{\Sigma,c}_{mn}\}]\Big)\Big],
\end{aligned}$$

must be added, where

$$b_{\ell mn} = \frac{f_{m\ell}}{\omega^S_{nm}\omega^S_{\ell m}}\left(\frac{2}{\omega^S_{nm}}+\frac{1}{\omega^S_{\ell m}}\right)+\frac{f_{n\ell}}{\omega^S_{nm}\omega^S_{n\ell}}\left(\frac{2}{\omega^S_{nm}}+\frac{1}{\omega^S_{n\ell}}\right),$$

comes from the $B$ term of Eq. (2.31). Following the steps of Ghahramani et al. [GMS91], we can show that for a clean, cold semiconductor $\chi^{abc}_D = 0$ [cab].

Finally, we insert the explicit values for the $f_n$ factors and take the limit

of $\eta \to 0$ in Eq . (2.34) to find

$$\begin{aligned}
\mathrm{Im}[\chi^{abc}_{\mathrm{v}}(-2\omega;\omega,\omega)] &= \frac{\pi|e|^3}{2\hbar^2}\int\frac{d^3k}{8\pi^3}\Big[\sum_{vc}\frac{16}{(\omega^S_{cv})^3}\Big(\sum_{c'}\frac{\mathrm{Im}[v^{\Sigma,a}_{vc}\{v^{\Sigma,b}_{cc'}v^{\Sigma,c}_{c'v}\}]}{\omega^S_{cv}-2\omega^S_{c'v}} \\
&- \sum_{v'}\frac{\mathrm{Im}[v^{\Sigma,a}_{vc}\{v^{\Sigma,b}_{cv'}v^{\Sigma,c}_{v'v}\}]}{\omega^S_{cv}-2\omega^S_{cv'}}\Big)\delta(\omega^S_{cv}-2\omega) \\
&+ \sum_{(vc)\neq\ell}\frac{1}{(\omega^S_{cv})^3}\Big(\frac{\mathrm{Im}[v^{\Sigma,a}_{\ell c}\{v^{\Sigma,b}_{cv}v^{\Sigma,c}_{v\ell}\}]}{\omega^S_{c\ell}-2\omega^S_{cv}} \\
&- \frac{\mathrm{Im}[v^{\Sigma,a}_{v\ell}\{v^{\Sigma,b}_{\ell c}v^{\Sigma,c}_{cv}\}]}{\omega^S_{\ell v}-2\omega^S_{cv}}\Big)\delta(\omega^S_{cv}-\omega) \\
&- \sum_{vc}\frac{1}{(\omega^S_{cv})^3}\Big(4\mathrm{Re}[\,v^{\Sigma,a}_{vc}\{\mathcal{F}^{bc}_{cv}\}]\delta(\omega^S_{cv}-2\omega) \\
&+ \mathrm{Re}[\{\mathcal{F}^{ab}_{vc}v^{\Sigma,c}_{cv}\}]\delta(\omega^S_{cv}-\omega)\Big)\Big],
\end{aligned} \tag{2.35}$$

as the imaginary part of the nonlinear SHG susceptibility for the scissored Hamiltonian within the velocity gauge formalism, where we have used the subscript v to denote it. The $\mathrm{Re}[\chi^{abc}_{\mathrm{v}}(-2\omega;\omega,\omega)]$ is obtained through the Kramers-Kroning transformation. Taking $\Delta = 0$ we get

$$\begin{aligned}
\mathrm{Im}[\chi^{abc}_{\mathrm{v},\Delta=0}(-2\omega;\omega,\omega)] &= \frac{\pi|e|^3}{2\hbar^2}\int\frac{d^3k}{8\pi^3}\Big[\sum_{vc}\frac{16}{(\omega_{cv})^3}\Big(\sum_{c'}\frac{\mathrm{Im}[v^{a}_{vc}\{v^{b}_{cc'}v^{c}_{c'v}\}]}{\omega_{cv}-2\omega_{c'v}} \\
&- \sum_{v'}\frac{\mathrm{Im}[v^{a}_{vc}\{v^{b}_{cv'}v^{c}_{v'v}\}]}{\omega_{cv}-2\omega_{cv'}}\Big)\delta(\omega_{cv}-2\omega) \\
&+ \sum_{(vc)\neq\ell}\frac{1}{(\omega_{cv})^3}\Big(\frac{\mathrm{Im}[v^{a}_{\ell c}\{v^{b}_{cv}v^{c}_{v\ell}\}]}{\omega_{c\ell}-2\omega_{cv}} - \frac{\mathrm{Im}[v^{a}_{v\ell}\{v^{b}_{\ell c}v^{c}_{cv}\}]}{\omega_{\ell v}-2\omega_{cv}}\Big) \\
&\times\ \delta(\omega_{cv}-\omega)\Big],
\end{aligned}$$

since $\mathcal{F}^{ab}_{nm}|_{\Delta=0} = 0$ (see the appendix). This equation is identical to that obtained earlier for the unscissored Hamiltonian [GMS91]. However, as far as we know the expression for $\mathrm{Im}[\chi^{abc}(-2\omega;\omega,\omega)]$ given in Eq. (2.35) is new, and the last two terms proportional to $\Delta$ through $\mathcal{F}^{ab}_{nm}$ (see Eq. (2.49) have been neglected in the literature until now. As shown below (Section 2.4), these terms are crucial for the gauge invariance of the second order response within the scissored Hamiltonian.

In the past the scissors implementation within the velocity gauge has been performed by taking Eq. (2.36) and simply replacing $\omega_{mn}$ by $\omega^S_{mn}$ and $\mathbf{v}_{mn}$ with $\mathbf{v}^\Sigma_{mn}$, as the usual scissoring of the linear response would wrongly suggest. This strategy leads to

$$\begin{aligned}
\mathrm{Im}[\chi^{abc}_{\mathrm{v,wrong}}(-2\omega;\omega,\omega)] &= \frac{\pi|e|^3}{2\hbar^2}\int\frac{d^3k}{8\pi^3}\Big[\sum_{vc}\frac{16}{(\omega^S_{cv})^3}\Big(\sum_{c'}\frac{\mathrm{Im}[v^{\Sigma,a}_{vc}\{v^{\Sigma,b}_{cc'}v^{\Sigma,c}_{c'v}\}]}{\omega^S_{cv}-2\omega^S_{c'v}} \\
&- \sum_{v'}\frac{\mathrm{Im}[v^{\Sigma,a}_{vc}\{v^{\Sigma,b}_{cv'}v^{\Sigma,c}_{v'v}\}]}{\omega^S_{cv}-2\omega^S_{cv'}}\Big)\delta(\omega^S_{cv}-2\omega) \\
&+ \sum_{(vc)\neq\ell}\frac{1}{(\omega^S_{cv})^3}\Big(\frac{\mathrm{Im}[v^{\Sigma,a}_{\ell c}\{v^{\Sigma,b}_{cv}v^{\Sigma,c}_{v\ell}\}]}{\omega^S_{c\ell}-2\omega^S_{cv}} \\
&- \frac{\mathrm{Im}[v^{\Sigma,a}_{v\ell}\{v^{\Sigma,b}_{\ell c}v^{\Sigma,c}_{cv}\}]}{\omega^S_{\ell v}-2\omega^S_{cv}}\Big)\delta(\omega^S_{cv}-\omega)\Big],
\end{aligned} \tag{2.36}$$

a wrong result, since we are missing the important contribution from $\mathcal{F}^{ab}_{mn}$ given in Eq. (2.35). It is obvious that the coincidence that takes place in the linear response does not arise here. If we substitute $\mathbf{v}^\Sigma_{nm} = (\omega^S_{nm}/\omega_{nm})\mathbf{v}_{nm}$ in Eq. (2.36) we do not get the last two terms on the right hand side of Eq. (2.35)!

### 2.3.3 Length gauge formalism

Within this gauge, the interaction Hamiltonian is given by

$$H_I(t) = -e\mathbf{r}\cdot\mathbf{E}(t). \tag{2.37}$$

As discussed in Nastos et al. [NOSS05], the length-gauge formalism for the scissored Hamiltonian can be easily worked out by simply using the unscissored Hamiltonian for the unperturbed system with $-e\mathbf{r}\cdot\mathbf{E}(t)$ as the interaction, and then, at the end of the calculation, only replacing $\omega_{nm}$ by $\omega^S_{nm}$ to obtain the scissored result for any susceptibility expression, whether linear or nonlinear. Indeed, $\mathbf{r}_{nm}$ and $\mathbf{r}_{nm;\mathbf{k}}$ are calculated within the unscissored (LDA) Hamiltonian, as stated before. We use $H(t) = H_0 - e\mathbf{r}\cdot\mathbf{E}(t)$ as the time dependent Hamiltonian, that from Eq. (2.4) gives $\dot{\mathbf{r}} = \mathbf{v} = \mathbf{p}/m_e$.

Taking the matrix elements of the density using, Eq. (2.2) with $H_I(t)$ of Eq. (2.37), we obtain $(\tilde{\rho}^{(1)}_L(t))_{nm} = B^b_{nm}E^b(\omega)e^{i(\omega_{nm}-\tilde{\omega})t}$, with

$$B^b_{nm} = \frac{e}{\hbar}\frac{f_{mn}r^b_{nm}}{\omega_{nm}-\tilde{\omega}},$$

and

$$(\tilde{\rho}_L^{(2)}(t))_{nm} = \frac{e}{i\hbar}\frac{1}{\omega_{nm}-2\tilde{\omega}}\left[i\sum_\ell\left(r^b_{n\ell}B^c_{\ell m}-B^c_{n\ell}r^b_{\ell m}\right)-(B^c_{nm})_{;k^b}\right] \times E^b(\omega)E^c(\omega)e^{i(\omega_{nm}-2\tilde{\omega})t}.$$

We have used the fact that for a cold semiconductor $\partial f_n/\partial\mathbf{k}=0$ and thus the intraband contribution to the linear term vanishes identically. From Eq. (2.3) we can obtain [AS95]

$$\chi^{abc}_{L,e}(-2\omega;\omega,\omega) = \frac{e^3}{\hbar^2}\int\frac{d^3k}{8\pi^3}\Big[\sum_{\ell(n\neq m)}\frac{2f_{nm}}{\omega_{mn}-2\tilde{\omega}}+\sum_{m(\ell\neq n)}\frac{f_{\ell n}}{\omega_{\ell n}-\tilde{\omega}} + \sum_{n(\ell\neq m)}\frac{f_{m\ell}}{\omega_{m\ell}-\tilde{\omega}}\Big]\frac{r^a_{nm}\{r^b_{m\ell}r^c_{\ell n}\}}{\omega_{\ell n}-\omega_{m\ell}},$$

as the contribution from interband processes, and

$$\chi^{abc}_{L,i}(-2\omega;\omega,\omega) = \frac{ie^3}{\hbar^2}\int\frac{d^3k}{8\pi^3}\sum_{m\neq n}f_{nm}\Big[\frac{2r^a_{nm}\{r^b_{mn;k^c}\}}{\omega_{mn}(\omega_{mn}-2\tilde{\omega})}+\frac{\{r^a_{nm;k^c}r^b_{mn}\}}{\omega_{mn}(\omega_{mn}-\tilde{\omega})} + \frac{1}{\omega^2_{mn}}\Big(\frac{1}{\omega_{mn}-\tilde{\omega}}-\frac{4}{\omega_{mn}-2\tilde{\omega}}\Big)r^a_{nm}\{r^b_{mn}\mathcal{V}^c_{mn}\} - \frac{\{r^b_{nm;k^a}r^c_{mn}\}}{2\omega_{mn}(\omega_{mn}-\tilde{\omega})}\Big],$$

as the contribution from intraband processes only, where $r^b_{nm;k^a}$ is the generalized derivative of $\mathbf{r}$, and is explicitly given by [AS95],

$$r^b_{nm;k^a} = \frac{r^a_{nm}\mathcal{V}^b_{mn}+r^b_{nm}\mathcal{V}^a_{mn}}{\omega_{nm}}+\frac{i}{\omega_{nm}}\sum_\ell\left(\omega_{\ell m}r^a_{n\ell}r^b_{\ell m}-\omega_{n\ell}r^b_{n\ell}r^a_{\ell m}\right);\quad (n\neq m), \tag{2.38}$$

where $\mathcal{V}^a_{nm}=(p^a_{nn}-p^a_{mm})/m_e$ is the difference between the electron velocity at bands $n$ and $m$, and the sum over $\ell$ is over all the valence and conduction states.

Notice that the above expressions for $\chi^{abc}_{L,e,i}(-2\omega;\omega,\omega)$ are divergence free at $\omega=0$, that both satisfy the intrinsic permutation symmetry

$$\chi^{abc}_{L,e,i}(-2\omega;\omega,\omega)=\chi^{acb}_{L,e,i}(-2\omega;\omega,\omega), \tag{2.39}$$

and finally that the full susceptibility is given by

$$\chi^{abc}_{L}(-2\omega;\omega,\omega)=\chi^{abc}_{L,e}(-2\omega;\omega,\omega)+\chi^{abc}_{L,i}(-2\omega;\omega,\omega), \tag{2.40}$$

where the subscript $L$ denotes the length gauge. Again using time reversal symmetry, we can take $\mathbf{r}_{mn}(\mathbf{k}) = \mathbf{r}_{nm}(-\mathbf{k})$ and $\mathbf{r}_{mn;\mathbf{k}}(\mathbf{k}) = -\mathbf{r}_{nm;\mathbf{k}}(-\mathbf{k})$, along with the hermiticity condition $\mathbf{r}_{mn} = \mathbf{r}^*_{nm}$, which implies that $\mathbf{r}_{mn;\mathbf{k}} = \mathbf{r}^*_{nm;\mathbf{k}}$, and leading to the imaginary parts of $\chi^{abc}_{i,e}$,

$$\begin{aligned}\mathrm{Im}[\chi^{abc}_{L,e}] &= \frac{\pi|e|^3}{\hbar^2}\int\frac{d^3k}{8\pi^3}\sum_{(vc)\neq\ell}\Big[\frac{2\mathrm{Re}[r^a_{vc}\{r^b_{c\ell}r^c_{\ell v}\}]}{\omega^S_{c\ell}-\omega^S_{\ell v}}\delta(\omega^S_{cv}-2\omega) \\ &+ \Big(\frac{\mathrm{Re}[r^a_{v\ell}\{r^b_{\ell c}r^c_{cv}\}]}{\omega^S_{cv}-\omega^S_{\ell c}}+\frac{\mathrm{Re}[r^a_{\ell c}\{r^b_{cv}r^c_{v\ell}\}]}{\omega^S_{v\ell}-\omega^S_{cv}}\Big)\delta(\omega^S_{cv}-\omega)\Big] \end{aligned} \tag{2.41}$$

and

$$\begin{aligned}\mathrm{Im}[\chi^{abc}_{L,i}] &= \frac{\pi|e|^3}{\hbar^2}\int\frac{d^3k}{8\pi^3}\sum_{vc}\Big[\Big(\frac{2\mathrm{Im}[r^a_{vc}\{r^b_{cv;k^c}\}]}{\omega^S_{cv}}-\frac{4\mathrm{Im}[r^a_{vc}\{r^b_{cv}\mathcal{V}^c_{cv}\}]}{(\omega^S)^2_{cv}}\Big) \\ &\times\ \delta(\omega^S_{cv}-2\omega) \\ &+ \Big(\frac{\mathrm{Im}[\{r^a_{vc;k^c}r^b_{cv}\}]}{\omega^S_{cv}}+\frac{\mathrm{Im}[r^a_{vc}\{r^b_{cv}\mathcal{V}^c_{cv}\}]}{(\omega^S)^2_{cv}}-\frac{\mathrm{Im}[\{r^b_{vc;k^a}r^c_{cv}\}]}{2\omega^S_{cv}}\Big) \\ &\times\ \delta(\omega^S_{cv}-\omega)\Big], \end{aligned} \tag{2.42}$$

where we have taken $\omega_{nm}\to\omega^S_{nm}$ so the above expressions are valid for the scissors Hamiltonian, $H^S = H_0 + S(\mathbf{r},\mathbf{p}) - e\mathbf{r}\cdot\mathbf{E}$. Recall that both $\mathbf{r}_{nm}$ and $\mathbf{r}_{nm;\mathbf{k}}$ werw calculated with the unscissored (Kohn-Sham) Hamiltonian [NOSS05]. The last two equations give the nonlinear SHG susceptibility within the length gauge for the scissored Hamiltonian. Comparing Eq. (2.41) and Eq. (2.42) to the velocity gauge result of Eq. (2.35), it is clear that, unlike for the linear response, there is no obvious analytical scheme to support that both gauges give the same result. In the following section we present numerical results to prove the expected gauge invariance.

## 2.4 Results

In this section we evaluate the velocity and length gauge expressions $\chi^{abc}_{\mathrm{v},L}$ for GaAs. In order to calculate the energies, wave functions and matrix elements we employ the "augmented plane wave plus local orbital method" using the WIEN2K code [BSM+01]. This all-electron code uses the full local-crystal potential, i.e. $V(\mathbf{r})$, just as required by our assumptions of Eq. (2.6), and thus the commutator $[\mathbf{r},H] = i\hbar\dot{\mathbf{r}}$ is correctly calculated for the local $V(\mathbf{r})$. We also

| Parameter (GaAs) | all-electron | pseudopotential |
|---|---|---|
| Lattice parameter | $10.684a_0$ | $10.684a_0$ |
| **k**-points | 27720 | 27720 |
| Unscissored band gap | 0.277 eV | 0.469 eV |
| Scissors | 1.243 eV | 1.051 eV |
| Valence bands | 14 (includes semi-core) | 4 |
| Conduction bands | 7 | 7 |
| Exchange correlation energy | LDA | LDA |
| Energy convergence limit | 0.001 Ry | - |
| Cut-off energy | - | 20 Ha |
| $R_{\rm MT}K_{\rm MAX}$ | 7.0 | - |

Table 2.1: The most important parameters used in the all-electron and pseudopotential schemes for GaAs. The empty entries are not relevant for the corresponding code. The **k**-points are for the irreducible part of the first Brillouin zone, and $R_{\rm MT}K_{\rm MAX}$ is a product of the "muffin-tin" radius $R$ and the maximum value for the plane wave vectors $\mathbf{K}$ [BSM+01].

show results calculated through the use of pseudopotentials with the ABINIT plane-wave code [GBC+02]. The pseudopotentials are non-local functions expressible as $V^{\rm NL}(\mathbf{r},\mathbf{p})$ [Sta71], just as is the scissor Hamiltonian $S(\mathbf{r},\mathbf{p})$. To really complete the calculation one would have to do the corresponding manipulations including $V^{\rm NL}(\mathbf{r},\mathbf{p})$ in the Hamiltonian $H^S$ (Eq. (2.9)), and new terms would arise in the linear and nonlinear susceptibility expressions. For instance, the term $i\hbar\mathbf{v}^{\rm NL} = [\mathbf{r}, V^{\rm NL}(\mathbf{r},\mathbf{p})]$ should be added to the velocity operator $\mathbf{v}^{\Sigma}$ given by Eq. (2.13). This is a research project for the future. Here we use the comparison of the all-electron and the pseudopotential calculation to get a estimate of the error involved by neglecting the nonlocal contributions coming from $V^{\rm NL}(\mathbf{r},\mathbf{p})$. The linear response counterpart of these calculations is discussed in Pulci et al. [PODSS98] and Mendoza et al. [MNAS06].

The spin-orbit effects, local field effects, and the consequences of the electron-hole attraction [LSHB05] on the SHG process are neglected. Although all these effects are important for the optical response of a semiconductor, their calculation is still subject of research and a numerical challenge that ought to be pursued. However this endeavour is beyond the scope of this thesis. The band gap of GaAs is adjusted to be its experimental value of 1.52 eV. We find converged spectra for all the quantities of interest in this work, and the most

important parameters are shown in Table 2.1. All the spectra are calculated with an energy smearing of 0.15 eV. The linear analytic tetrahedron method is used to evaluate the Brillouin zone integrals for the imaginary part of the spectra, where special care was taken to examine the double resonances [NOSS05]. Double resonances occur if, for a given frequency $\omega$, there can be resonant transitions at both frequencies $\omega$ and $2\omega$, that is, if there is a region in the Brillouin zone such that $\omega_{cv}(\mathbf{k}) = 2\omega_{c'v}(\mathbf{k}) = 2\omega$. For these $\mathbf{k}$ points the perturbation theory used to calculate the spectrum breaks down, since there is real population excited, which in a correct calculation must be taken into account. These points introduce sharp spikes in the spectrum that can in principle affect the low-frequency results, since the response at frequencies below the band gap is computed from the Kramers-Kronig relation. However, in agreement with Nastos et al. [NOSS05], we find here that the double resonances affect the low-frequency results by less than 2%.

In Fig. 2.1 we show the imaginary part of $\chi^{xyz}_{\mathrm{v},L}(-2\omega;\omega,\omega)$ with no scissors correction ($\Delta = 0$), calculated with the all-electron scheme [nota]. As expected, $\mathrm{Im}[\chi^{xyz}_{\mathrm{v},L}](-2\omega;\omega,\omega)$ is zero below the gap, ($E_g^{LDA} = 0.27$ eV), and above it we see a series of positive and negative peaks that can be related to electronic transitions. What is more relevant for this chapter is that in the (a) panel of Fig. 2.1 we have plotted both $\chi^{xyz}_{\mathrm{v}}(-2\omega;\omega,\omega)$ and $\chi^{xyz}_{L}(-2\omega;\omega,\omega)$; they seem to be identical. In the bottom panel (b) of Fig. 2.1, we show $\mathrm{Im}[\chi^{xyz}_{L}(-2\omega;\omega,\omega) - \chi^{xyz}_{\mathrm{v}}(-2\omega;\omega,\omega)]$, which confirms that the results for the unscissored $\mathrm{Im}[\chi^{abc}_{\mathrm{v}}(-2\omega;\omega,\omega)]$ and $\mathrm{Im}[\chi^{abc}_{L}(-2\omega;\omega,\omega)]$ coincide to within a numerical accuracy of about 1 part in approximately $10^5$, as would be expected from gauge invariance.

In Fig. 2.2 we show the imaginary part of $\chi^{xyz}_{\mathrm{v},L}(-2\omega;\omega,\omega)$ with a scissors shift of $\Delta = 1.243$ eV, calculated with the all-electron scheme. In the top panel we compare the velocity-gauge calculation of $\mathrm{Im}[\chi^{xyz}_{\mathrm{v}}(-2\omega;\omega,\omega)]$ (of Eq. (2.35)) to a calculation where we neglect the new contributions coming from the scissors term, (i.e. $\mathrm{Im}[\chi^{xyz}_{\mathrm{v,wrong}}(-2\omega;\omega,\omega)]$ of Eq. (2.36)); we see that the results disagree. In the middle panel we show $\mathrm{Im}[\chi^{xyz}_{L}(-2\omega;\omega,\omega)]$ and in the bottom panel we show $\mathrm{Im}[\chi^{xyz}_{L}(-2\omega;\omega,\omega) - \chi^{xyz}_{\mathrm{v}}(-2\omega;\omega,\omega)]$, where it is clear that, as in the unscissored case, gauge invariance with the scissored Hamiltonian is confirmed within good numerical accuracy. We stress that this fulfillment of gauge invariance is due to the additional terms of Eq. (2.35) proportional to $\mathcal{F}^{ab}_{mn}$ which, in turn, depend on the commutator $[\mathbf{r}, \mathbf{v}^S]$, with $\mathbf{v}^S = -(i/\hbar)[\mathbf{r}, S(\mathbf{r},\mathbf{p})]$, thus, neglecting the effect of the scissors operator $S(\mathbf{r},\mathbf{p})$ in the usual perturbation procedure would lead, in general, to the wrong

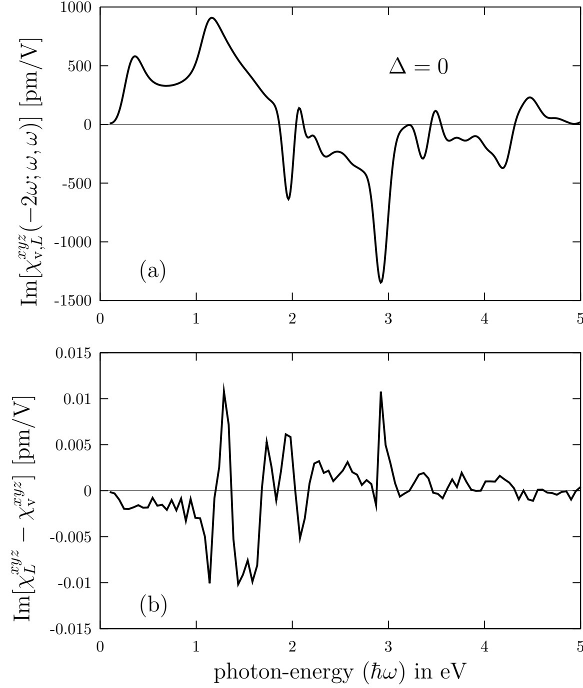


Figure 2.1: (a) Plot of the $\text{Im}[\chi^{xyz}_{v,L}(-2\omega;\omega,\omega)]$ calculated within the length and the velocity gauge schemes, using the all-electron approach for zero scissors correction, $\Delta = 0$. (b) Plot of the $\text{Im}[\chi^{xyz}_{L}(-2\omega;\omega,\omega) - \chi^{xyz}_{v}(-2\omega;\omega,\omega)]$ where very small differences between the two schemes are seen.

result for nonlinear susceptibility tensors within the velocity gauge approach.

As explained above, we have also used a pseudopotential method to calculate the SHG susceptibility tensor. This way, we can estimate the error made when one calculates the matrix elements of the electron's momentum operator through the use of pseudopotentials, the error arising from the non-local part of the pseudopotential in the commutators [PODSS98, MNAS06]. In Fig. 2.3 we show the absolute value of $|\chi^{xyz}_{L}(-2\omega;\omega,\omega)| = |\chi^{xyz}_{v}(-2\omega;\omega,\omega)| \equiv |\chi^{xyz}(-2\omega;\omega,\omega)|$ with the scissors corrections, of $\Delta = 1.051$ eV using pseudopotential code and of $\Delta = 1.243$ eV using the all-electron code. Notice that there is a difference of approximately 36.8 pm/V between the results of the value of the static limit of $|\chi^{xyz}(-2\omega;\omega,\omega)|$ calculated within the length and the velocity gauges. We obtain a static value of $|\chi^{xyz}(0;0,0)| = 135.6$ pm/V for the pseudo-potential calculation, and $|\chi^{xyz}(0;0,0)| = 172.4$ pm/V, for the

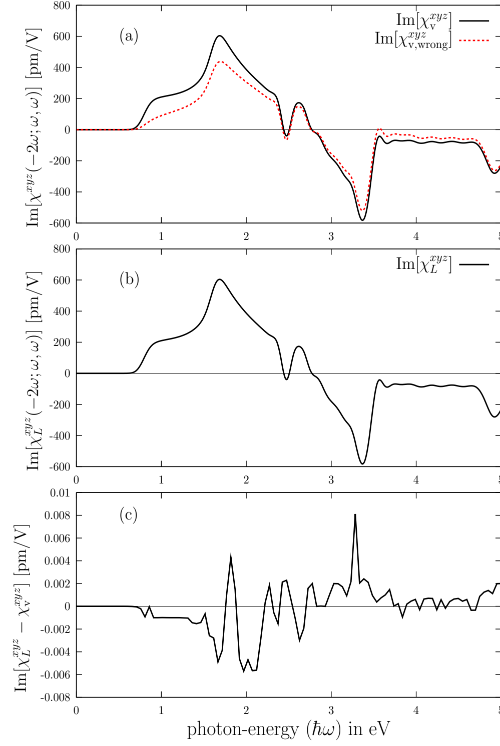

Figure 2.2: (a) Plots of the $\text{Im}[\chi_{\text{v}}^{xyz}(-2\omega;\omega,\omega)]$ and $\text{Im}[\chi_{\text{v,wrong}}^{xyz}(-2\omega;\omega,\omega)]$ calculated within the velocity gauge. (b) Plot of the $\text{Im}[\chi_{L}^{xyz}(-2\omega;\omega,\omega)]$ calculated within the length gauge. (c) Plot of $\text{Im}[\chi_{L}^{xyz}(-2\omega;\omega,\omega)-\chi_{\text{v}}^{xyz}(-2\omega;\omega,\omega)]$ where very small differences are seen . The spectra is evaluated within the all-electron approach using a scissors correction of $\Delta = 1.243$ eV.

all-electron calculation. These quantities are close to the theoretical values of other studies [NOSS05], and to the recently found experimental value of 172 pm/V at 0.118 eV [ETP+01]. We see that the corrections owing to the non-local nature of the pseudopotentials affect, not only the strength of the spectrum, but also its line shape, as some resonances are energy shifted from one calculation to the other. The overall intensity correction is smaller than $\sim 25\%$, and we may conclude that the pseudopotential calculation does a reasonable job for the nonlinear response. Indeed, this seems to be the case for the linear optical response as well [MNAS06].

Although the main objective of this chapter is to show how the non-local

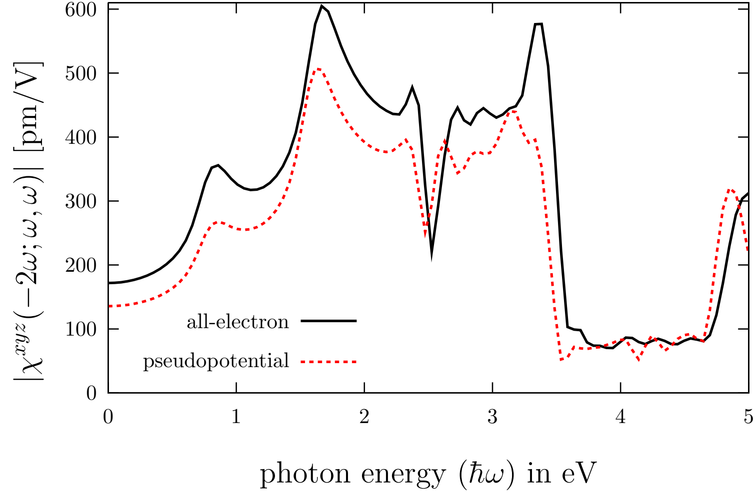


Figure 2.3: Plot of $|\chi_L^{xyz}(-2\omega;\omega,\omega)| = |\chi_{\rm v}^{xyz}(-2\omega;\omega,\omega)| \equiv |\chi^{xyz}(-2\omega;\omega,\omega)|$ with a scissors correction of $\Delta = 1.243$ eV for the all-electron calculation and $\Delta = 1.051$ eV for the pseudopotential calculation.

scissors correction must be included in the linear and nonlinear optical response, and how including it fulfills gauge invariance, as shown in Fig. 2.2, we present for comprisson purposes the theoretical and experimental results. In Fig. 2.4 we show the experimental spectrum of $\chi^{xyz}$ measured by Bergfeld and Daum [BD03]. In order to have a better comparison between theory and experiment, the energy scale of the theoretical results has been linearly rescaled as proposed by them [notb]. Our results for the all-electron calculation for $\chi^{xyz}$ shows a good qualitative agreement with the experimental spectrum. Above 4.3 eV the theoretical signal qualitatively disagrees with the experimental signal, although it shows a similar line shape but blue-shifted in energy. The theoretical spectra obtained in Ref. [RLS98, LSHB05, NOSS05, AB98, HS96] qualitatively show a similar comparison with the experiment.

## 2.5 Conclusions

We have presented a comparison between the calculations of the second harmonic susceptibility tensor using two well-known approaches, often colloquially referred to as using the “velocity gauge” and the “length gauge”. We have done this using two different Hamiltonians: the usual LDA Hamiltonian and the

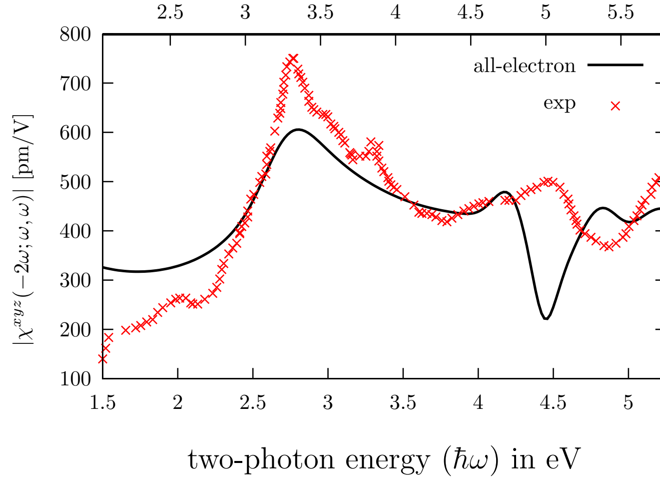


Figure 2.4: Plot of $|\chi_L^{xyz}| = |\chi_v^{xyz}| = \chi^{xyz}$ with with a scissors correction of $\Delta = 1.243$ eV for the all-electron calculation, along with the experimental data of Ref. [BD03]. The top axis is the original energy $E_{\rm orig}$ of the all-electron calculation. The bottom axis is the scaled energy, $2E_{\rm mod}$ [notb], for the theoretical spectra and the two-photon energy of the experimental data.

scissored Hamiltonian, where a rigid energy shift in the conduction bands is introduced so that the experimental (or GW) energy gap is obtained. We derived a new expression for the velocity gauge susceptibility $\chi_{\rm v}^{abc}(-2\omega;\omega,\omega)$, where correction terms related to the non-local nature of the scissors operator were obtained. These terms, not considered before in the literature, are crucial in order to obtain gauge invariance. Using the unscissored Hamiltonian, gauge invariance is obtained with the usual $\chi^{abc}(-2\omega;\omega,\omega)$ expression calculated within the velocity and length gauge.

We have presented our numerical results for GaAs using both a DFT-LDA *ab initio* calculation, with the augmented plane wave plus local orbital all-electron method as given by WIEN2K [BSM$^+$01], and a plane-wave pseudopotential scheme given by the ABINIT code [GBC$^+$02]. Besides providing a numerical demonstration of gauge invariance for the unscissored and the scissored Hamiltonian calculations, we have shown the kind and size of error when one neglect the non-local nature of the pseudopotentials, it affects not only the strength of the spectrum, but also its line shape. Our results compare qualitatively well to previous works of other authors and, in particular, with

the experimental data. However, the details of each approach used show that the calculation of the nonlinear response is a nontrivial matter, and better calculations of $\chi^{abc}(-2\omega;\omega,\omega)$ using more sophisticated means are still to be sought.

## 2.6 Appendix

In this Appendix we derive several results related to the scissors operator $S(\mathbf{r},\mathbf{p})$ of Eq. (2.7). First we sketch some well known results, for which we follow Aversa and Sipe [AS95], and Blount [Blo62]. We write the position operator of the electron, $\mathbf{r}$, as the sum of its *interband* part $\mathbf{r}_e$ and *intraband* part $\mathbf{r}_i$, $\mathbf{r}=\mathbf{r}_e+\mathbf{r}_i$. The matrix elements of $\mathbf{r}_e$ are simply given by [AS95]

$$\langle n\mathbf{k}|\mathbf{r}_e|m\mathbf{k}'\rangle = \delta(\mathbf{k}-\mathbf{k}')(\mathbf{r}_e)_{nm} \rightarrow \mathbf{r}_{nm} = \frac{\mathbf{p}_{nm}}{im\omega_{nm}} = \frac{\mathbf{v}_{nm}}{i\omega_{nm}} \quad n\neq m, \tag{2.43}$$

where the canonical momentum matrix elements, $\mathbf{p}_{nm}$, are calculated according to

$$\langle n\mathbf{k}|\mathbf{p}|m\mathbf{k}'\rangle = \delta(\mathbf{k}-\mathbf{k}')\mathbf{p}_{nm} = \delta(\mathbf{k}-\mathbf{k}')\int d^3r\psi^*_{n\mathbf{k}}(\mathbf{r})(-i\hbar\boldsymbol{\nabla})\psi_{m\mathbf{k}}(\mathbf{r}),$$

and one actually uses its following property [AS95],

$$\langle n\mathbf{k}|[\mathbf{r}_i,\mathcal{O}]|m\mathbf{k}'\rangle = i\delta(\mathbf{k}-\mathbf{k}')(\mathcal{O}_{nm})_{;\mathbf{k}}, \tag{2.44}$$

where $\mathcal{O}$ is an operator and $(\mathcal{O}_{nm})_{;\mathbf{k}}$ is the generalized derivative of its matrix elements, i.e. Eq. (2.38) for $r^b_{nm;k^a}$. As discussed by Nastos et al. [NOSS05], both $\mathbf{r}_{nm}$, (Eq. (2.43)), and its generalized derivative $\mathbf{r}_{nm;\mathbf{k}}$, (Eq. (2.38)), are evaluated using the unscissored energies.

Now we derive Eq. (2.23). We take matrix elements of Eq. (2.12) and use Eq. (2.7) to write

$$\begin{aligned}
\mathbf{v}^S_{nm} &= -\frac{i}{\hbar}\langle n\mathbf{k}|(\mathbf{r}S(\mathbf{r},\mathbf{p})-S(\mathbf{r},\mathbf{p})\mathbf{r})|m\mathbf{k}\rangle \\
&= -i\Delta\Big((1-f_m)-(1-f_n)\Big)\langle n\mathbf{k}|\mathbf{r}|m\mathbf{k}\rangle \\
&= i\Delta f_{mn}\mathbf{r}_{nm} \\
&= \frac{\Delta f_{mn}}{m\omega_{nm}}\mathbf{p}_{nm}\ ;\ n\neq m
\end{aligned} \tag{2.45}$$

where we used Eq. (2.43). Then the matrix elements of Eq. (2.13) reduce to

$$\begin{aligned}
\mathbf{v}^{\Sigma}_{nm} &= \big(1+\frac{\Delta f_{mn}}{\omega_{nm}}\big)\langle n\mathbf{k}|\frac{\mathbf{p}}{m}|m\mathbf{k}\rangle \\
&= \big(\frac{\omega_{nm}+\Delta f_{mn}}{\omega_{nm}}\big)\mathbf{v}_{nm} = \big(\frac{\omega^S_n-\omega^S_m}{\omega_{nm}}\big)\mathbf{v}_{nm} \\
&= \frac{\omega^S_{nm}}{\omega_{nm}}\mathbf{v}_{nm}\ ;\ n\neq m \qquad (2.46)
\end{aligned}$$

where we used Eq. (2.8); thus Eq. (2.46) is Eq. (2.23).

In order to prove Eq. (2.21), we start with the matrix elements of $\mathcal{F}^{ab}$, Eq. (2.18), which we write as

$$\mathcal{F}^{ab}_{nm} = \langle n\mathbf{k}|\big([r^a_i, v^{S,b}] + [r^a_e, v^{S,b}]\big)|m\mathbf{k}\rangle.$$

The interband part is

$$\begin{aligned}
\langle n\mathbf{k}|[r^a_e, v^{S,b}]|m\mathbf{k}\rangle &\equiv \mathcal{F}^{ab}_{e,nm} = \sum_\ell \Big(r^a_{e,n\ell}v^{S,b}_{\ell m} - v^{S,b}_{n\ell}r^a_{e,\ell m}\Big) \\
&= i\Delta \sum_{\ell\neq(mn)} \Big(f_{m\ell}r^a_{n\ell}r^b_{\ell m} - f_{\ell n}r^b_{n\ell}r^a_{\ell m}\Big), \qquad (2.47)
\end{aligned}$$

where we used Eq. (2.43) and Eq. (2.45). For the intraband part we use Eq. (2.44) and Eq. (2.45) to simply write

$$\langle n\mathbf{k}|[r^a_i, v^{S,b}]|m\mathbf{k}\rangle \equiv \mathcal{F}^{ab}_{i,nm} = iv^{S,b}_{nm;k^a} = \Delta f_{nm}r^b_{nm;k^a}. \qquad (2.48)$$

Substituting Eq. (2.47) and Eq. (2.48) we find

$$\mathcal{F}^{ab}_{nm} = i\Delta \sum_{\ell\neq(mn)} \Big(f_{m\ell}r^a_{n\ell}r^b_{\ell m} - f_{\ell n}r^b_{n\ell}r^a_{\ell m}\Big) + \Delta f_{nm}r^b_{nm;k^a}. \qquad (2.49)$$

We see that for $n=m$, the intraband contribution $\mathcal{F}^{ab}_{i,nn}=0$. Whereas the interband part reduces to

$$\mathcal{F}^{ab}_{nn} = \mathcal{F}^{ab}_{e,nn} = i\Delta\sum_{m\neq n} f_{nm}(r^a_{nm}r^b_{mn} + r^b_{nm}r^a_{mn}), \qquad (2.50)$$

giving Eq. (2.21).

Now we take matrix elements of $[r^a, \mathcal{F}^{bc}]$, separating $r^a = r^a_i + r^a_e$. Then the interband part gives

$$[r^a_e, \mathcal{F}^{bc}]_{nn} = \sum_{m\neq n}\big(r^a_{nm}\mathcal{F}^{bc}_{mn} - \mathcal{F}^{bc}_{nm}r^a_{mn}\big), \qquad (2.51)$$

while the intraband part gives

$$[r_i^a, \mathcal{F}^{bc}]_{nn} = i\mathcal{F}^{bc}_{nn;a} = i\frac{\partial}{\partial k^a}\mathcal{F}^{bc}_{nn} = i\frac{\partial}{\partial k^a}\mathcal{F}^{bc}_{e,nn}, \tag{2.52}$$

where we used Eq. (2.50). Then Eq. (2.51) and Eq. (2.52) are used to obtain Eq. (2.29).

Now we derive Eq. (2.24), using Eq. (2.46), $\omega^S_{mn} = \omega_{mn} - f_{mn}\Delta$, Eq. (2.43) and Eq. (2.21), Eq. (2.19) reduces to

$$\begin{aligned}
\zeta^{ab} &= \frac{e^2}{\hbar}\int\frac{d^3k}{8\pi^3}\sum_{m\neq n} f_n\omega^S_{mn}\frac{v^a_{nm}v^b_{mn}+v^a_{mn}v^b_{nm}}{\omega^2_{mn}} - \frac{e^2 n}{m}\delta_{ab} \\
&= \frac{e^2}{\hbar}\int\frac{d^3k}{8\pi^3}\sum_{m\neq n} f_n\omega_{mn}\frac{v^a_{nm}v^b_{mn}+v^a_{mn}v^b_{nm}}{\omega^2_{mn}} - \frac{e^2 n}{m}\delta_{ab} \\
&- \frac{e^2\Delta}{\hbar}\int\frac{d^3k}{8\pi^3}\sum_{m\neq n} f_n f_{mn}\frac{v^a_{nm}v^b_{mn}+v^a_{mn}v^b_{nm}}{\omega^2_{mn}} \\
&= -e^2\int\frac{d^3k}{8\pi^3}\sum_n f_n\Big(\frac{\delta_{ab}}{m} - \sum_{m\neq n}\frac{v^a_{nm}v^b_{mn}+v^a_{mn}v^b_{nm}}{\hbar\omega_{mn}}\Big) \\
&+ \frac{e^2\Delta}{\hbar}\int\frac{d^3k}{8\pi^3}\sum_n f_n\sum_{m\neq n} f_{nm}\Big(r^a_{nm}r^b_{mn}+r^a_{mn}r^b_{nm}\Big) \\
&= -e^2\int\frac{d^3k}{8\pi^3}\sum_n f_n\left[\frac{1}{m^*_n}\right]^{ab} - \frac{ie^2}{\hbar}\int\frac{d^3k}{8\pi^3}\sum_n f_n\mathcal{F}^{ab}_{nn},
\end{aligned} \tag{2.53}$$

where

$$\left[\frac{1}{m^*_n}\right]^{ab} = \frac{\delta_{ab}}{m} - \sum_{m\neq n}\frac{v^a_{nm}v^b_{mn}+v^a_{mn}v^b_{nm}}{\hbar\omega_{mn}}, \tag{2.54}$$

is the effective mass tensor. Identifying the second term on the right hand side of Eq. (2.53) as $-\eta^{ab}$ (see Eq. (2.20)), leads to

$$\zeta^{ab} + \eta^{ab} = -e^2\int\frac{d^3k}{8\pi^3}\sum_n f_n\left[\frac{1}{m^*_n}\right]^{ab}. \tag{2.55}$$

Substituting Eq. (2.55) in Eq. (2.22) gives Eq. (2.24).

Chapter 3

# Optical injection current at semiconductor surfaces

---

## Contents

**3.1 Summary** . . . . . . . . . . **33**
**3.2 Introduction** . . . . . . . . . . **34**
**3.3 Theory** . . . . . . . . . . **36**
**3.4 Computational details** . . . . . . . . . . **41**
**3.5 Results** . . . . . . . . . . **42**
3.5.1 Si(111) surfaces . . . . . . . . . . 44
3.5.2 GaAs(110) surfaces . . . . . . . . . . 45
3.5.3 Surface vs. bulk experimental detection estimate . . . . 46
**3.6 Conclusions** . . . . . . . . . . **47**
**3.7 Appendix** . . . . . . . . . . **48**

---

## 3.1 Summary

We present a study of the optical coherent control of injection currents at surfaces of cubic semiconductors. We propose and use this optical effect as a surface sensitive probe of crystals with bulk inversion symmetry or $\bar{6}m2$, $\bar{6}$, and $\bar{4}\bar{3}m$ (zinc-blende) symmetry. In crystals with any of these symmetries, this effect vanishes in the bulk, but it is allowed in surface regions owing to the local break of symmetry. We present the results of *ab initio* calculations for optically injected currents at the clean Si(111)$(2\times1)$ surface, and clean and Sb-covered GaAs(110)$(1\times1)$ surfaces. The reconstruction of each of these surfaces is well understood. The effects are shown to be sensitive to surface structure, and the experimental signals that the injected currents should generate can be

understood in terms of the surface electronic structure. Calculated magnitudes indicate that the currents should be observable, and the calculated spectra of all of the surfaces show interesting behavior as a function of the energy of the incident light.

## 3.2 Introduction

The study and control of the structure and chemistry of surfaces is of scientific and technological importance. Optical probes are of particular interest because they do not require a high vacuum environment, and experiments can be performed at interfaces where other techniques are impossible to use. However, because of the long wavelength of the incident light, surface sensitivity typically only arises when the effect studied is absent in the underlying bulk. Two examples are reflectance anisotropy spectroscopy (RAS) [WMCF05, Ric96], and surface second harmonic generation (SSHG) [DMG01, LDE+00]. Both have been employed as passive probes of clean and adsorbate-covered surfaces. In this chapter we introduce a surface optical effect that offers the potential, not only for the study of surfaces, but also for the control of chemical reactions there. It relies on the breaking of the bulk symmetry at the surface. In some excitation scenarios a current can be injected in the surface region by an incident optical field, with a variation in time that is driven by the time dependence of the incident intensity. Within the susceptibility framework of optical response this effect is nonlinear, but its amplitude scales linearly with the incident intensity. In pulsed excitation it can be detected by the emission of THz radiation due to the acceleration of the charges [lam]. It can also be studied, in both pulsed and CW excitation, by measuring a voltage induced along the surface [lam].

The simplest such phenomenon is below band-gap optical rectification, where a polarization is induced by an optical field at incident frequencies below the energy gap of a semiconductor or insulator; the polarization follows the incident intensity in its time evolution, and its time derivative yields a current that can produce THz radiation. This current, which vanishes for CW irradiation, is not our concern here. Rather, we focus on incident light with frequencies above the band gap, where not only virtual but also real excitations are allowed. For such incident fields there are, approximately, two currents that can arise [NOSS05, SS00, nas]: The first is a shift current, $\mathbf{J}_{shift}$, associated with the motion of the center of charge of the electrons as they are injected from the valence to the conduction bands; it is approximately

proportional to the pulse intensity. The second is an injection current, $\mathbf{J}_{inj}$, associated with a polar asymmetry of the injected electrons to the conduction band and holes in reciprocal space; in this case, $d\mathbf{J}_{inj}/dt$ is approximately proportional to the pulse intensity, and the injection can be understood as a quantum interference between different absorption pathways associated with different linear polarizations of the light. In both effects the energy increase of carriers is provided by the electromagnetic field, while the increase in momentum is provided by the crystal lattice. In the bulk of crystals without inversion symmetry the injection and shift currents fall into the phenomenological categories of a circular photogalvanic effect and a linear photogalvanic effect respectively [Stu92], and their description has been formulated in the context of nonlinear optics [NOSS05, SS00, AS96, AS95, nas]. As shorter pulses are considered, the distinction between these terms (and optical rectification, which, of course, still exists above the band gap) becomes less sharp [nas]. In the CW limit, the injection current in a bulk medium is characterized by a third rank tensor $\eta_2^{abc}$

$$\dot{J}^a_{inj} = 2\eta_2^{abc}(0;\omega,-\omega)E^b(\omega)E^c(-\omega), \tag{3.1}$$

where the superscripts indicate Cartesian components that are to be summed over if repeated, and $\mathbf{E}(\omega)$ indicates the electric field amplitude at the incident frequency $\omega$; in the independent particle approximation the coefficient $\eta_2^{abc}$ is antisymmetric in the components $b$ and $c$, and is purely imaginary [NOSS05, SS00, nas]. For slowly varying pulses the intensity-like term $E^b(\omega)E^c(-\omega)$ can be multiplied by a function describing the time dependence of the intensity in the pulse [NOSS05, nas], and the resulting equation used to determine the injected current in the absence of scattering and space charge effects.

In this chapter we focus on the optical injection current that arise at the surfaces centrosymmetric when light incides on it. This includes not only centrosymmetric crystals (such as Si), Among centrosymmetric crystals, we have Si crystals of the clasess $\bar{6}m2$, $\bar{6}$, and $\bar{4}\bar{3}m$. The latter class includes typical III-V semiconductors such as GaAs. Notice that the different effects can be distinguished from each other by their dependence on pulse width, and from each other and from phase insensitive photovoltaic effects by their dependence on the polarization of the incident field [NOSS05, nas, notc]. We consider that current injection is the most striking of these as yet uninvestigated surface terms, since it vanishes of the bulk of many fundamental centrosymmetric semiconductors and because the opportunity it would give an experimentalist to “shoot” electrons and holes in one direction or another along the surface is

particularly exciting.

At a surface, Eq. (3.1) can be replaced by corresponding equations involving the surface injection current $\dot{\mathbf{J}}^S_{inj}$ and a surface response coefficients $\eta_2^{S,abc}$. We evaluate $\eta_2^{S,abc}$ for three structures of the well-studied Si(111) surfaces [RL99, SCC+87],and two of GaAs(110) surfaces [MAVN08]; the results demonstrate that the injection current is sensitive to surface structure. Furthermore, we show that it can be understood in a simple way in terms of the properties of electronic surface states, and it should be amenable to experimental study.

The chapter is organized as follows. In Section 3.3 we present the theory for the calculation of the surface injected current, using a new approach that is well suited for a surface calculation. Then, in Section 3.4 we present the computational details of the *ab initio* approach used in our calculations, and in Section 3.5 we present the results for the chosen surfaces. Finally, in Section 3.6 we present the conclusions.

## 3.3 Theory

In this section we derive the expressions for the generation of the injection current suitable for surfaces and interfaces. To model the semi-infinite crystal, we use a slab consisting of $N$ atomic layers inside a supercell of total height $L$ and volume $\Omega = AL$, where $A$ is the surface area of the unit cell. The supercell includes the vacuum region required to use a repeated slab scheme. In a slab calculation not only one often wants to calculate the response from one of the two halves of the slab but also from a particular layer of the slab. A convenient way to accomplish the separation of the response of any layer is through the use of the so called "cut function", $\mathcal{F}_\ell(z)$, as a top-hat cut function that selects a given layer,

$$\mathcal{F}_\ell(z) = \Theta(z - z_\ell + \Delta_\ell^b)\Theta(z_\ell - z + \Delta_\ell^f), \tag{3.2}$$

where $\Theta$ is the Heaviside function. Here, $\Delta_\ell^{f/b}$ is the distance that the $\ell$-th layer extends towards the front ($f$) or back ($b$) from its $z_\ell$ position. Thus $\Delta_\ell^f + \Delta_\ell^b$ is the thickness of layer $\ell$. The cut function was originally used by Hogan *et al.* [HDSO03] and Castillo *et al.* [CMS+03], and more recently was put on a more solid basis through a microscopic calculation of the linear optical response of a surface by Mendoza *et al.* [MNAS06]. The above scheme known as a layer-by-layer approach is successfully used to provide deeper understanding of various surface optical responses [MNAS06, MSM04, HDSO03, CMS+03]. However, for this work, the use of the layer-by-layer approach is crucial, since

it allow us to perform a physically relevant calculation for the surface injection current. The slab used to represent the aforementioned surfaces is centrosymmetric and thus $\eta_2^{abc}(\omega) = 0$ for the whole slab. Using $\mathcal{F}_\ell(z)$ for each layer gives a finite value of $\eta_2^{abc}(\omega)$, and as we will see in this section, such splitting allow us to calculate the surface value of $\eta_2^{abc}(\omega) \to \eta_2^{S,abc}(\omega)$ and thus of $\dot{\mathbf{J}}^S_{inj}$.

Lets begin by writing the polarization density of the $\ell^{th}$ layer of the slab as

$$P^{\ell,a}(\omega) = \hbar\xi^{\ell,ab}(\omega)E^b(\omega), \tag{3.3}$$

where, from the appendix,

$$\xi^{\ell,ab}(\omega) = \frac{e^2}{\hbar^2}\int\frac{d^3k}{8\pi^3}\sum_{m\neq n} f_{nm}\frac{\mathcal{R}^{\ell,a}_{nm}(\mathbf{k})r^b_{mn}(\mathbf{k})}{\omega_{mn}(\mathbf{k})-\omega-i\eta}, \tag{3.4}$$

is related to the imaginary part of the $\ell^{th}$ layer of the linear optical susceptibility. In here we take $\eta \to 0$, $f_{nm} = f_n - f_m$ with $f_n$ the Fermi occupation factor that, for a clean, cold semiconductor, equals one if the band $n$ is occupied (valence band $n = c$) and zero if the band is empty (conduction band $n = c$), regardless of the value of $\mathbf{k}$, and thus $f_{nm}$ does not depend on $\mathbf{k}$; $\hbar\omega_{mn}(\mathbf{k}) = \hbar\omega_m(\mathbf{k}) - \hbar\omega_n(\mathbf{k})$ is the difference of energies between states $m$ and $n$ for a crystal momentum $\mathbf{k}$. The position operator matrix elements are obtained through the relationship $r^a_{nm}(\mathbf{k}) = v^a_{nm}(\mathbf{k})/(i\omega_{nm}(\mathbf{k}))$ $(n \neq m)$, where $v^a_{nm}(\mathbf{k})$ are the standard velocity matrix elements. However, $\mathcal{R}^a_{nm}(\mathbf{k}) = \mathcal{V}^a_{nm}(\mathbf{k})/(i\omega_{nm}(\mathbf{k}))$ $(n \neq m)$, where

$$\mathcal{V}^{\ell,a}_{nm}(\mathbf{k}) = \frac{1}{m_e}\int d^3r\,\psi^*_{n\mathbf{k}}(\mathbf{r})\mathcal{P}^{\ell,a}\psi_{m\mathbf{k}}(\mathbf{r}), \tag{3.5}$$

is the modified velocity matrix elements, through which the polarization of the $\ell^{th}$ layer is obtained [MNAS06]. Here, $\psi_{n\mathbf{k}}(\mathbf{r})$ is the wave function normalized with the volume of the supercell and $m_e$ is the electron mass. Also,

$$\mathcal{P}^{\ell,a} = \frac{\mathcal{F}_\ell(z)p^a + p^a\mathcal{F}_\ell(z)}{2}, \tag{3.6}$$

with $p^a = -i\hbar\nabla^a$, the top-hat cut function $\mathcal{F}_\ell(z)$ selects the $\ell^{th}$ layer of the slab. If we take $\mathcal{F}_\ell(z) = 1$, then $\mathcal{P}^{\ell,a} \to p^a$, from Eq. (3.5) we obtain that $\mathcal{V}^{\ell,a}_{nm}(\mathbf{k}) \to v^a_{nm}(\mathbf{k})$ or $\mathcal{R}^{\ell,a}_{nm}(\mathbf{k}) \to r^a_{nm}(\mathbf{k})$. We remark that replacing $\mathcal{R}^{\ell,a}_{nm}(\mathbf{k})$ by $r^a_{nm}(\mathbf{k})$ in Eq. (3.4) would give the standard expression for the linear susceptibility [SS00] through which one can calculate the polarization of the whole

slab or of a bulk semiconductor. We mention that the dielectric response tensor for the $\ell^{th}$ layer is given by $\varepsilon^{\ell,ab} = \delta^{ab} + 4\pi\hbar\xi^{\ell,ab}$. In the context of RAS, it is analyzed in Ref. [MNAS06] for a hydrogenated Si(100) surface.

The rate at which the electromagnetic field does work on the $\ell^{th}$ layer of the material medium (per unit volume) is given by $\mathbf{J}^\ell \cdot \mathbf{E} = \dot{\mathbf{P}}^\ell \cdot \mathbf{E}$, and its time average is related to the photocarrier generation rate of the $\ell^{th}$ layer, $\dot{n}^\ell$, by

$$\dot{n}^\ell = \frac{1}{\hbar\omega}\langle \dot{\mathbf{P}}^\ell \cdot \mathbf{E}\rangle, \tag{3.7}$$

where $\langle \cdots \rangle$ denotes the time average. Writing

$$\mathbf{E}(t) = \mathbf{E}(\omega)e^{-i\omega t} + \mathbf{E}^*(\omega)e^{i\omega t}, \tag{3.8}$$

where $\mathbf{E}^*(\omega) = \mathbf{E}(-\omega)$, and the $\ell^{th}$ layer polarization as

$$\mathbf{P}^\ell(t) = \mathbf{P}^\ell(\omega)e^{-i\omega t} + \mathbf{P}^{\ell^*}(\omega)e^{i\omega t}, \tag{3.9}$$

we get

$$\dot{n}^\ell = \frac{-i}{\hbar}(\mathbf{P}^\ell(\omega)\cdot\mathbf{E}^*(\omega) - \mathbf{P}^{\ell^*}(\omega)\cdot\mathbf{E}(\omega)), \tag{3.10}$$

where the terms proportional to $2\omega$ (not shown) average out to zero. Before we proceed, a word of caution is required. The electric field of Eq. (3.10) is implicitly taken as uniform in the region of interest. Clearly this is inappropriate for the $z$ component of the electric field, which for semiconductors can change by orders of magnitude as one moves from vacuum to the semiconductor. Thus, all aspects of the optical response at an interface due to this component of the electric field would require a self-consistent calculation of the variation of $E^z$ across the surface region [SSP98]. Although the calculation of this variation is important, we do not address it here. Instead, we focus on the simplest experimental geometry of normal incidence. Then, since the electric field lies in the plane of the interface, it can be taken, as uniform through the interface region, neglecting local field corrections which is typically done even in bulk calculations,

Using Eq. (3.3) in Eq. (3.10), we obtain

$$\dot{n}^\ell = \frac{-i}{2}\left(\xi^{\ell,bc}E^c(\omega)E^b(-\omega) - \xi^{\ell,bc^*}E^c(-\omega)E^b(\omega) + b \leftrightarrow c\right), \tag{3.11}$$

where we have symmetrized the dummy Cartesian indices $b$ and $c$ using $b \leftrightarrow c$ that denotes the exchange of $b$ and $c$ of the previous terms. Using Eq. (3.4),

we obtain

$$\begin{aligned}\dot{n}^\ell &= \frac{-e^2}{2\hbar^2}\int\frac{d^3k}{8\pi^3}\sum_{m\neq n} f_{nm}\Big(i\Big(\frac{\mathcal{R}^{\ell,b}_{nm}(\mathbf{k})r^c_{mn}(\mathbf{k})}{\omega_{mn}(\mathbf{k})-\omega-i\eta}-\frac{\mathcal{R}^{\ell,c}_{mn}(\mathbf{k})r^b_{nm}(\mathbf{k})}{\omega_{mn}(\mathbf{k})-\omega+i\eta}\Big)\\ &\times\ E^b(-\omega)E^c(\omega)+\text{c.c.}\Big), \end{aligned}\tag{3.12}$$

with c.c denoting the complex conjugate of the previous term. We used $r^a_{nm}(\mathbf{k}) = r^{a^*}_{mn}(\mathbf{k})$ and $\mathcal{R}^a_{nm}(\mathbf{k}) = \mathcal{R}^{a^*}_{mn}(\mathbf{k})$. We see that the terms inside the integral over $\mathbf{k}$ and the summation over states are proportional to the rate of photocarriers generated by the electric field between bands $m$ and $n$ at point $\mathbf{k}$, for the $\ell^{th}$ layer. Thus, from Eq. (3.12) we can construct the injection current density of the $\ell^{th}$ layer, $\dot{J}^{\ell,a}$, as

$$\begin{aligned}\dot{J}^{\ell,a}_{inj} &= \frac{-e^2}{2\hbar^2}\int\frac{d^3k}{8\pi^3}\sum_{m\neq n} f_{nm}\Delta^{\ell,a}_{mn}(\mathbf{k})\Big(i\Big(\frac{\mathcal{R}^{\ell,b}_{nm}(\mathbf{k})r^c_{mn}(\mathbf{k})}{\omega_{mn}(\mathbf{k})-\omega-i\eta}\\ &-\ \frac{\mathcal{R}^{\ell,c}_{mn}(\mathbf{k})r^b_{nm}(\mathbf{k})}{\omega_{mn}(\mathbf{k})-\omega+i\eta}\Big)E^b(-\omega)E^c(\omega)+\text{c.c.}\Big),\end{aligned}$$

where we have introduced the real function $e\Delta^{\ell,a}_{mn} = e(\mathcal{V}^{\ell,a}_{mm} - \mathcal{V}^{\ell,a}_{nn})$, that represents the current created in the $\ell$-th layer by bands $m$ and $n$, with $\mathcal{V}^{\ell,a}_{mm}$ the electron velocity along $a$ for band $m$ and layer $\ell$-th, The Fermi factor $f_{nm}$ forces $n \neq m$ and so if $n = c$ then $m = v$ and viceversa, thus the minus sign in $e\Delta^{\ell,a}_{mn}$ simply says that we are including the current created by the electron/hole pair created at $\mathbf{k}$ for the $\ell$-th layer. The equation above is written as

$$\dot{J}^{\ell,a}_{inj} = \eta^{\ell,abc}(0;\omega,-\omega)E^b(\omega)E^c(-\omega) + \text{c.c.},\tag{3.13}$$

where

$$\begin{aligned}\eta^{\ell,abc}(0;\omega,-\omega) &= \frac{i|e|^3}{2\hbar^2}\int\frac{d^3k}{8\pi^3}\sum_{m\neq n} f_{nm}\Delta^{\ell,a}_{mn}(\mathbf{k})\Big(\frac{\mathcal{R}^{\ell,c}_{nm}(\mathbf{k})r^b_{mn}(\mathbf{k})}{\omega_{mn}(\mathbf{k})-\omega-i\eta}\\ &-\ \frac{\mathcal{R}^{\ell,b}_{mn}(\mathbf{k})r^c_{nm}(\mathbf{k})}{\omega_{mn}(\mathbf{k})-\omega+i\eta}\Big).\end{aligned}\tag{3.14}$$

Writing $\eta^{\ell,abc}(0;-\omega,\omega) = \eta^{\ell,abc}_{\mathrm{r}}(0;-\omega,\omega) + i\eta^{\ell,abc}_{\mathrm{i}}(0;-\omega,\omega)$, and using (see the appendix),

$$\begin{aligned}\eta^{\ell,abc}(0;-\omega,\omega) &= -\eta^{\ell,acb}(0;-\omega,\omega)\\ \eta^{\ell,abc}(0;-\omega,\omega) &= \eta^{\ell,abc^*}(0;\omega,-\omega),\end{aligned}$$

Eq. (3.13) reduces to

$$
\begin{aligned}
j^{\ell,a} &= 2i\eta_{\mathrm{i}}^{\ell,abc}(0;\omega,-\omega)E^b(\omega)E^c(-\omega) \\
&\equiv 2\eta_2^{\ell,abc}(0;\omega,-\omega)E^b(\omega)E^c(-\omega),
\end{aligned}
\tag{3.15}
$$

where from the appendix $\eta_2^{\ell,abc}(0;\omega,-\omega) = i\eta_{\mathrm{i}}^{\ell,abc}(0;\omega,-\omega)$ is given by

$$
\begin{aligned}
\eta_2^{\ell,abc}(0;\omega,-\omega) &= \frac{i\pi|e|^3}{2\hbar^2}\int\frac{d^3k}{8\pi^3}\sum_{m\neq n} f_{nm}\Delta_{mn}^{\ell,a}(\mathbf{k})\mathrm{Im}\Big[\mathcal{R}_{mn}^{\ell,c}(\mathbf{k})r_{nm}^b(\mathbf{k}) \\
&+ \mathcal{R}_{nm}^{\ell,b}(\mathbf{k})r_{mn}^c(\mathbf{k})\Big]\delta(\omega_{mn}(\mathbf{k})-\omega),
\end{aligned}
\tag{3.16}
$$

which shows that $\eta_2^{\ell,abc}(0;\omega,-\omega)$ is a purely imaginary tensor and that is antisymmetric in the last two Cartesian indices. This constitutes the main analytic result of this chapter.

Replacing $\mathcal{R}_{mn}^{\ell,c}(\mathbf{k})$ by $r_{mn}^c(\mathbf{k})$ , $\mathcal{R}_{nm}^{\ell,b}(\mathbf{k})$ by $r_{nm}^b(\mathbf{k})$ and $\Delta_{nm}^{\ell,a}(\mathbf{k})$ by $\Delta_{nm}^a(\mathbf{k})$ in the equation above one would obtain the expression for $\eta_2^{abc}(0;\omega,-\omega)$ valid for a bulk semiconductor (see Eq. (3.29),in the appendix) [SS00]. However, such a replacement is equivalent to taking $\mathcal{F}_\ell(z) = 1$ for all $\ell$, i.e. the whole slab, and thus the same bulk expression could be used to calculate the response of the full slab. Nevertheless, for a centrosymmetric system, whether bulk or slab, one can always choose the matrix elements of $r_{nm}^a(\mathbf{k})$ to be real functions, and thus $\eta_2^{abc}(0;\omega,-\omega) = 0$ (see also Eq. (3.29)). Indeed, for a centrosymmetric system there is no injection current [Sau96, SS00], however for a surface there may be a finite injection current since the surface is not centrosymmetric. Therefore, the use of $\mathcal{F}_\ell(z)$ readily allow us to get a finite $\eta_2^{\ell,abc}(0;\omega,-\omega)$ from Eq. (3.16).

In order to define the injection current suitable for a surface, we take into account the following observations. As we mentioned before, the slab that we use to represent the semi-infinite system consists of $N$ layers, where the value of $N$ is such that for $N \geq N_c$ the value of $\eta_2^{\ell,abc}(0;\omega,-\omega)$ does not change any more. Also, one should expect that for a layer, $\tilde{\ell}$, near or at the middle ($\ell_B$) of the slab, where the spatial environment is centrosymmetric, $\eta_2^{\tilde{\ell},abc}(0;\omega,-\omega) \approx \eta_2^{\ell_B,abc}(0;\omega,-\omega) = 0$. The $\mathbf{k}$ integration in Eq. (3.16) is normalized by $\Omega$. Then we could use $(1/A)\sum_{\ell=1}^{\ell_B}\Omega\eta_2^{\ell,abc}(0;\omega,-\omega)$, as a surface response. Now, $\Omega/A = L$ where $L = L_s + L_v$ with $L_s$ and $L_v$ being the length of the slab and the vacuum, respectively. The value of $L_v$ is such that after some minimum value, that avoids the interference between slabs of contiguous unit cells, the calculated response for a given $L_s$ does not change. Indeed,

choosing inappropriate values for $L_v$ leads to inaccurate results as analyzed in Ref. [MNAS06] for the linear optical response. On the other hand, $L_s$ comprise all the layers of the slab, but as we would expect some of them have zero response due to their centrosymmetric environment. Therefore, we find that the most appropriate length needed to define the surface response is the total thickness that comprise all the layers that do have a $\eta_2^{\ell,abc}(0;\omega,-\omega) \neq 0$.

Let the surface response be

$$\eta_2^{S,abc}(0;\omega,-\omega) = L_{\text{eff}} \sum_{\ell=1}^{\ell_{\text{eff}}} \eta_2^{\ell,abc}(0;\omega,-\omega) = \sum_{\ell=1}^{\ell_{\text{eff}}} \tilde{\eta}_2^{\ell,abc}(0;\omega,-\omega), \tag{3.17}$$

with $\tilde{\eta}_2^{\ell,abc}(0;\omega,-\omega) = L_{\text{eff}}\eta_2^{\ell,abc}(0;\omega,-\omega)$, where $L_{\text{eff}}$ is the thickness of all the layers that "effectively" contribute to the sum in th equation above, and $\ell_{\text{eff}}$ the last layer (counting from the surface) for which $\eta_2^{\ell,abc}(0;\omega,-\omega) \neq 0$. Thus only the layers close to the surface, will contribute to $\eta_2^{S,abc}(0;\omega,-\omega)$ since it is only close to the surface where the centrosymmetry is broken. Finally,

$$\dot{J}^{S,a} = 2\eta_2^{S,abc}(0;\omega,-\omega)E^b(\omega)E^c(-\omega), \tag{3.18}$$

gives the surface injection current, where both $\dot{J}^{S,a}$ and $\eta_2^{S,abc}(0;\omega,-\omega)$ have the units of their bulk counterparts times the length as expected for a surface response.

## 3.4 Computational details

Our layer-by-layer analysis is done by using the well known ABINIT plane-wave code [XBC+02]. A self-consistent calculation is first made to determine the Kohn-Sham potential for the relaxed surface structures. We use the separable Hartwigsen-Goedecker-Hutter (HGH) pseudopotentials [HGH98] within the LDA as parametrized by Goedecker et al. [GTH96]. In our calculations for Si and GaAs surfaces, we exclude the semi-core states, as it is usually done, though they can be included with more computational effort. Once the Kohn-Sham potential is determined, we find the wavefunctions, and then the matrix elements are calculated for **k**-points on a specially determined tetrahedral grid. This grid is used in the integrals of Eq. (3.16), that are conveniently done by a linear analytic tetrahedral integration method [NRSM+07]. A set of 112 **k**-points in the irreducible surface Brillouin zone (SBZ) and a cut-off energy of 10 Ha is used for each of the surfaces. With these parameters, and the number

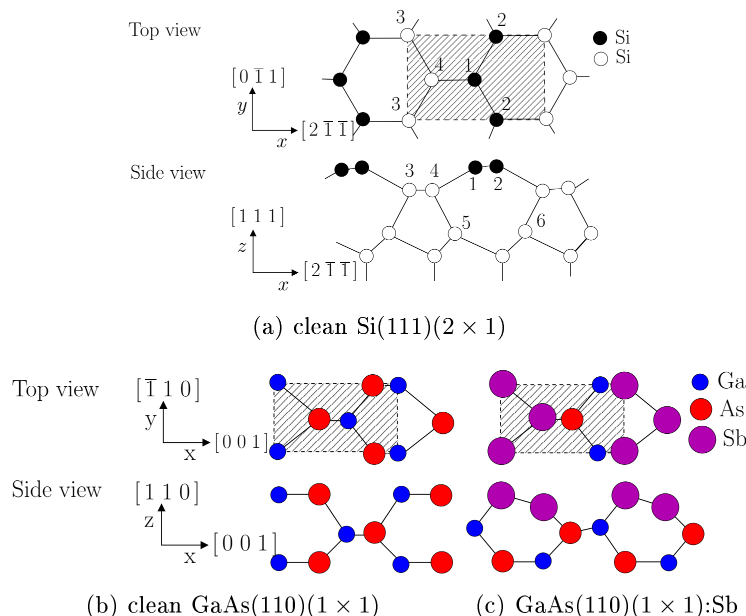


Figure 3.1: Top and side views of the (a) clean Si(111)(2 × 1), (b) clean GaAs(110)(1 × 1) and (c) Sb-covered GaAs(110)(1 × 1) surfaces. The shaded areas represents the unit cells for the corresponding surfaces.

of layers in the slab, $N_c$, shown in Table 3.1, we find well converged results for all the responses of interest in this work. The required matrix elements are calculated as indicated in Ref. [MNAS06]. We use the scissors correction, to correct the LDA energy gap underestimation with respect to the experimental value, that for the calculated responses, only implies the rigid shift of the spectra by the scissors correction $\mathcal{S}$ [NOSS05, CME+09]. We have neglected local field and excitonic effects; including any of these is a numerical challenge.

## 3.5 Results

In this section we present our results using the full-band electronic scheme developed in section 3.3. The chosen systems are the clean Si(111)(2 × 1) and the clean and Sb covered GaAs(110) surfaces (see Fig. 3.1). We have considered these surfaces since their reconstruction are well understood and easily reproducible experimentally. The nonzero (symmetry-allowed) components of $\eta_2^{S,abc}(0;\omega,-\omega)$ for all the surfaces under consideration are the $yyx$, $xzx$ and $yzy$ components. The last two take places with a field perpendic-

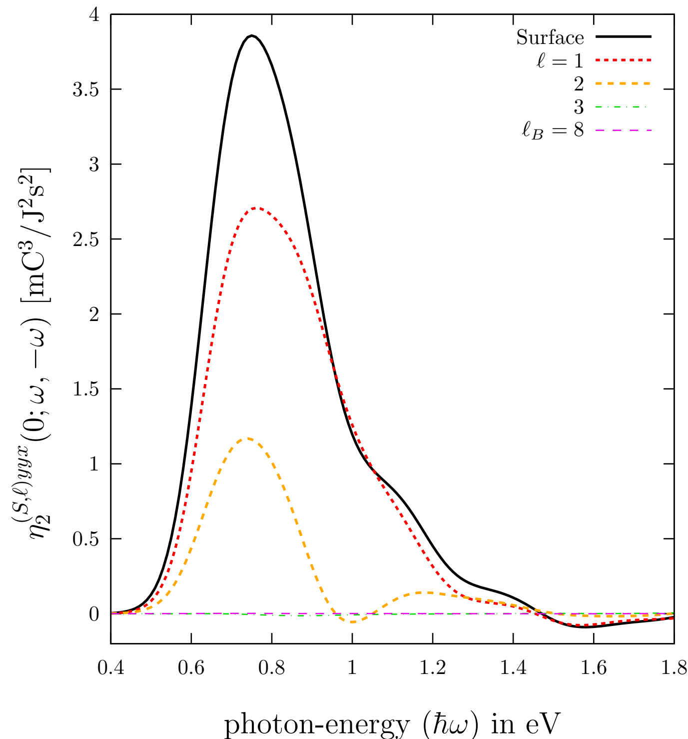


Figure 3.2: Plot of $\eta_2^{S,yyx}(0;\omega,-\omega)$ for a clean Si(111)(2 $\times$ 1) surface and the layer resolved contribution, $\tilde{\eta}_2^{\ell,yyx}(0;\omega,-\omega)$, for several of its layers. Note that for $\ell \geq 3$, $\tilde{\eta}_2^{\ell,yyx}(0;\omega,-\omega) \sim 0$ and that $\tilde{\eta}_2^{\ell_B,yyx}(0;\omega,-\omega) = 0$.

ular to the surface, and as discussed above, it requires a detailed calculation of $E^z(\omega)$ [SSP98], thus we only present results for the first component. The $\eta_2^{S,yyx}(0;\omega,-\omega)$ tensor component, requires a circularly polarized field and parallel to the surface, i.e. at normal incidence. For instance, taking $E^x(\omega) = E_0(\omega)$ and $E^y(\omega) = E_0(\omega)e^{i\phi}$, from Eq. (3.18)

$$\dot{J}^{S,y} = 4i\eta_2^{S,yyx}(0;\omega,-\omega)|E_0(\omega)|^2 \sin\phi, \tag{3.19}$$

from where it follows that the rate of injected current along $y$ is proportional to the phase difference of the field components through a sine dependence.

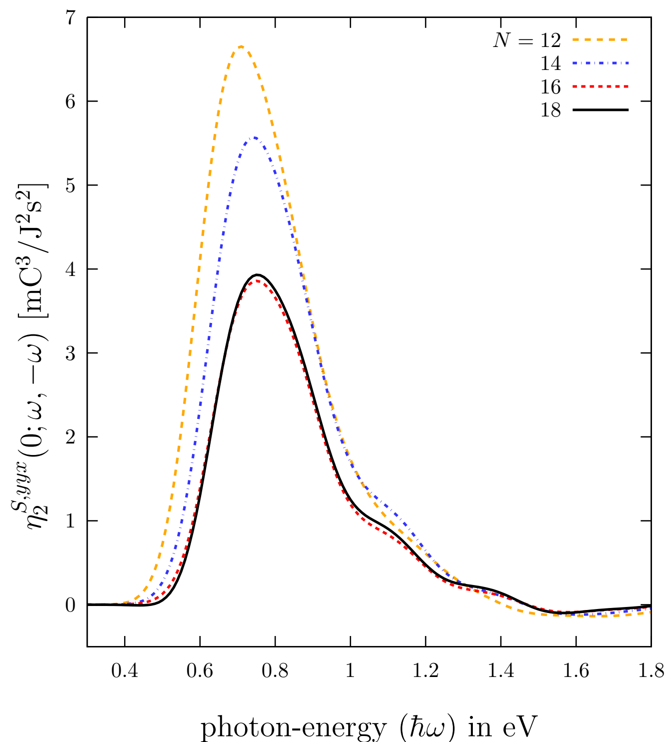


Figure 3.3: Plot of $\eta_2^{S,yyx}(0;\omega,-\omega)$ for a clean Si(111)(2×1) surface for several values of $N$, notice that the results are converged for $N_c = 16$.

### 3.5.1 Si(111) surfaces

We first show the results for a clean cleaved Si(111) surface. This surface has a $2 \times 1$ Pandey reconstruction which is characterized by buckled zigzag chains along the $y$ ($[01\bar{1}]$) direction [Pan82, RL99]. The upper atoms labelled 2 in Fig. 3.1, show $sp^3$-like bonding with one orbital predominantly filled, while the lower atoms labelled 1, exhibit $sp^2$-like bonding with their $p_z$ orbitals predominantly empty. From Eq. (3.19) it follows that the rate of injected current along the $y$ direction is possible because excited electrons can move along the zigzag chains of atoms.

For a clean Si(111) $2\times1$ surface we plot in Fig. 3.2, the spectral dependence of $\eta_2^{S,yyx}(0;\omega,-\omega)$ and $\tilde{\eta}_2^{\ell,yyx}(0;\omega,-\omega)$ for several values of $\ell$ corresponding to the top most atomic layer ($\ell = 1$) composed by the dimers, the next two atomic layers $\ell = 2,3$ and the bulk-like layer at $\ell_B = 8$. We see that the

surface response starts rising sharply around 0.5 eV, which corresponds to the transitions between the surface states, reaching its maximum at 0.75 eV and followed by a sharp decline. Above 1.75 eV the signal is basically zero. The calculated layer-by-layer responses convincingly demonstrates that the surface signal is dominated by the first two atomic layers, and that after the third layer $\tilde{\eta}_2^{\ell\geq 3,yyx}(0;\omega,-\omega)\approx 0$ is almost zero. Therefore $L_{\text{eff}}$ would correspond to the total thickness of the first 3 layers and $\ell_{\text{eff}}=3$. surprising very few atomic layers beneath the surface are required for the system to be "centrosymmetric" as far as this response is concerned. As shown in Fig. 3.2 the corresponding surface injection current occurs below the bulk band gap of Si, this is because the prominent surface energy levels appear within the gap of the projected-bulk band structure. In Fig. 3.3, we plot the calculated spectrum of $\eta_2^{S,yyx}(0;\omega,-\omega)$ for several values of $N$, where we know that $L_{\text{eff}}$ corresponds to the thickness of the first three layers of the slab from previous results. We see that the results converged for $N_c=16$ layers.

### 3.5.2 GaAs(110) surfaces

The GaAs surfaces considered here are a clean (110) and Sb covered (110) surfaces, both of them show a $(1\times1)$ reconstruction. The clean surface contains a zigzag chain of alternating Ga and As atoms along the $y$ direction, $[\bar{1}10]$, that are replaced by Sb atoms in the Sb-covered surface. In Fig. 3.4 we show the spectra of $\eta_2^{S,yyx}(0;\omega,-\omega)$ and $\tilde{\eta}_2^{\ell,yyx}(0;\omega,-\omega)$ for the first two layers of both the clean and the Sb covered GaAs(110)$(1\times1)$ surfaces. Notice the sensitivity of the signal to the different surface termination. The magnitudes of the injection current response are of the same order of magnitude and have a rich spectral behavior. It is interesting to see the different spectral features of $\eta_2^{S,yyx}(0;\omega,-\omega)$ by the two first layers of the surface. For instance the negative peak at $\sim 3$ eV in the clean surface comes from the first atomic layer, whereas the positive peak at $\sim 3.4$ eV comes from the second atomic layer. For the Sb covered surface the signal seem to be dominated by the Sb zigzag chains that correspond to $\ell=1$ in Fig. 3.4, with some contribution by the Ga and As atoms in the second layer but only for energies above $\sim 2.5$ eV. We find that for both surfaces a large $N_c$ is required for convergence, as seen in Table 3.1, and that $\ell_{\text{eff}}=7$ with is corresponding value of $L_{\text{eff}}$ properly included in Eq. (3.17).

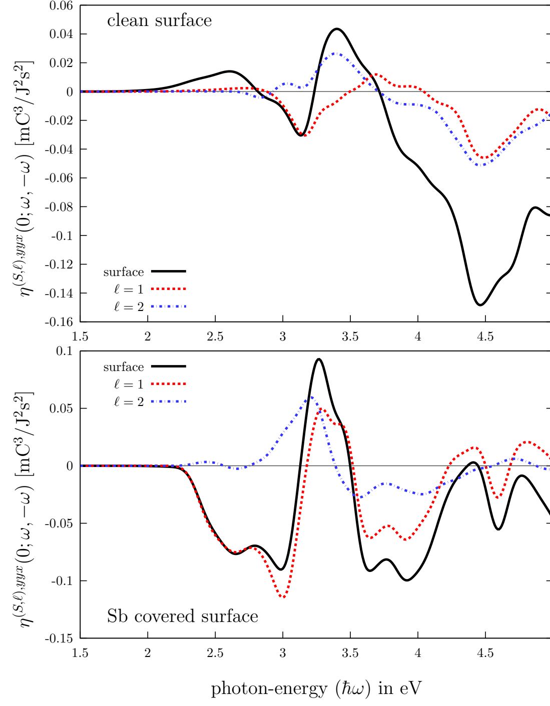


Figure 3.4: Spectra of $\eta_2^{S,yyx}(0;\omega,-\omega)$ and $\tilde{\eta}_2^{\ell,yyx}(0;\omega,-\omega)$ for the clean and an Sb covered GaAs(110)(1 × 1) surfaces. The spectra for $\ell = 1$ in the clean (Sb-covered) surface corresponds to that layer with the zigzag chains of Ga and As (Sb) atoms, and the spectra for $\ell = 2$ corresponds to the second layer of Ga and As atoms for both surfaces.

### 3.5.3 Surface vs. bulk experimental detection estimate

The detection of injection current requires measurements of voltage induced along the surface [LSSvD99], or terahertz radiation generated by an incident ultrafast optical pulse [CLvD02, CFD+99]. To demonstrate that this effect is strong enough to be observed experimentally we refer to the study of injection of current in hexagonal bulk CdSe made by Laman et al. [LSSvD99]. There the current injection generation was restricted to the penetration depth of $l \approx 1.8$ $\mu$m of the incident radiation, therefore the signal can be associated with an effective surface injection coefficient $\eta_2^S = l\eta_2^B$, where $\eta_2^B$ is the bulk coefficient. The injection current that results with a carrier momentum relaxation time of $\tau \approx 40$ fs, is $J_{inj} \propto 4\tau\eta_2^B|E_0|^2$ (see Eq. (3.18)) where an effective surface

| Surface | Number of Layers $N_c$ | $\mathcal{S}$ (eV) |
|---|---|---|
| Si(111)(2 × 1) | 16 | 0.43 |
| GaAs(110)(1 × 1) | 27 | 1 |
| GaAs(110)(1 × 1):Sb | (1)Sb+(27)GaAs+(1)Sb=29 | 0.8 |

Table 3.1: We give the number of atomic layers and the scissors correction $\mathcal{S}$ for the considered slab. In all surfaces, the we used a grid of 112 **k**-points and 10 Ha as the cut-off energy.

current $J^S_{inj} = lJ_{inj}$ of magnitude 5.4 nA/cm was detected [LSSvD99], corresponding to an effective surface injection coefficient $\eta^S_2 = 90$ mC$^3$/(J$^2$s$^2$). This experimental value is larger than our calculated values. However, the measurements of injection current made by Latman et al. [LSSvD99] were done at low incident field intensity of only 0.06 W/cm$^2$. Since the current signal generated from the effect scales linearly with the incident intensity (see Eq. (3.19)), an easily observable signal from surface injection current should be possible at intensities low enough to avoid surface damage. Finally, the injection current periodic dependence on the phase shift between two perpendicular light polarizations provides a straightforward way to discriminate the injection current from various surface photovoltaic effects.

## 3.6 Conclusions

We have developed a layer-by-layer formalism of the injection current in order to calculate it at the surface of semiconductor crystals. Since the injection current is zero for crystals with bulk inversion symmetry or crystal of the groups $\bar{6}m2$, $\bar{6}$, and $\bar{4}\bar{3}m$ (zinc blende), the experimental measurement of such a current present a valuable tool for non-invasive characterization of semiconductor surfaces. Following the layer-by-layer approach we derived the macroscopic response tensor that describes the surface injection current. We performed *ab-initio* calculations to evaluate the response for a few prototypical surfaces such as the clean Si(111)(2×1) as well as clean and Sb terminated GaAs(110)(1×1) surfaces. The surface injection current is found to be very sensitive to the basic semiconductor surface parameters such as reconstruction, unit cell symmetry, adsorbates type and bonding, which modify the electronic band structure. At all considered surfaces, contributions to the surface states are clearly present in the calculated spectra of the surface injection coefficients. The layer-by-layer

analysis proved to be crucial in order to extract the current response of each atomic layer of any given system, and thus it allows to explain the surface response behavior as the sum of the response contributions of the different atomic planes.

Like other conventional optical techniques, it requires a comparably easy experimental setup. However, unlike SSHG, which is a parametric process and typically only probes excitation to virtual states, the surface injection current involves real transitions where the system is left in the final excited state. Since, the nature of these final excited states can be understood in terms of the symmetry and the structure of the surface, it is possible to interpret the injection current much more directly than the signal due to SSHG. Also, the injection current is linear in the incident optical intensity, unlike the quadratic dependence of SSH. Although detection by terahertz radiation requires ultra short pulses, we note that electrode detection of the injection current has been demostrated even with CW radiation [CFD+99].

Finally, numerical estimates indicate that the surface injection current should be measurable. Thus, the injection current offers the possibility of using optical coherent control to manipulate the actual motion of the electrons at the surface. Experiments to investigate the surface injection current are clearly warranted.

## 3.7 Appendix

We derive Eq. (3.4) that is needed for the Eq. (3.4) of polarization of the $\ell^{th}$ layer. We combine Eq. (14) and Eq. (15) from Mendoza et al. [MNAS06], to write

$$J^{\ell,a}(\omega) = e\int \frac{d^3k}{8\pi^3}\sum_{mn} c_{mn}(\mathbf{k},\omega)\mathcal{V}^{\ell,a}_{nm}(\mathbf{k}), \tag{3.20}$$

as the current density from the $\ell^{th}$ layer of the slab used to represent the semi-infinite crystal [MNAS06]. In the equation above, $c_{mn}$ is given by

$$c_{mn}(\mathbf{k},\omega) = \frac{-ie}{\hbar}\frac{f_{nm}v^b_{mn}(\mathbf{k})E^b(\omega)}{\omega_{mn}(\mathbf{k})(\omega_{mn}(\mathbf{k})-\omega-i\eta)}, \tag{3.21}$$

From $\mathbf{J} = d\mathbf{P}/dt$, and assuming a harmonic field $\mathbf{E}(t) = \mathbf{E}(\omega)e^{-i\omega t} + \mathbf{E}^*(\omega)e^{i\omega t}$, using Eq. (3.20) and Eq. (3.21) gives

$$\begin{aligned} P^{\ell,a}(\omega) &= \frac{e^2}{\hbar\omega}\int\frac{d^3k}{8\pi^3}\sum_{mn}\frac{f_{nm}\mathcal{V}^{\ell,a}_{nm}(\mathbf{k})v^b_{mn}(\mathbf{k})}{\omega_{mn}(\mathbf{k})(\omega_{mn}(\mathbf{k})-\omega-i\eta)}E^b(\omega) \quad (3.22) \\ &= \frac{e^2}{\hbar}\int\frac{d^3k}{8\pi^3}\sum_{mn}\frac{f_{nm}\mathcal{V}^{\ell,a}_{nm}(\mathbf{k})v^b_{mn}(\mathbf{k})}{\omega_{mn}(\mathbf{k})(\omega_{mn}(\mathbf{k})-i\eta)}\Big(\frac{1}{\omega}+\frac{1}{\omega_{mn}(\mathbf{k})-\omega-i\eta}\Big)E^b(\omega) \\ &= \frac{e^2}{\hbar}\int\frac{d^3k}{8\pi^3}\sum_{mn}\frac{f_{nm}\mathcal{V}^{\ell,a}_{nm}(\mathbf{k})v^b_{mn}(\mathbf{k})}{\omega^2_{mn}(\mathbf{k})}\Big(\frac{1}{\omega}+\frac{1}{\omega_{mn}(\mathbf{k})-\omega-i\eta}\Big)E^b(\omega), \end{aligned}$$

since we can take $\eta \to 0$ in the first term after the sum. Only the "positive frequency" term is kept in the result above, because that term will contribute to the positive frequency part of the injection current responses. Using time-reversal symmetry, i.e. $v^a_{nm}(-\mathbf{k}) = -v^a_{mn}(\mathbf{k})$, $\mathcal{V}^{\ell,a}_{nm}(-\mathbf{k}) = -\mathcal{V}^{\ell,a}_{mn}(\mathbf{k})$, and $\omega_{mn}(\mathbf{k}) = \omega_{mn}(-\mathbf{k})$, we can easily show that the $1/\omega$ term vanishes as one does the sum over $\mathbf{k}$. Since $f_{nm} = f_n - f_m$ forces $n \neq m$, we can use $v^a_{nm}(\mathbf{k}) = i\omega_{nm}(\mathbf{k})r^a_{nm}(\mathbf{k})$ and $\mathcal{V}^a_{nm}(\mathbf{k}) = i\omega_{nm}(\mathbf{k})\mathcal{R}^a_{nm}(\mathbf{k})$ in Eq. (3.22) to write

$$\begin{aligned} P^{\ell,a}(\omega) &= \frac{e^2}{\hbar}\int\frac{d^3k}{8\pi^3}\sum_{m\neq n} f_{nm}\frac{\mathcal{R}^{\ell,a}_{nm}(\mathbf{k})r^b_{mn}(\mathbf{k})}{\omega_{mn}(\mathbf{k})-\omega-i\eta}E^b(\omega) \\ &\equiv \hbar\xi^{\ell,ab}(\omega)E^b(\omega), \quad (3.23) \end{aligned}$$

as the corresponding polarization of the system's layer, $\ell^{th}$, from where Eq. (3.4) could be obtained.

To obtain Eq. (3.16) we proceed as follow. We write the first term of

Eq. (3.14) as

$$
\begin{aligned}
\eta^{\ell,abc} &\propto \frac{i|e|^3}{2\hbar^2}\sum_{m\neq n} f_{nm}\Big(\int_{\mathbf{k}>0}\frac{\Delta^{\ell,a}_{mn}(\mathbf{k})\mathcal{R}^{\ell,c}_{nm}(\mathbf{k})r^b_{mn}(\mathbf{k})}{\omega_{mn}(\mathbf{k})-\omega-i\eta} \\
&+ \int_{\mathbf{k}<0}\frac{\Delta^{\ell,a}_{mn}(\mathbf{k})\mathcal{R}^{\ell,c}_{nm}(\mathbf{k})r^b_{mn}(\mathbf{k})}{\omega_{mn}(\mathbf{k})-\omega-i\eta}\Big)\frac{d^3k}{8\pi^3} \\
&= \frac{i|e|^3}{2\hbar^2}\sum_{m\neq n} f_{nm}\int_{\mathbf{k}>0}\frac{d^3k}{8\pi^3}\Delta^{\ell,a}_{mn}(\mathbf{k})\frac{\mathcal{R}^{\ell,c}_{nm}(\mathbf{k})r^b_{mn}(\mathbf{k})-\mathcal{R}^{\ell,c}_{mn}(\mathbf{k})r^b_{nm}(\mathbf{k})}{\omega_{mn}(\mathbf{k})-\omega-i\eta} \\
&= \frac{i|e|^3}{2\hbar^2}\sum_{m\neq n} f_{nm}\int_{\mathbf{k}>0}\frac{d^3k}{8\pi^3}\Delta^{\ell,a}_{mn}(\mathbf{k})\frac{\mathcal{R}^{\ell,c}_{nm}(\mathbf{k})r^b_{mn}(\mathbf{k})-\mathcal{R}^{\ell,c^*}_{nm}(\mathbf{k})r^{b^*}_{mn}(\mathbf{k})}{\omega_{mn}(\mathbf{k})-\omega-i\eta} \\
&= \frac{-|e|^3}{2\hbar^2}\sum_{m\neq n} f_{nm}\int_{\mathbf{k}>0}\frac{d^3k}{8\pi^3}\Delta^{\ell,a}_{mn}(\mathbf{k})\frac{2\mathrm{Im}[\mathcal{R}^{\ell,c}_{nm}(\mathbf{k})r^b_{mn}(\mathbf{k})]}{\omega_{mn}(\mathbf{k})-\omega-i\eta} \\
&= \frac{-|e|^3}{2\hbar^2}\int\frac{d^3k}{8\pi^3}\sum_{m\neq n} f_{nm}\Delta^{\ell,a}_{mn}(\mathbf{k})\frac{\mathrm{Im}[\mathcal{R}^{\ell,c}_{nm}(\mathbf{k})r^b_{mn}(\mathbf{k})]}{\omega_{mn}(\mathbf{k})-\omega-i\eta},
\end{aligned}
\tag{3.24}
$$

where we recall that $\Delta^{\ell,a}_{nm}(\mathbf{k})$ is a real quantity, and that due to time-reversal invariance $r^a_{nm}(-\mathbf{k}) = r^a_{mn}(\mathbf{k})$ and $\mathcal{R}^{\ell,a}_{nm}(-\mathbf{k}) = \mathcal{R}^{\ell,a}_{mn}(\mathbf{k})$ is satisfied. Likewise, the second term of Eq. (3.14) could be deduced, so we obtain

$$
\begin{aligned}
\eta^{\ell,abc}(0;\omega,-\omega) &= \frac{-|e|^3}{2\hbar^2}\int\frac{d^3k}{8\pi^3}\sum_{m\neq n} f_{nm}\Delta^{\ell,a}_{mn}(\mathbf{k})\Big(\frac{\mathrm{Im}[\mathcal{R}^{\ell,c}_{nm}(\mathbf{k})r^b_{mn}(\mathbf{k})]}{\omega_{mn}(\mathbf{k})-\omega-i\eta} \\
&- \frac{\mathrm{Im}[\mathcal{R}^{\ell,b}_{mn}(\mathbf{k})r^c_{nm}(\mathbf{k})]}{\omega_{mn}(\mathbf{k})-\omega+i\eta}\Big).
\end{aligned}
\tag{3.25}
$$

Now, we prove several properties of $\eta^{\ell,abc}(0;\omega,-\omega)$ from the equation above.

For instance

$$\begin{aligned}
\eta^{\ell,abc}(0;-\omega,\omega) &= \frac{-|e|^3}{2\hbar^2}\int\frac{d^3k}{8\pi^3}\sum_{m\neq n} f_{nm}\Delta^{\ell,a}_{mn}(\mathbf{k})\Big(\frac{\mathrm{Im}[\mathcal{R}^{\ell,c}_{nm}(\mathbf{k})r^b_{mn}(\mathbf{k})]}{\omega_{mn}(\mathbf{k})+\omega-i\eta} \\
&- \frac{\mathrm{Im}[\mathcal{R}^{\ell,b}_{mn}(\mathbf{k})r^c_{nm}(\mathbf{k})]}{\omega_{mn}(\mathbf{k})+\omega+i\eta}\Big) \\
&= \frac{-|e|^3}{2\hbar^2}\int\frac{d^3k}{8\pi^3}\sum_{m\neq n} f_{nm}\Delta^{\ell,a}_{mn}(\mathbf{k})\Big(\frac{\mathrm{Im}[\mathcal{R}^{\ell,c}_{nm}(\mathbf{k})r^b_{mn}(\mathbf{k})]}{-\omega_{nm}(\mathbf{k})+\omega-i\eta} \\
&- \frac{\mathrm{Im}[\mathcal{R}^{\ell,b}_{mn}(\mathbf{k})r^c_{nm}(\mathbf{k})]}{-\omega_{nm}(\mathbf{k})+\omega+i\eta}\Big) \\
&= \frac{-|e|^3}{2\hbar^2}\int\frac{d^3k}{8\pi^3}\sum_{m\neq n} f_{nm}\Delta^{\ell,a}_{mn}(\mathbf{k})\Big(\frac{-\mathrm{Im}[\mathcal{R}^{\ell,c}_{nm}(\mathbf{k})r^b_{mn}(\mathbf{k})]}{\omega_{nm}(\mathbf{k})-\omega+i\eta} \\
&+ \frac{\mathrm{Im}[\mathcal{R}^{\ell,b}_{mn}(\mathbf{k})r^c_{nm}(\mathbf{k})]}{\omega_{nm}(\mathbf{k})-\omega-i\eta}\Big) \\
&= \frac{-|e|^3}{2\hbar^2}\int\frac{d^3k}{8\pi^3}\sum_{m\neq n} f_{mn}\Delta^{\ell,a}_{nm}(\mathbf{k})\Big(\frac{-\mathrm{Im}[\mathcal{R}^{\ell,c}_{mn}(\mathbf{k})r^b_{nm}(\mathbf{k})]}{\omega_{mn}(\mathbf{k})-\omega+i\eta} \\
&+ \frac{\mathrm{Im}[\mathcal{R}^{\ell,b}_{nm}(\mathbf{k})r^c_{mn}(\mathbf{k})]}{\omega_{mn}(\mathbf{k})-\omega-i\eta}\Big) \\
&= \frac{-|e|^3}{2\hbar^2}\int\frac{d^3k}{8\pi^3}\sum_{m\neq n} f_{nm}\Delta^{\ell,a}_{mn}(\mathbf{k})\Big(\frac{\mathrm{Im}[\mathcal{R}^{\ell,c}_{nm}(\mathbf{k})r^b_{mn}(\mathbf{k})]}{\omega_{mn}(\mathbf{k})-\omega+i\eta} \\
&- \frac{\mathrm{Im}[\mathcal{R}^{\ell,b}_{mn}(\mathbf{k})r^c_{nm}(\mathbf{k})]}{\omega_{mn}(\mathbf{k})-\omega-i\eta}\Big) \\
&= \eta^{\ell,abc^*}(0;\omega,-\omega), \qquad (3.26)
\end{aligned}$$

Where the second step we simply did $\omega_{mn}(\mathbf{k}) = -\omega_{nm}(\mathbf{k})$; in the third step we factorize a minus sign in the energy denominators; in fourth step we exchanged the dummy indices $m$ and $n$; fifth line we used the following identities $\mathrm{Im}[A_{mn}B_{nm}] = -\mathrm{Im}[A_{nm}B_{mn}]$ and $f_{mn}\Delta^{\ell,a}(\mathbf{k})_{nm} = f_{nm}\Delta^{\ell,a}(\mathbf{k})_{mn}$; finally in

the last step we just followed trivially from the fifth step Also,

$$
\begin{aligned}
\eta^{\ell,acb}(0;\omega,-\omega) &= \frac{-|e|^3}{2\hbar^2}\int\frac{d^3k}{8\pi^3}\sum_{m\neq n} f_{nm}\Delta^{\ell,a}_{mn}(\mathbf{k})\Big(\frac{\mathrm{Im}[\mathcal{R}^{\ell,b}_{nm}(\mathbf{k})r^c_{mn}(\mathbf{k})]}{\omega_{mn}(\mathbf{k})-\omega-i\eta} \\
&- \frac{\mathrm{Im}[\mathcal{R}^{\ell,c}_{mn}(\mathbf{k})r^b_{nm}(\mathbf{k})]}{\omega_{mn}(\mathbf{k})-\omega+i\eta}\Big) \\
&= \frac{-|e|^3}{2\hbar^2}\int\frac{d^3k}{8\pi^3}\sum_{m\neq n} f_{nm}\Delta^{\ell,a}_{mn}(\mathbf{k})\Big(\frac{-\mathrm{Im}[\mathcal{R}^{\ell,b}_{mn}(\mathbf{k})r^c_{nm}(\mathbf{k})]}{\omega_{mn}(\mathbf{k})-\omega-i\eta} \\
&+ \frac{\mathrm{Im}[\mathcal{R}^{\ell,c}_{nm}(\mathbf{k})r^b_{mn}(\mathbf{k})]}{\omega_{mn}(\mathbf{k})-\omega+i\eta}\Big) \\
&= \frac{|e|^3}{2\hbar^2}\int\frac{d^3k}{8\pi^3}\sum_{m\neq n} f_{nm}\Delta^{\ell,a}_{mn}(\mathbf{k})\Big(\frac{\mathrm{Im}[\mathcal{R}^{\ell,b}_{mn}(\mathbf{k})r^c_{nm}(\mathbf{k})]}{\omega_{mn}(\mathbf{k})-\omega-i\eta} \\
&- \frac{\mathrm{Im}[\mathcal{R}^{\ell,c}_{nm}(\mathbf{k})r^b_{mn}(\mathbf{k})]}{\omega_{mn}(\mathbf{k})-\omega+i\eta}\Big) \\
&= -\eta^{\ell,abc}(0;\omega,-\omega),
\end{aligned}
\tag{3.27}
$$

where in the second step we use the identity $\mathrm{Im}[A_{mn}B_{nm}] = -\mathrm{Im}[A_{nm}B_{mn}]$ and in the third step we simply factorized a minus sign. The last line of Eq. (3.27) follows by comparing the obtained expression of third step with Eq. (3.14). Similarly we can prove that $\eta^{\ell,abc}(0;-\omega,\omega) = -\eta^{\ell,abc}(0;\omega,-\omega)$.

Using $\lim_{\eta\to 0} 1/(x-i\eta) = \mathcal{P}(1/x) + i\pi\delta(x)$, with $\mathcal{P}$ the principal part, we get from Eq. (3.25) that

$$
\begin{aligned}
\eta^{\ell,abc}_{\mathrm{i}}(0;\omega,-\omega) &= \frac{-\pi|e|^3}{2\hbar^2}\int\frac{d^3k}{8\pi^3}\sum_{m\neq n} f_{nm}\Delta^{\ell,a}_{mn}(\mathbf{k})\Big(\mathrm{Im}[\mathcal{R}^{\ell,c}_{nm}(\mathbf{k})r^b_{mn}(\mathbf{k})] \\
&+ \mathrm{Im}[\mathcal{R}^{\ell,b}_{mn}(\mathbf{k})r^c_{nm}(\mathbf{k})]\Big)\delta(\omega_{mn}(\mathbf{k})-\omega) \\
&= \frac{\pi|e|^3}{2\hbar^2}\int\frac{d^3k}{8\pi^3}\sum_{m\neq n} f_{nm}\Delta^{\ell,a}_{mn}(\mathbf{k})\Big(\mathrm{Im}[\mathcal{R}^{\ell,c}_{mn}(\mathbf{k})r^b_{nm}(\mathbf{k})] \\
&+ \mathrm{Im}[\mathcal{R}^{\ell,b}_{nm}(\mathbf{k})r^c_{mn}(\mathbf{k})]\Big)\delta(\omega_{mn}(\mathbf{k})-\omega),
\end{aligned}
\tag{3.28}
$$

which gives $\eta^{\ell,abc}_2(0;\omega,-\omega) = i\eta^{\ell,abc}_{\mathrm{i}}(0;\omega,-\omega)$ from Eq. (3.16). If we replace

$\mathcal{R}^{\ell,a}_{nm}(\mathbf{k})$ by $r^a_{nm}(\mathbf{k})$ and $\Delta^{\ell,a}_{mn}(\mathbf{k})$ by $\Delta^a_{mn}(\mathbf{k})$ in the previous equation we get

$$\begin{aligned}\eta_2^{abc}(0;\omega,-\omega) &= \frac{i\pi|e|^3}{\hbar^2}\int\frac{d^3k}{8\pi^3}\sum_{m\neq n} f_{nm}\Delta^a_{mn}(\mathbf{k})\mathrm{Im}[r^c_{mn}(\mathbf{k})r^b_{mn}(\mathbf{k})]\\ &\times \delta(\omega_{mn}(\mathbf{k})-\omega)\\ &= \frac{\pi|e|^3}{2\hbar^2}\int\frac{d^3k}{8\pi^3}\sum_{m\neq n} f_{nm}\Delta^a_{mn}(\mathbf{k})[r^c_{mn}(\mathbf{k}),r^b_{nm}(\mathbf{k})]\\ &\times \delta(\omega_{mn}(\mathbf{k})-\omega),\end{aligned} \tag{3.29}$$

where we removed the $\ell$ superscript since the expression no longer depends on its value, and used $2i\mathrm{Im}[A_{nm}B_{mn}] = A_{nm}B_{mn} - B_{nm}A_{mn} \equiv [A_{nm}, B_{mn}]$. The above expression is the same as that one derived by Sipe and Shkrebtii valid for a bulk semiconductor [SS00].

Chapter 4

# Optical spin injection at semiconductor surfaces

## Contents


**4.1 Summary** . . . . . . . . . . . . . . . . . . . . . . . . . . . . **55**

**4.2 Introduction** . . . . . . . . . . . . . . . . . . . . . . . . . . **56**

**4.3 Theory** . . . . . . . . . . . . . . . . . . . . . . . . . . . . . **57**

4.3.1 Surface responses . . . . . . . . . . . . . . . . . . . . . . . 61

**4.4 Computational details** . . . . . . . . . . . . . . . . . . . . . **63**

**4.5 Results** . . . . . . . . . . . . . . . . . . . . . . . . . . . . . **65**

**4.6 Conclusions** . . . . . . . . . . . . . . . . . . . . . . . . . . . **73**


## 4.1 Summary


We present a study of electron spin-injection at several Si(111) surfaces produced by optical excitation above the direct gap with circularly polarized light. Calculations where performed on H, As and In covered Si(111) surfaces. The reconstruction of each of these surfaces is well understood and experimentally achievable. We use a full-band electronic structure pseudopotential scheme to calculate the rate of spin and carrier injection, and then calculate the degree of spin polarization up to energies well above the surface modified band gap. The model accounts for the coherences excited in a semiconductor with spin-split bands, and a "layer-by-layer" analysis of the response is implemented. The relatively low symmetry of the surfaces leads to spin-injection from direct transitions which can be up to 52% for the In covered Si(111) surface. For comparison, in bulk Si the maximum polarization calculated is 30%, and only over a very narrow range of incident frequencies. The spectra for all of the

surfaces shows an interesting behavior as a function of the energy of incidence of the circularly polarized light.

## 4.2 Introduction

The study of spin injection into a non-magnetic semiconductor is an important problem in condensed matter physics. The optical excitation of semiconductors with circularly polarized light creates spin-polarized electrons in the conduction bands [DP84]. The idea of using light for spin injection and detection dates back to the late 1960 [Lam68], and later it was shown that conversion of angular momentum of light into electron spin and vice versa is very efficient in III-V semiconductors [DP84]. Known as "optical orientation", this effect serves as an important tool in the field of spintronics, where it is used to spin polarize electrons. The injection of spin and the degree of spin polarization in bulk GaAs, Si and CdSe semiconductors has been reported recently [NRSM+07], and a detailed comparison between a 30-band $\mathbf{k}\cdot\mathbf{p}$ model and a full band structure LDA (Local Density Approximation) calculation was given. Some of the results obtained could be explained by using well-known features of the band structure and selection rules around the $\Gamma$ points of GaAs and Si. However, for photon energies well above the band gap the selection rules are more complicated and full band structure calculations are required to calculate the degree of spin polarization. For many semiconductors no $\mathbf{k}\cdot\mathbf{p}$ models are available. Results of Nastos et al. [NRSM+07] indicate that the degree of spin polarization can be reliably calculated with LDA band structures. This suggests a program of study of optical orientation based on LDA calculations. Both the ubiquitous presence of a surface in any semiconductor sample, and the steady progress in the miniaturization of electronic semiconductor components, suggests a focus on the spin injected at the surface of semiconductors. In this chapter we report the first calculations of the degree of spin polarization at semiconductors surfaces produced by absorption of light across the direct gap. The Si semiconductor was chosen for this study because it is, by far, the most used semiconductor. H, As and In terminated as well as clean surfaces were studied. The criteria for choosing these surfaces as representative examples is that their atomic reconstruction is well understood and that the surfaces are experimentally achievable. To model these surfaces we use a slab approach and develop a scheme that allows us to study the layer-by-layer [HDSO03, CMS+03, MNAS06, CMN+] contribution. To calculate the rate of spin injection, we use Density Functional Theory (DFT). We restrict

ourselves to pseudopotential band structures based on the LDA + scissors correction, since this is the simplest and still the most popular approach LDA systematically underestimates the band gap, therefore a band gap correction, is required. This rigidly shifts the conduction band energies by a constant amount. The excitation of spin-split bands by the finite energy width of the laser pulse creates coherences that are properly accounted for in our description of the optical spin injection of a semi-infinite semiconductor.

We show that the lower symmetry of the reconstructed surfaces taken as examples exhibits a well differentiated spectra for the degree of spin polarization. For instance, in the In covered Si(111) surface, the spin polarization is increased to 52% from the bulk Si value of 30%, and a significant value for the spin polarization occurs over a wider frequency range. This indicates that surfaces of semiconductors provide venues for the optical injection of spin that are interesting as well as novel.

This chapter is organized as follows: in Section 4.3 we present a derivation of the spin and carrier injection rate for any layer of a slab, and their surface related counterparts. In Section 4.4 the computational details of the calculation are given. In Section 4.5 The results obtained for the degree of spin polarization of the chosen surfaces are presented and discussed, and finally in Section 4.6 conclusions are given.

## 4.3 Theory

In this section the required expressions to evaluate the degree of spin polarization for a clean, cold-semiconducting surface are derived. To model the semi-infinite medium we use a slab consisting of $N$ atomic layers inside a supercell of total height $L$ and volume $\Omega = AL$, where $A$ is the surface area of the unit cell. The supercell includes the required vacuum region to use a repeated slab scheme.

In a slab calculation, not only one often wants to calculate the response from one of the two halves of the slab but also from a particular layer of the slab. A convenient way to accomplish the separation of the response of any layer is to through the use of the so called "cut function", $\mathcal{F}_\ell(z)$, as a top-hat cut function that selects a given layer,

$$\mathcal{F}_\ell(z) = \Theta(z - z_\ell + \Delta_\ell^b)\Theta(z_\ell - z + \Delta_\ell^f), \tag{4.1}$$

where $\Theta$ is the Heaviside function. Here, $\Delta_\ell^{f/b}$ is the distance that the $\ell$-th layer extends towards the front ($f$) or back ($b$) from its $z_\ell$ position. Thus $\Delta_\ell^f + \Delta_\ell^b$

is the thickness of layer $\ell$. The cut function was originally used by Hogan *et al.* [HDSO03] and Castillo *et al.* [CMS+03], and more recently was put on a more solid basis through a microscopic calculation of the linear optical response of a surface by Mendoza *et al,* [MNAS06] and in the optical coherent control of the injection current at a surface by Cabellos et al. [CMN+]. In order to obtain the spin injection rate for a particular layer of the slab, we proceed as follows. First we realized that conduction bands in a semiconductor are spin-split by a small amount [Dre55, CvSK06], typically smaller than the energy width of the laser pulse, and so the external pulse excites a coherent superposition of the two conduction spin-split states. Even for very long pulses with narrow energy widths, dephasing effects lead to an energy width of the bands large enough so that spin-split states can become quasidegenerate. Within the independent particle approximation, these coherences can be calculated by using a multiple scale approach to solve the following equation of motion for the scaled single particle density matrix $\rho_{mn}(\mathbf{k};t)$ [Boo57],

$$\frac{\partial \rho_{mn}(\mathbf{k};t)}{\partial t} = -i(\omega_{mn}(\mathbf{k}) - i\varepsilon) - \frac{i}{\hbar}([H^{\mathrm{ext}}(t), \rho(\mathbf{k};t)])_{mn}.$$

Assuming that the conduction bands $c$ and $c'$ are close to one another, and that the pulse is short enough so that the energy width overlaps the two bands, the result for the off-diagonal component, $\rho_{cc'}$, where $c$ and $c'$ are quasi-degenerate conduction states, is given by Nastos *et al.* [NRSM+07] as

$$\begin{aligned} \frac{\partial \rho_{cc'}}{\partial t} &= -i(\omega_{cc'} - i\varepsilon)\rho_{cc'} - \frac{e^2 E^{\mathrm{b}*}(\omega) E^{\mathrm{c}}(\omega)}{i\hbar^2} \\ &\quad \times \sum_v r^{\mathrm{b}}_{vc'} r^{\mathrm{c}}_{cv} \left( \frac{1}{\omega - \omega_{c'v} - i\varepsilon} - \frac{1}{\omega - \omega_{cv} + i\varepsilon} \right), \end{aligned} \tag{4.2}$$

where we have assumed a perturbation of the form $H^{\mathrm{ext}}(t) = -er^{\mathrm{a}}E^{\mathrm{a}}(t)$, with $e$ the electron charge, $\mathbf{r}$ the position operator and $\mathbf{E}(t) = \mathbf{E}(\omega)\exp(-i\omega t) + \mathbf{E}^*(\omega)\exp(i\omega t)$, being the Maxwell field. Many-particle effects and phonon scattering are neglected. In the equation above, $r^{\mathrm{a}}_{cv}(\mathbf{k}) = v^{\mathrm{a}}_{cv}(\mathbf{k})/i\omega_{cv}(\mathbf{k})$ are the off-diagonal position matrix elements, $v^{\mathrm{a}}_{cv}(\mathbf{k})$ are the matrix elements of the velocities, $\varepsilon \to 0$, and the sum over $v$ is limited to valence bands. Also, the ground state Hamiltonian, $H_0$, gives $H_0|n\mathbf{k}\rangle = \hbar\omega_n(\mathbf{k})|n\mathbf{k}\rangle$ where $\hbar\omega_n(\mathbf{k})$ is the energy of the electronic band $n$, with crystal momentum $\mathbf{k}$, $|n\mathbf{k}\rangle$ is the Bloch state, and $\omega_{mn}(\mathbf{k}) = \omega_m(\mathbf{k}) - \omega_n(\mathbf{k})$. We consider the bands to be either totally empty (conduction bands $n = c$), or totally full (valence bands $n = v$). The superscript in Roman characters indicate Cartesian coordinates,

when repeated, as in the above expressions, are to be summed over. The implicit dependence of $\mathbf{k}$ is assumed in the corresponding quantities in order to save space. Throughout this chapter we assume, that the hole spins relax very quickly and we neglect them [DP84], focusing only on the electron spins. Measurements have led to estimates of 110 fs for the heavy-hole spin life time in GaAs [HT02].

Furthemore, we change to the so called *interaction* representation, by which any operator $\mathcal{O}$ is replaced by

$$\tilde{\mathcal{O}} = e^{iH_0t/\hbar}\mathcal{O}e^{-iH_0t/\hbar},$$

such that the matrix elements are now given by,

$$\tilde{\mathcal{O}}_{mn}(\mathbf{k}) = \langle m\mathbf{k}|e^{iH_0t/\hbar}\mathcal{O}e^{-iH_0t/\hbar}|n\mathbf{k}\rangle = e^{i\omega_{mn}(\mathbf{k})t}\mathcal{O}_{mn}(\mathbf{k}). \tag{4.3}$$

Taking $\varepsilon \to 0$ in the first term of Eq. (4.2) and using Eq. (4.3) we get

$$\begin{aligned}\frac{\partial\tilde{\rho}_{cc'}(\mathbf{k})}{\partial t} &= \frac{e^2E^{\mathrm{b}}(-\omega)E^{\mathrm{c}}(\omega)}{i\hbar^2}e^{i\omega_{cc'}t} \\ &\times \sum_v r^{\mathrm{b}}_{vc'}r^{\mathrm{c}}_{cv}\left(\frac{1}{\omega-\omega_{c'v}-i\varepsilon}-\frac{1}{\omega-\omega_{cv}+i\varepsilon}\right),\end{aligned} \tag{4.4}$$

where $\varepsilon \to 0$ still needs to be taken, and we have used $\mathbf{E}^*(\omega) = \mathbf{E}(-\omega)$. Now, we introduce the top-hat cut function, $\mathcal{F}_\ell(z)$, of Eq. (3.2) in order to obtain the $\ell$-*th* layer contribution to the density matrix $\tilde{\rho}_{cc'}$ as

$$\begin{aligned}\frac{\partial}{\partial t}\langle c\mathbf{k}|\mathcal{F}_\ell(z)\tilde{\rho}|c'\mathbf{k}\rangle &= \frac{e^2E^{\mathrm{b}}(-\omega)E^{\mathrm{c}}(\omega)}{i\hbar^2}e^{i\omega_{cc'}t}\sum_v\langle v\mathbf{k}|\mathcal{F}_\ell(z)r^{\mathrm{b}}|c'\mathbf{k}\rangle\langle c\mathbf{k}|r^{\mathrm{c}}|v\mathbf{k}\rangle \\ &\times \left(\frac{1}{\omega-\omega_{c'v}-i\varepsilon}-\frac{1}{\omega-\omega_{cv}+i\varepsilon}\right),\end{aligned}$$

and define $\tilde{\rho}^{\ell}_{cc'}(\mathbf{k}) \equiv \langle c\mathbf{k}|\mathcal{F}_\ell(z)\tilde{\rho}|c'\mathbf{k}\rangle$ and $\mathcal{R}^{\ell,\mathrm{b}}_{nm}(\mathbf{k}) \equiv \langle n\mathbf{k}|\mathcal{F}_\ell(z)r^{\mathrm{b}}|m\mathbf{k}\rangle$ (with $n \neq m$), to get

$$\begin{aligned}\frac{\partial\tilde{\rho}^{\ell}_{cc'}}{\partial t} &= \frac{e^2}{i\hbar^2}e^{i\omega_{cc'}t}\sum_v\mathcal{R}^{\ell,\mathrm{b}}_{vc'}r^{\mathrm{c}}_{cv}\left(\frac{1}{\omega-\omega_{c'v}-i\varepsilon}-\frac{1}{\omega-\omega_{cv}+i\varepsilon}\right) \\ &\times E^{\mathrm{b}}(-\omega)E^{\mathrm{c}}(\omega),\end{aligned} \tag{4.5}$$

as the $cc'$ matrix elements for the single particle density of the $\ell^{th}$ layer (in the interaction picture). Following Mendoza et al. [MNAS06], the modified

position operator matrix elements are obtained through Eq. (3.5). The spin injection rate into the conduction bands of a semiconductor for the $\ell$-*th* layer, is calculated through $\dot{S}^{\ell,\mathrm{a}} = \mathrm{Tr}(\dot{\tilde{\rho}}^{\ell}\tilde{S}^{\mathrm{a}})$, with Tr the trace. From Eq. (4.5) we get

$$\begin{aligned}\dot{S}^{\ell,\mathrm{a}} &= \frac{e^2}{i\hbar^2}\int\frac{d^3k}{8\pi^3}\sum_{vcc'}{}' S^{\mathrm{a}}_{c'c}\mathcal{R}^{\ell,\mathrm{b}}_{vc'}r^{\mathrm{c}}_{cv}\left(\frac{1}{\omega-\omega_{c'v}-i\varepsilon}-\frac{1}{\omega-\omega_{cv}+i\varepsilon}\right)\\ &\times\ E^{\mathrm{b}}(-\omega)E^{\mathrm{c}}(\omega),\end{aligned} \tag{4.6}$$

where we used $\tilde{S}^{\mathrm{a}}_{c'c} = e^{i\omega_{c'c}t}S^{\mathrm{a}}_{c'c}$ (see Eq. (4.3)). The prime on the summation indicates that the sum is to be done over pairs of conduction bands $c$ and $c'$ that are quasi-degenerate. We classify bands separated by no more than $\delta E$ to be quasi degenerate, where the defining energy $\delta E$ is chosen such that it is approximately both a typical laser pulse energy width and the room temperature energy. We find that for $\delta E \sim 30$ meV the results are rather insensitive to the exact value of $\delta E$. In Eq. (4.6), $S^{\mathrm{a}}_{c'c}(\mathbf{k})$, are the matrix elements of the spin operator, $S^{\mathrm{a}} = (\hbar/2)\sigma^{\mathrm{a}}$, with $\sigma^{\mathrm{a}}$ the begin Pauli matrices

$$\sigma^{\mathrm{x}} = \begin{pmatrix} 0 & 1\\ 1 & 0\end{pmatrix}\quad \sigma^{\mathrm{y}} = \begin{pmatrix} 0 & -i\\ i & 0\end{pmatrix}\quad \sigma^{\mathrm{z}} = \begin{pmatrix} 1 & 0\\ 0 & -1\end{pmatrix}.$$

From Eq. (4.6) we see that the spin injection rate is proportional to the field intensity [MZ84, NBS03, NRSM+07], thus it is convenient to write it as,

$$\dot{S}^{\ell,\mathrm{a}} = \zeta^{\ell,\mathrm{abc}}(\omega)E^{\mathrm{b}}(-\omega)E^{\mathrm{c}}(\omega), \tag{4.7}$$

where

$$\begin{aligned}\zeta^{\ell,\mathrm{abc}}(\omega) &= \frac{e^2}{i\hbar^2}\int\frac{d^3k}{8\pi^3}\sum_{vcc'}{}' S^{\mathrm{a}}_{c'c}(\mathbf{k})\mathcal{R}^{\ell,\mathrm{b}}_{vc'}(\mathbf{k})r^{\mathrm{c}}_{cv}(\mathbf{k})\\ &\times\left(\frac{1}{\omega-\omega_{c'v}(\mathbf{k})-i\varepsilon}-\frac{1}{\omega-\omega_{cv}(\mathbf{k})+i\varepsilon}\right).\end{aligned} \tag{4.8}$$

is the tensor purely imaginary that allow us to calculate the $\ell$-*th* layer spin injection rate.

Using time-reversal invariance [notd], Eq. (4.8) can be rewritten as

$$\begin{aligned}\zeta^{\ell,\mathrm{abc}}(\omega) &= \frac{e^2}{\hbar^2}\int\frac{d^3k}{8\pi^3}\sum_{vcc'}{}' \mathrm{Im}[S^{\mathrm{a}}_{c'c}(\mathbf{k})\mathcal{R}^{\ell,\mathrm{b}}_{vc'}(\mathbf{k})r^{\mathrm{c}}_{cv}(\mathbf{k})]\\ &\times\left(\frac{1}{\omega-\omega_{c'v}(\mathbf{k})-i\varepsilon}-\frac{1}{\omega-\omega_{cv}(\mathbf{k})+i\varepsilon}\right).\end{aligned}$$

Taking $\varepsilon \to 0$, leads to

$$\begin{aligned}\zeta^{\ell,\mathrm{abc}}(\omega) &= \frac{e^2}{\hbar^2}\int\frac{d^3k}{8\pi^3}\sum_{vcc'}{}' \,\mathrm{Im}[S^{\mathrm{a}}_{c'c}(\mathbf{k})\mathcal{R}^{\ell,\mathrm{b}}_{vc'}(\mathbf{k})r^{\mathrm{c}}_{cv}(\mathbf{k})] \\ &\times \Big(\mathcal{P}\Big(\frac{\omega_{cc'}}{(\omega_{cv}(\mathbf{k})-\omega)(\omega_{c'v}(\mathbf{k})-\omega)}\Big) \\ &+ i\pi\big(\delta(\omega_{cv}(\mathbf{k})-\omega)+\delta(\omega_{c'v}(\mathbf{k})-\omega)\big)\Big),\end{aligned}$$

where $\mathcal{P}$ denotes the Cauchy principal part. Since $\omega_{cc'}$ is small we can neglect the principal part term and obtain that

$$\begin{aligned}\zeta^{\ell,\mathrm{abc}}(\omega) &= \frac{i\pi e^2}{\hbar^2}\int\frac{d^3k}{8\pi^3}\sum_{vcc'}{}' \,\mathrm{Im}[S^{\mathrm{a}}_{c'c}(\mathbf{k})\mathcal{R}^{\ell,\mathrm{b}}_{vc'}(\mathbf{k})r^{\mathrm{c}}_{cv}(\mathbf{k}) \\ &+ S^{\mathrm{a}}_{cc'}(\mathbf{k})\mathcal{R}^{\ell,\mathrm{b}}_{vc}(\mathbf{k})r^{\mathrm{c}}_{c'v}(\mathbf{k})]\delta(\omega_{cv}(\mathbf{k})-\omega),\end{aligned} \tag{4.9}$$

We finish this section presenting the carrier injection rate, $\dot{n}^\ell$, for the $\ell$-*th* layer. With the help of Eq. (4.5) we obtain that

$$\dot{n}^\ell = \xi^{\ell,\mathrm{bc}}(\omega)E^{\mathrm{b}}(-\omega)E^{\mathrm{c}}(\omega), \tag{4.10}$$

with

$$\xi^{\ell,\mathrm{ab}}(\omega) = \frac{2\pi e^2}{\hbar^2}\int\frac{d^3k}{8\pi^3}\sum_{vc}\mathrm{Re}[\mathcal{R}^{\ell,\mathrm{a}}_{vc}(\mathbf{k})r^{\mathrm{b}}_{cv}(\mathbf{k})]\delta(\omega_{cv}(\mathbf{k})-\omega), \tag{4.11}$$

begin the carrier injection tensor, this result agrees with that reported by Cabellos et al. [CMN+] For a bulk calculation we simply take $\mathcal{R}^{\ell,\mathrm{a}}_{mn}(\mathbf{k}) \to r^{\mathrm{a}}_{mn}(\mathbf{k})$ in Eq. (4.9) and Eq. (4.11) to obtain $\zeta^{B,\mathrm{abc}}(\omega)$ and $\xi^{B,\mathrm{ab}}(\omega)$, respectively. These bulk ($B$) expressions are the same as those of Nastos et al. [NRSM+07].

### 4.3.1 Surface responses

Once that we have the expressions for the carrier injection rate and spin injection rate for the $\ell$-*th* layer, we proceed to define their surface related quantities. The slab that we have useed to represent the semi-infinite system, extends $N$ atomic layers, from the “front” surface to the “back”surface. $N$ is chosen such that one gets converged results, i.e. for the considered physical quantities that beyond some value of $N \geq N_c$ its corresponding spectrum do not change significantly. In principle, for a given layer $\ell$ in the middle of the slab or close to it, called $\ell_B$, when $N \geq N_c$, the values of $\dot{n}^{\ell=\ell_B}$ and $\dot{\mathbf{S}}^{\ell=\ell_B}$ should match

the bulk values. Indeed, one should expect that for a large enough slab, the evaluation of $\xi^{\ell_B,\mathrm{bc}}$ from Eq. (4.11) and $\zeta^{\ell_B,\mathrm{abc}}$ from Eq. (4.9), should give the corresponding bulk values for $\xi^{B,\mathrm{bc}}$ and $\zeta^{B,\mathrm{abc}}$, respectively [note].

Both $\dot{n}^\ell$ and $\dot{\mathbf{S}}^\ell$, are defined per unit volume, and as such are not additive quantities. To overcome this, we simply multiply them by the normalizing unit cell volume $\Omega$, add them and then divide over $A$, to get the corresponding surface related quantities per unit area. Therefore, we can easily define a surface response through the following general expression,

$$\mathcal{O}^S = \frac{1}{A}\sum_{\ell=1}^{\ell_B}\left(\Omega\mathcal{O}^\ell - \Omega\mathcal{O}^{\ell_B}\right) \quad (N \geq N_c), \tag{4.12}$$

where $\mathcal{O}$ stands for the sought response. Of course, one can also describe the above expression as the response coming from the "front" surface of the slab, while

$$\mathcal{O}^{bS} = \frac{1}{A}\sum_{\ell=\ell_B}^{N}\left(\Omega\mathcal{O}^\ell - \Omega\mathcal{O}^{\ell_B}\right) \quad (N \geq N_c),$$

would be the response of the "back" surface of the slab. For symmetric slabs $\mathcal{O}^S$ would be trivially related to $\mathcal{O}^{bS}$. We see that the above definition, Eq. (4.12), would give converged results since even if we use a very large slab with $N >> N_c$, the sum would be finite, after some large value of $\tilde{\ell} < \ell_B$ one would be at a bulk-like layer and thus $\mathcal{O}^{\tilde{\ell}} \simeq \mathcal{O}^{\ell_B}$ and the summand would be zero from this value until $\tilde{\ell} = \ell_B$.

We introduce volume independent quantities by putting a tilde over them, then $\tilde{\mathcal{O}} = \Omega\mathcal{O}$, and thus we can write with the help of Eq. (4.12)

$$\xi^{S,\mathrm{ab}}(\omega) = \frac{1}{A}\Big(\sum_{\ell=1}^{\ell_B}\tilde{\xi}^{\ell,\mathrm{ab}}(\omega) - \ell_B\tilde{\xi}^{\ell_B,\mathrm{ab}}(\omega)\Big) \quad (N \geq N_c), \tag{4.13}$$

as the response tensor that gives the surface value of the number of injected electrons into the conduction band per unit area, and

$$\zeta^{S,\mathrm{abc}}(\omega) = \frac{1}{A}\Big(\sum_{\ell=1}^{\ell_B}\tilde{\zeta}^{\ell,\mathrm{abc}}(\omega) - \ell_B\tilde{\zeta}^{\ell_B,\mathrm{abc}}(\omega)\Big) \quad (N \geq N_c), \tag{4.14}$$

as the response tensor that gives the surface value of the spin injection rate per unit area. We have used the fact that $\tilde{\xi}^{\ell_B,\mathrm{ab}}(\omega)$ and $\tilde{\zeta}^{\ell_B,\mathrm{abc}}(\omega)$ do not depend on $\ell$. Although $\zeta^{S,\mathrm{abc}}(\omega)$ is useful for understanding the total surface spin

injection, a more physically transparent quantity useful for characterizing the spin-injection is the surface degree of spin polarization(DSP), which is defined as

$$\mathcal{D}^{S,\mathrm{a}} = \frac{\dot{S}^{S,\mathrm{a}}}{(\hbar/2)\dot{n}^S}, \tag{4.15}$$

where

$$\dot{S}^{S,\mathrm{a}} = \zeta^{S,\mathrm{abc}}(\omega)E^{\mathrm{b}}(-\omega)E^{\mathrm{c}}(\omega), \tag{4.16}$$

is the surface spin injection and

$$\dot{n}^S = \xi^{S,\mathrm{bc}}(\omega)E^{\mathrm{b}}(-\omega)E^{\mathrm{c}}(\omega). \tag{4.17}$$

is the surface carrier injection.

## 4.4 Computational details

Our calculations are done by using the ABINIT plane-wave code [XBC+02]. A self-consistent calculation was done to determine the relaxed surface structures and their Kohn-Sham potential. We used the separable Hartwigsen-Goedecker-Hutter (HGH) pseudopotentials [HGH98] within the LDA as parametrized by Goedecker et al. [GTH96]. These pseudopotentials are a common choice in *ab initio* studies investigating materials where the spin-orbit contribution cannot be neglected. In our calculations, we exclude the semi-core states, though they can be included with more computational effort. Once the Kohn-Sham potential is determined, we find the wavefunctions, and then the matrix elements are calculated for **k**-points on a specially determined tetrahedral grid. This grid is used in the integrals of Eqs. (4.9) and (4.11), that are calculated through a linear analytic tetrahedral integration method [NRSM+07]. With the parameters shown in Table 4.1, we find convergence of the results for all the quantities of interest in this work, with respect to the number of layers in the slab, the number of **k**-points, and the cut-off energy.

The ABINIT code provides the plane-wave coefficients $C^{\uparrow;\downarrow}_{n\mathbf{k}}(\mathbf{G})$ of the spinor wave function expansion

$$\psi_{n\mathbf{k}}(\mathbf{r}) = \sum_{\mathbf{G}} \begin{pmatrix} C^{\uparrow}_{n\mathbf{k}}(\mathbf{G}) \\ C^{\downarrow}_{n\mathbf{k}}(\mathbf{G}) \end{pmatrix} e^{i(\mathbf{k}+\mathbf{G})\cdot\mathbf{r}}, \tag{4.18}$$

| Surface | # $\mathbf{k}$ | # Atomic layers | # Atoms | $\Delta$ (eV) |
|---|---|---|---|---|
| Clean Si(111)$(2\times 1)$ | 109 | 14 | 28 | 0.45 |
| Si(111)$(1\times 1)$ :As | 109 | 1-As+46-Si+1-As=48 | 48 | 1.14 |
| Si(111)$(1\times 1)$ :H | 109 | 1-H+46-Si+1-H=48 | 48 | 1.55 |
| Si(111)$(\sqrt{3}\times\sqrt{3})$ :In | 91 | 1-In+12-Si+1-In=14 | 38 | 1.01 |

Table 4.1: Convergence parameters for the calculation of $\dot{S}^{S,\mathrm{a}}$ and $\dot{n}^S$ and the corresponding scissors correction $\Delta$. In all surfaces the cut-off energy is 10 Ha.

where the up(down) arrow denotes the up(down) component of the spinor. From Mendoza *et al.* [MNAS06], we find that the matrix elements of the velocity, Eq. (3.5), in function of the plane-wave coefficients $C^{\uparrow;\downarrow}_{n\mathbf{k}}(\mathbf{G})$ are given by

$$\begin{aligned}\mathcal{V}^{\mathrm{a}}_{mn}(\ell;\mathbf{k}) &= \frac{\hbar}{2}\sum_{\mathbf{G},\mathbf{G}'}\left(C^{\uparrow *}_{m\mathbf{k}}(\mathbf{G})C^{\uparrow}_{n\mathbf{k}}(\mathbf{G}') + C^{\downarrow *}_{m\mathbf{k}}(\mathbf{G})C^{\downarrow}_{n\mathbf{k}}(\mathbf{G}')\right) \\ &\times \ (2k^{\mathrm{a}} + G^{\mathrm{a}} + G'^{\mathrm{a}})\delta_{\mathbf{G}_\parallel,\mathbf{G}'_\parallel} f_\ell(G_\perp - G'_\perp). \end{aligned} \tag{4.19}$$

where the reciprocal lattice vectors $\mathbf{G}$ are decomposed into components parallel, $\mathbf{G}_\parallel$, and perpendicular $G_\perp\hat{\mathbf{z}}$, to the surface so that $\mathbf{G} = \mathbf{G}_\parallel + G_\perp\hat{\mathbf{z}}$, and

$$f_\ell(g) = \frac{1}{L}\int_{z_\ell-\Delta^b_\ell}^{z_\ell+\Delta^f_\ell} e^{igz}\,dz. \tag{4.20}$$

The double-summation over the $\mathbf{G}$-vectors can be efficiently done by creating a pointer array to identify all the plane-wave coefficients associated with the same $\mathbf{G}_\parallel$. We take $z_\ell$ at the center of an atom that belongs to layer $\ell$. Thus Eq. (4.9) and Eq. (4.11) give the $\ell$-th atomic layer contribution to the spin injection rate and carrier injection rate of the slab. Note that if we take the cut function $\mathcal{F}_\ell(z)$ to be unity through the whole slab, then $f_\ell(g) = \delta_{g,0}$ and from Eq. (4.19) one would recover the results for the entire slab. The contributions from the nonlocal part of the pseudopotential and from the spin-orbit interaction to the velocity matrix elements are excluded. They are not readily available and, to our knowledge, no efficient scheme that include simultaneously has been presented. Yet, it has been demonstrated that these contributions are small for Si [MNAS06, RN91, KS97]. It is well known that the DFT generally underestimates the band gap of insulators [JG89, GSS86]. A usual approach to overcome this problem is the use of the so-called scissors correction, in

| surface | $\zeta^{\mathrm{abc}}(\omega) = -\zeta^{\ell,\mathrm{acb}}(\omega)$ | | |
|---|---|---|---|
| Si(111)(1 × 1) :As | xzy | yxz | zxy |
| Si(111)(1 × 1) :H | xzy | yxz | zxy |
| Si(111)(2 × 1) | xzy xyx | yxz | zxy zyz |
| Si(111)($\sqrt{3} \times \sqrt{3}$) :In | xzy xyx | yxz | zxy zyz |

Table 4.2: Non-zero components of the layer spin injection tensor, $\zeta^{\ell,\mathrm{abc}}(\omega)$, for the surfaces considered in this work.

which the conduction bands are rigidly shifted up in energy by an amount $\Delta$ that corrects the band gap to the experimental value (see Table 4.1). The result from an analysis of the scissors-modified Hamiltonian is that the matrix elements $S^{\mathrm{a}}_{mn}(\mathbf{k})$, $r^{\mathrm{a}}_{mn}(\mathbf{k})$ and $\mathcal{R}^{\mathrm{a},\ell}_{mn}(\mathbf{k})$ are the same for both the LDA and the scissored Hamiltonian [CME+09, NOSS05, DSG93]. Since the energies are shifted, the only significant consequence is in the $\delta$ function of Eq. (4.9) and Eq. (4.11), and so the spectra corresponding to the scissored Hamiltonian are obtained by simply translating in energy the spectra calculated from the LDA Hamiltonian by the scissors correction $\Delta$.

## 4.5 Results

In Fig. 4.1 we show the different Si(111) surfaces for which we calculate the surface DSP, $\mathcal{D}^{S,\mathrm{a}}$. These surfaces are chosen on the basis that they are experimentally accessible and their reconstruction is well understood. We take the surface parallel to the $x$-$y$ plane, with the surface-normal in the $+z$ direction. The surfaces are the clean surface with a $2 \times 1$ Pandey reconstruction characterized by buckled dimers forming zigzag chains along the $y$ ($[00\bar{1}]$) direction [Pan82, RL99], for which $\xi^{S,\mathrm{xx}}(\omega) \neq \xi^{S,\mathrm{yy}}(\omega)$ [CCSC84]; the As and H covered surfaces with a $1 \times 1$ surface reconstruction, exhibitis a bulk-like hexagonal symmetry, where $\xi^{S,\mathrm{xx}}(\omega) = \xi^{S,\mathrm{yy}}(\omega)$; and finally, the In covered surface, which exhibits a rather large reconstruction with a $(\sqrt{3} \times \sqrt{3})R30^\circ$ unit cell, with 3 Si atoms by atomic layer beneath the surface and only one In atom at the surface, with $\xi^{S,\mathrm{xx}}(\omega) \neq \xi^{S,\mathrm{yy}}(\omega)$. In Table 4.2 we show the nonzero components of $\zeta^{\ell,\mathrm{abc}}(\omega)$ for all the surfaces treated in this work, satisfy $\zeta^{\ell,\mathrm{abc}}(\omega) = -\zeta^{\ell,\mathrm{acb}}(\omega)$ as can be proved from Eq. (4.9).

The slabs used to represent the surfaces mentionated above are all centrosymmetric and thus their front and back surface layer are equivalent. This

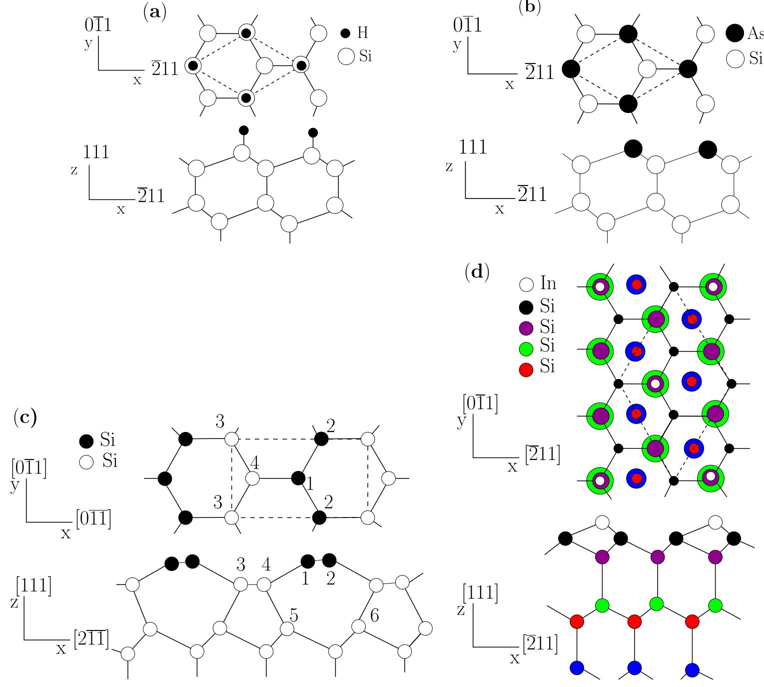


Figure 4.1: Top and side views of the (a) H and (b) As-covered Si(111) surfaces with a $1 \times 1$ relaxed unit cell; (c) clean Si(111) surface with a $2 \times 1$ relaxed unit cell; (d) In-covered Si(111) surface that relaxes with a $(\sqrt{3} \times \sqrt{3})R30°$ unit cell. All surface unit cells are denoted by dotted lines.

simplifies the expression for $\zeta^{S,\mathrm{abc}}(\omega)$ and $\xi^{S,\mathrm{ab}}(\omega)$. For instance we can write

$$\sum_{\ell=1}^{\ell_B} \tilde{\zeta}^{\ell,\mathrm{abc}}(\omega) \equiv \tilde{\zeta}^{\mathrm{half-slab,abc}}(\omega) = \frac{\tilde{\zeta}^{\mathrm{slab,abc}}(\omega)}{2}, \tag{4.21}$$

where the half-slab response which calculated by taking $\mathcal{F}_\ell(z) = 1$ either in the first or second half of the slab. Since the slab is centrosymmetric, this should be half of the full slab result, which is obtained by taking $\mathcal{F}_\ell(z) = 1$ in the whole slab. For this case, one actually does the calculation taking $\mathcal{R}^{\ell,\mathrm{a}}_{mn} \to r^{\mathrm{a}}_{mn}$, that is, like a bulk calculation with the unit cell being the whole slab. Then, using Eq. (4.21) in Eq. (4.14) we get

$$\zeta^{S,\mathrm{abc}}(\omega) = \frac{\Omega}{A}\left(\frac{\zeta^{\mathrm{slab,abc}}(\omega)}{2} - \ell_B \zeta^{\ell_B,\mathrm{abc}}(\omega)\right) \quad (N \geq N_c). \tag{4.22}$$

Likewise, Eq. (4.13) reduces to

$$\xi^{S,\mathrm{bc}}(\omega) \;=\; \frac{\Omega}{A}\Big(\frac{\xi^{\mathrm{slab,bc}}(\omega)}{2} - \ell_B \xi^{\ell_B,\mathrm{bc}}(\omega)\Big) \quad (N \geq N_c). \tag{4.23}$$

The derivation of Eq. (4.7) and Eq. (4.10) implicitly takes the electric field to be uniform in the region of interest. This is clearly inappropriate for the $z$ component of the electric field, which for semiconductors it can change by orders of magnitude as one moves from vacuum to the semiconductor. Thus, all aspects of the optical response at an interface owing to this component of the electric field would require a self-consistent calculation of the variation of $E^{\mathrm{z}}$ across the surface region. Although the calculation of this variation is an important issue, we do not address it here. Instead, we focus on the simplest experimental geometry of normal incidence. Then, since the electric field lies in the plane of the interface, it can be taken, to be uniform through the interface region neglecting the local field corrections. Then, we take a circularly left-polarized electric field propagating along the $-z$ direction,

$$\mathbf{E}(\omega) = \frac{E_0}{\sqrt{2}}\big(\hat{\mathbf{x}} - i\hat{\mathbf{y}}\big), \tag{4.24}$$

with $E_0$ being its intensity, thus Eq. (4.15) can be rewritten as

$$\mathcal{D}^{S,\mathrm{z}} \;=\; \frac{2\hat{\zeta}^{S,\mathrm{zxy}}(\omega)}{\hbar\left(\xi^{S,\mathrm{xx}}(\omega) + \xi^{S,\mathrm{yy}}(\omega)\right)/2}, \tag{4.25}$$

where we wrote $\hat{\zeta}^{S,\mathrm{zxy}}(\omega) = i\zeta^{S,\mathrm{zxy}}(\omega)$, and we used the fact that for all the surfaces considered here, $\xi^{S,\mathrm{ab}}(\omega)$ is diagonal in the adopted reference frame. We recall that the first super index in $\zeta^{S,\mathrm{abc}}$ gives the direction of the induced spin, whereas the last two are related to the exciting electric field. Thus, $\zeta^{S,\mathrm{zxy}}$ gives the spin spin injection rate with polarized along the z direction, which is the direction of propagation of the driving electric field with components along x and y.

Before we present the DSP for the above mentioned Si surfaces, we first confirm that our formalism to extract the surface response readily works. In the top panel of Fig. 4.2, we show the layer spin-injection spectra $\tilde{\zeta}^{\ell,\mathrm{zxy}}(\omega)$ for the As terminated Si(111) surface. With $\ell = 1$ that corresponds to the As layer; with $\ell = 24$ that corresponds to $\ell_B = 24$ the middle layer of the slab; we also show $\zeta^{B,\mathrm{zxy}}(\omega)$ corresponding to the bulk Si. Notice that $\zeta^{\ell=1,\mathrm{zxy}}(\omega)$ becomes non-zero at 2.2 eV, since the electronic surface sates induced by the

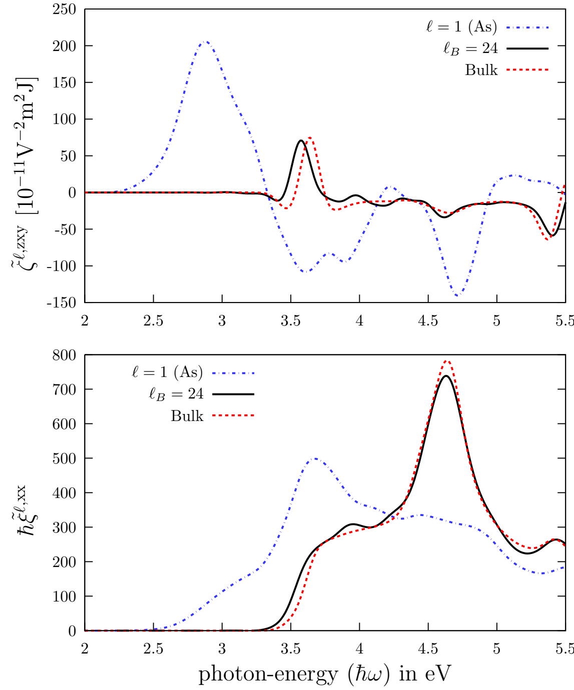


Figure 4.2: In the top panel we show the layer spin-injection spectra $\tilde{\zeta}^{\ell,\mathrm{zxy}}(\omega)$ (bottom panel $\hbar\tilde{\xi}^{\ell,\mathrm{xx}}(\omega)$) for the As-terminated Si(111) surface, where $\ell = 1$ corresponds to spectra for the As layer, $\ell = 24$ corresponds to the spectrum for the middle of the slab, and the label Bulk corresponds to the bulk spectrum.

As layer reduce the direct energy gap value of bulk Si from 3.4 eV to 2.2 eV. Thus, we see that $\zeta^{\ell_B,\mathrm{zxy}}(\omega)$ is non-zero above 3.4 eV, and that it is very similar to $\zeta^{B,\mathrm{xyz}}(\omega)$. Our calculated, spin injection spectrum, $\zeta^{B,\mathrm{zxy}}(\omega)$ agrees with that reported by Nastos et al. [NRSM+07]. In the bottom panel of Fig. 4.2 we show the carrier injection tensor spectra $\hbar\tilde{\xi}^{\ell,\mathrm{xx}} = \hbar\tilde{\xi}^{\ell,\mathrm{yy}}$ (a dimensionless quantity) for the same cases as in the top panel. Again, we see that the As-related signal is well below the bulk energy gap, and that the corresponding spectra for $\ell_B$ and bulk are almost identical. Thus, a very clear picture emerges from our formalism. For energies above at the bulk energy gap the response coming from the middle of the slab is almost identical to the bulk response, and for energies above at the surface modified energy gap, the response is surface related. We see that the surface response may also overlap with the bulk response, however from this energy on, the response would be bulk dominated.

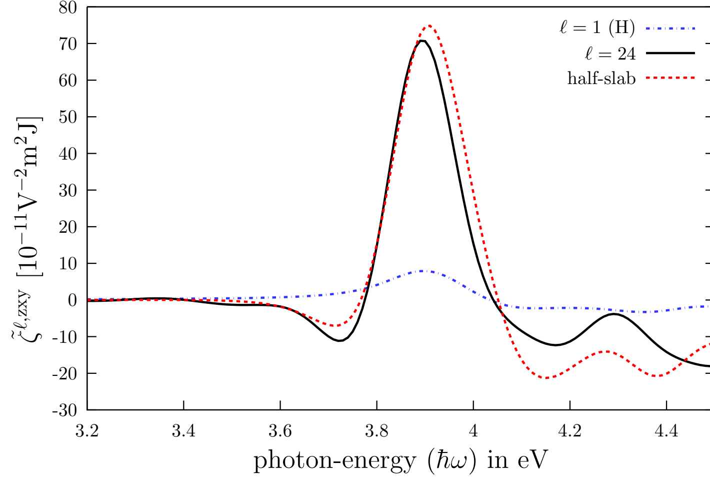


Figure 4.3: $\zeta^{\ell,\rm zxy}(\omega)$ for the H-covered Si(111) surface, where $\ell = 1$ corresponds to the H layer, $\ell = 24$ to the middle of the slab, and the half-slab value.

Therefore, our scheme clearly shows that for "low" energies the response is surface related, whereas for "high" energies the response is bulk related. To reinforce this result, we show in Fig. 4.3 the calculated values of the layer spin injection spectra, $\tilde{\zeta}^{\ell,\rm zxy}(\omega)$, for the H-terminated Si(111) surface. The H atoms quench the electronic surface states, and as a result we see that $|\tilde{\zeta}^{H,\rm xyz}(\omega)| << |\tilde{\zeta}^{\ell_B,\rm xyz}(\omega)| \sim |\tilde{\zeta}^{\rm half-slab,xyz}(\omega)|$, and thus for this surface there is no "surface" response since it entirely overlaps with the bulk response. This shows that the surface response ought to be calculated with care, since one has to calculate both the surface response and the bulk response to clearly separate the latter from the former. If we apply Eq. (4.15) naively we would get not finite values which of course is inconsistent, but all this means that there is no "low" energy surface response for the H covered Si(111) surface.

Now, we move to the DSP results. In Fig. 4.4 we show the DSP spectrum $\mathcal{D}^{S,\rm z}$ for the clean Si(111) surface. Wherein we see a sharp onset of $\mathcal{D}^{S,\rm z}$ just above the band gap edge, with a maximum signal of 36%; then the spectrum remains positive and is almost zero above $\sim$ 1 eV. In Fig. 4.5 we show the DSP spectrum $\mathcal{D}^{S,\rm z}$ for the Si(111) As covered surface. Notice that as in the previous surface, the signal rises sharply just after the band edge (2.2 eV) and remains at $\sim$ 44% for almost 100 meV after the band gap edge. For energies

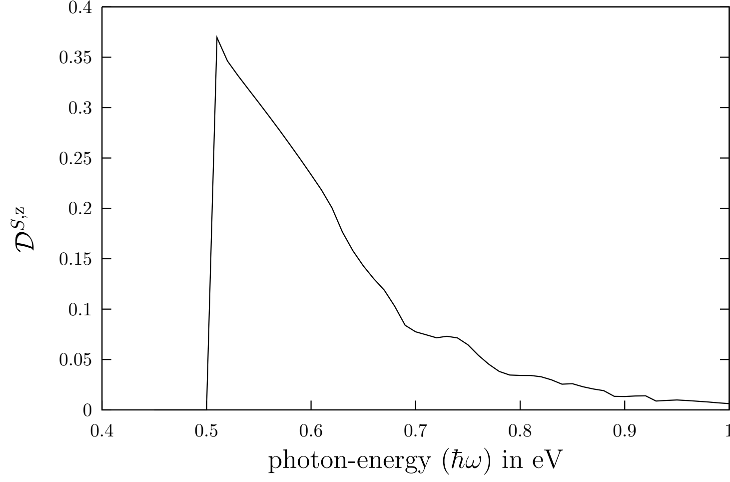


Figure 4.4: We show the DSP spectrum $\mathcal{D}_s^{\mathrm{z}}(\omega)$, for the clean Si(111) surface as a function of the incoming photon energy at normal incidence.

greater than 2.3 eV, $\mathcal{D}^{S,\mathrm{z}}$ starts to decay to zero almost monotonically. Finally, in Fig. 4.6 we show the DSP spectrum $\mathcal{D}^{S,\mathrm{z}}$ for the In-covered Si(111) surface. In contrast with the previous surfaces, we see a rich spectral dependence, and that $\mathcal{D}^{S,\mathrm{z}}$ is mainly negative, meaning that the spin polarizes opposite to the direction of the propagation of the left-circularly polarized electric field, that is towards the surface. The onset of the signal $\mathcal{D}^{S,\mathrm{z}}$ is still at the band gap edge wherein reaches a value of -34%, similar to the previous surfaces. The maximum spin polarization value, -52%, is almost 120 meV above the band gap. The $\mathcal{D}^{S,\mathrm{z}}$ spectrum shows a rapid change from -16% to 12% at a photon energy of $\sim$ 2.23 eV, and above this value it is almost zero.

To understand the main features shown by the DSP spectrum $\mathcal{D}^{S,\mathrm{z}}(\omega)$ of any of the previous surfaces, we can analyse the corresponding surface spin injection spectrum, $\zeta^{S,\mathrm{zxy}}(\omega)$, according to the contributions coming from electron transitions between any valence band to any conduction band. In particular, we show in Fig. 4.7 $\zeta^{S,\mathrm{zxy}}(\omega)$ for selected transitions between the spin-split valence and conduction bands of the In-covered Si(111) surface. We label the bands from the bottom conduction band $c_1$, to the higher consecutive conduction bands as $c_2, c_3, \cdots$, and from the top valence band $v_1$, to the lower consecutive valence bands as $v_2, v_3, \cdots$. We see how the onset of the response is mainly given by contributions of the transitions $v_1 \to c_1$, $v_1 \to c_2$, $v_2 \to c_1$,

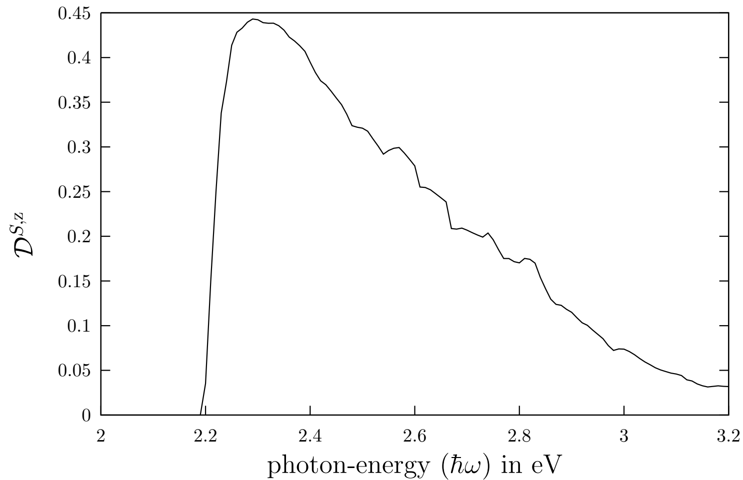


Figure 4.5: We show the DSP spectrum $\mathcal{D}^{S,\mathrm{z}}(\omega)$ for the As covered Si(111) surface as a function of the incoming photon energy.

and $v_2 \rightarrow c_2$, which are the transitions from the top-two spin-split valence bands to the bottom-two spin-split conduction bands. From Fig. 4.7 we see that these are the transitions that contribute to the first minimum of $\mathcal{D}^{S,\mathrm{z}}$. On the other hand, the minimum of $\zeta^{S,\mathrm{zxy}}(\omega)$ at around 2.09 eV mainly comes from the transitions $v_1 \rightarrow c_{3,4}$ and $v_2 \rightarrow c_{3,4}$. It is interesting to note that the $v_{1,2} \rightarrow c_2$ transitions contributes with an almost constant signal, whereas the $v_{1,2} \rightarrow c_1$ transitions are positive around the 2.09 peak, thus subtracting spin injection from the corresponding contributions of the other transitions. In turn, these are the transitions responsible for the minimum around 2.09 of $\mathcal{D}^{S,\mathrm{z}}$ shown in Fig. 4.6. We also see that a given transition injects spin with a very different spectral dependence, energy onset and sign, which could even change as a function of photon energy. For example, we also show the contribution from $v_3 \rightarrow c_1$ that is responsible for the local maximum of the total spin injection signal at 2.03 eV. Likewise we can identify the transitions responsible for any of the features in $\zeta^{S,\mathrm{zxy}}(\omega)$, and from these the actual line shape in $\mathcal{D}^{S,z}$ of the clean and As covered Si(111) surfaces shown in Fig. 4.4 and Fig. 4.5, respectively.

From the calculations presented above we see that studied the surfaces have a different optical response depending on the magnitude and spectral shape of the injected spin polarization. The onset of the spin injection spectrum oc-

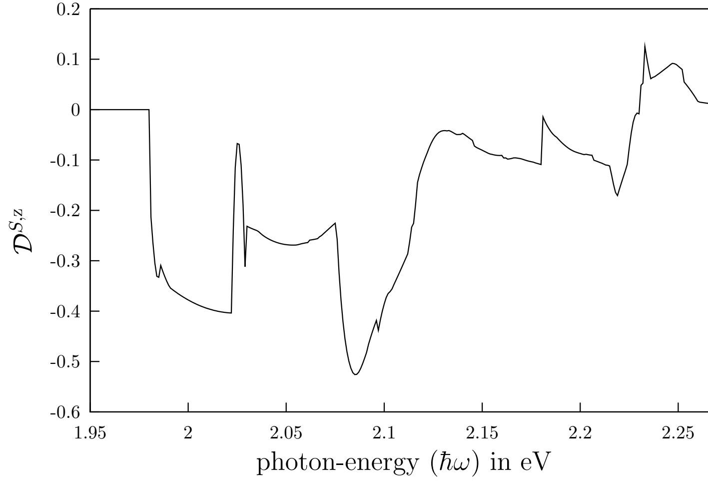


Figure 4.6: The DSP spectrum, $\mathcal{D}^{S,z}(\omega)$, for the In-covered Si(111) surface as a function of the incoming photon energy.

curs at very different energies, from the infrared, for the clean Si(111)$2 \times 1$ surface, (see Fig. 4.4) to the visible (green-yellow), for the As-covered Si(111) surface (see Fig. 4.5). The maximum value of $\mathcal{D}^{S,z}(\omega)$ can arise not just above the band gap, but also at higher energies, as in the In-covered surface (see Fig. 4.6). Part of the difference in the injected spin polarization can be understood by the fact that the spin-orbit coupling, which allows the incident light to distinguish between the two (opposite) electronic spin states, is larger for heavier atoms. Thus the clean surface, has the smaller $\mathcal{D}^{S,z}$ with a porcentage value of 36%, followed in size by the As-covered surface with 44%, and then by the In-terminated surface with 52%. It is very interesting that, except for the H-covered Si(111) surface, where there is no "surface" contribution separable from the "bulk" contribution, the other surfaces show a sizable surface spin polarization, specially when compared with bulk Si for which $\mathcal{D}^{B,z}|_{\max} = -30\%$ at 3.4 eV [NRSM+07], thus indicating that the Si(111) surfaces could be better candidates to optically polarize the electron spin with the added advantage of having different photon energies to chose from.

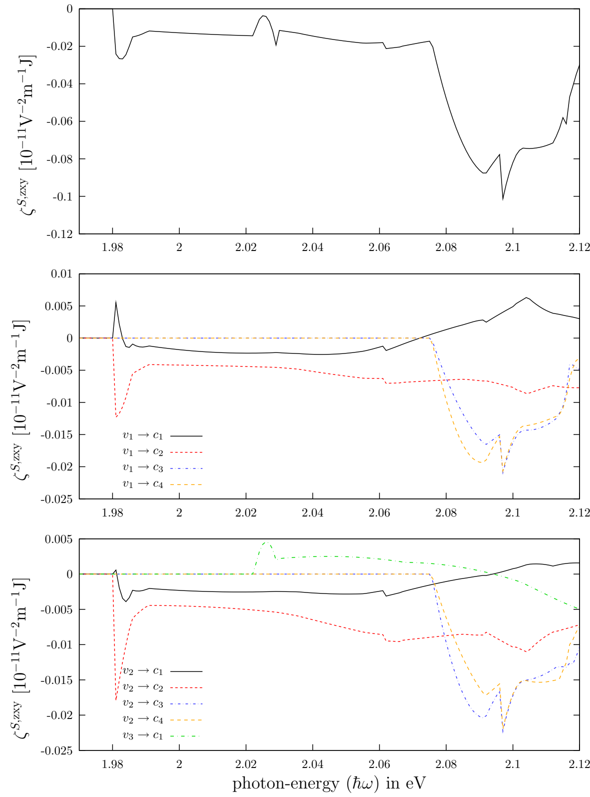


Figure 4.7: The surface spin injection spectrum, $\zeta^{S,\mathrm{zxy}}(\omega)$, (top panel) for the In-covered Si(111) surface and its contributions (middle and bottom panels) for selected transitions between spin-split valence ($v_n$) and conduction ($c_n$) bands (see text for details).

## 4.6 Conclusions

We have presented a systematic scheme to calculate the degree of spin polarization from semiconductor surfaces, where the corresponding contribution of any given layer of the slab can be calculated. The coherent excitation of the spin-split bands of the semiconductor were included. We have neglected local field and excitonic effects as well as the contributions to the velocity matrix elements from the nonlocal part of the pseudopotential. The inclusion of any of these effects is a theoretical challenge that should be addressed. We used the ABINIT plane-wave code to calculate the degree of spin polarization for several

Si(111) surfaces, and showed that these surfaces present very interesting spectra. The largest degree with which the spin can be polarized is 36% at 0.5 eV for the clean surface, 44% at 2.2 eV for the As-covered surface, and 52% at 2.08 eV for the In-covered surface. All of these values are larger than that of bulk Si, which is only 30% at 3.4 eV. However, for the H-covered surface it is not possible to separate the surface spin polarization from bulk spin polarization, being what one should expect as the H atoms basically quench the surface electronic states. Since the degree of spin polarization has been measured in bulk GaAs [BNK+05], and agrees rather well with the calculation [NRSM+07], we hope that the present investigations will motivate corresponding experiments at Si(111) surfaces. Appropriately chosen or designed surfaces are good venues for the optical injection of spin polarized electrons and, needless to say, one can use this fact either to characterize the surface itself, or to exploit the richness of the effect for practical applications in spintronics.

Chapter 5

# Stress modulated optical spin-injection in bulk semiconductors

---

**Contents**


5.1 Summary . . . 75
5.2 Introduction . . . 75
5.3 Theory . . . 76
5.4 Results . . . 78
5.5 Conclusions . . . 85


## 5.1 Summary


A full band-structure *ab initio* calculation of the degree of spin polarization (DSP) in stressed bulk Si and bulk GaAs is reported. For Si, we found that compressive stress causes the DSP signal peak to decrease slightly in magnitude and to shift to higher energies. For expansive stress, the DSP signal shows a notable enhancement, changing from -31.5% for the unstressed case to +50% with only 1.5% of volumetric change. For GaAs, the only change induced due to either expansive or compressive stress is an energy shift of the DSP spectrum. This behaviour may serve to tune the DSP in semiconductors to a suitable laser energy.


## 5.2 Introduction

The study of spin injection into a non-magnetic semiconductor is an important field of research in condensed matter physics, known as spintronics, which

has the potential of many applications [ZFS04]. The optical excitation of semiconductors with circularly polarized light creates spin-polarized electrons in the conduction bands [DP84]. The idea of using light for spin injection and detection dates back to 1968 [Lam68]. Later it was shown that conversion of angular momentum of light into electron spin and viceversa is very efficient in III-V semiconductors [DP84]. Known as “optical orientation”, this effect serves as an important tool in the field of spintronics, where it is used to spin-polarize electrons. The injection of spin and the DSP in bulk GaAs, Si and CdSe semiconductors has been reported recently [NRSM+07], where a detailed comparison between a 30-band $\mathbf{k}\cdot\mathbf{p}$ model and a full band structure LDA (local density approximation) + scissors correction calculation was given. Some of the results obtained could be explained simply by using well-known features of the band structure and selection rules around the $\Gamma$ points of GaAs and Si. However, for photon energies well above the band gap, the selection rules are more complicated, and full band structure calculations are required to explore the DSP. For many semiconductors, like CdSe, no $\mathbf{k}\cdot\mathbf{p}$ models are available, and the results of Nastos et al. [NRSM+07] indicate that the DSP can be reliably calculated with LDA + scissors corrected band structures. This suggests a program of study of optical orientation based on LDA + scissors calculations.

The purpose of this chapter is to calculate the DSP in stressed bulk Si and stressed bulk GaAs. We characterized the applied stress by isometric volumetric strains, where the ratio of the volume at the stressed state to the volume at the unstressed state is employed as the independent input variable. We compute the DSP for a set of volumetric strains. To avoid structural changes, which are reported to arise at about 10% of volumetric change [tur], we restricted our computations between the range of 1.5% of expansive strain and −1.5% of compressive strain.

The chapter is organized as follows: In Section 5.3 we briefly describe the theoretical approach for the calculation, in Section 5.4 the results are presented and in Section 5.5 the conclusions are given.

## 5.3 Theory

The theory of DSP is laid out in the previous chapter (Chapter 4) where we refer the reader for details. Here, we only reproduce the most important expressions in order to calculate the DSP, which is formally defined along the

"a" direction as

$$\mathcal{D}^{\rm a} = \frac{\dot{S}^{\rm a}}{(\hbar/2)\dot{n}}, \tag{5.1}$$

where the rate of spin injection is given by $\dot{S}^{\rm a} = \zeta^{\rm abc}(\omega)E^{\rm b}(-\omega)E^{\rm c}(\omega)$ and the rate of carrier injection by $\dot{n} = \xi^{\rm ab}(\omega)E^{\rm b}(-\omega)E^{\rm c}(\omega)$. Also,

$$\begin{aligned} \zeta^{\rm abc}(\omega) &= \frac{i\pi e^2}{\hbar^2}\int \frac{d^3k}{8\pi^3}\sum_{vcc'}{}' \,{\rm Im}\Big[S^{\rm a}_{c'c}(\mathbf{k})r^{\rm b}_{vc'}(\mathbf{k})r^{\rm c}_{cv}(\mathbf{k}) \\ &+ S^{\rm a}_{cc'}(\mathbf{k})r^{\rm b}_{vc}(\mathbf{k})r^{\rm c}_{c'v}(\mathbf{k})\Big]\delta(\omega_{cv}(\mathbf{k})-\omega), \end{aligned} \tag{5.2}$$

is the (purely imaginary) pseudo-tensor that allows us to calculate the spin injection rate, and

$$\xi^{\rm ab}(\omega) = \frac{2\pi e^2}{\hbar^2}\int \frac{d^3k}{8\pi^3}\sum_{vc}{\rm Re}[r^{\rm a}_{vc}(\mathbf{k})r^{\rm b}_{cv}(\mathbf{k})]\delta(\omega_{cv}(\mathbf{k})-\omega), \tag{5.3}$$

is the tensor that allows us to calculate the carrier injection. In the expressions above we have substituted $\mathcal{R}^a_{nm}$ with its corresponding bulk value $r^a_{nm}$ (see Eqs. 4.9 and 4.11). The roman Cartesian superscripts are summed over if repeated. Eq. (5.2) takes into account the excited coherences of the conduction bands that are spin split by a small amount, typically smaller than the laser pulse energy width. Thus, this pulse excites a coherent superposition of two conduction bands. Even for very long pulses with narrow energy widths, dephasing effects lead to an energy width of the bands large enough so that spin-split states can become quasi-degenerate. Thus, these coherences were included by solving the equation of motion for the single particle density matrix with the use of a multiple scale approach [NRSM+07]. Therefore, the prime in the sum of Eq. (5.2) is restricted to quasi-degenerated conduction bands $c$ and $c'$ that are closer than 30 meV, where this value is both a typical laser pulse energy width and the room temperature energy [NRSM+07]. As we show later, neglecting these coherences leads to wrong results. The matrix elements of the position operator $r^{\rm a}_{nm}(\mathbf{k})$, the spin operator $S^{\rm a}_{nm}(\mathbf{k})$, and the energy difference between valence ($v$) and conduction ($c$) states, $\omega_{cv}(\mathbf{k})$, are evaluated for **k**-points on a specially determined tetrahedral grid. This grid is used in the integrals of Eqs. (5.2) and (5.3) that are calculated through a linear analytic tetrahedral integration method [NRSM+07]. We assume that the hole spins relax very quickly and we neglect them [DP84], focusing only on the electron

spins; measurements have led to estimates of 110 fs for the heavy-hole spin life time in GaAs [HT02]. We mention that the theoretical scheme neglects many particle effects, electron energy thermalization, electron-hole recombination and phonon interaction, the latter limits the results to absorption across the direct band. The treatment of above effects is a theoretical challenge that ought to be pursued.

## 5.4 Results

The calculations were performed in the framework of DFT within LDA + scissors correction by using ABINIT plane-wave code [GBC+02]. To include the spin-orbit interaction, we use the separable Hartwigsen-Goedecker-Hutter pseudopotentials [HGH98] within LDA as parametrized by Goedecker et al. [GTH96]. We exclude the semi-core states and the contributions to the velocity matrix elements from the nonlocal part of the pseudopotential. However, we know that this contributions are small for Si [MNAS06, RN91, KS97]. The scissors correction causes a rigid shift of the spectrum of $\mathcal{D}^a$ along the energy axis by 0.87 eV for Si and 1.16 eV for GaAs, these values are required to increase the LDA gap, at the $\Gamma$ point, to their experimental value [CME+09, NOSS05]. Since the core electrons are neglected, we have 8 electrons in the primitive unit cell with either spin up or spin down wave functions, and thus 8 valence bands. Consequently we found converged results with just 8 conduction bands, along with a cut-off energy of 30 Hartree and 18424 **k**-points.

For Si and GaAs their corresponding crystal classes have the following non-zero components for the spin injection tensor: $\zeta^{\rm zxy} = \zeta^{\rm yzx} = \zeta^{\rm xyz} = -\zeta^{\rm zyx} = -\zeta^{\rm yxz} = -\zeta^{\rm xzy}$, and for carrier injection $\xi^{\rm xx} = \xi^{\rm yy} = \xi^{\rm zz} \equiv \xi$. Using a circularly left-polarized electric field propagating along the $-z$ direction, i.e. $\mathbf{E} = E_0(\hat{\mathbf{x}} - i\hat{\mathbf{y}})/\sqrt{2}$ with $E_0$ being its intensity, we get the DSP along the direction of propagation of the electric field as $\mathcal{D}^{\rm z} = \zeta^{\rm zxy}/(\hbar\xi/2)$ from Eq. (5.1). Because of the relatively high symmetry of Si and GaAs, the exact crystal cut is unimportant; the injected spin density will always be aligned parallel or antiparallel to the laser beam. We characterized the applied stress by isometric volumetric strains. Then, we define $\sigma = a_s/a_0$ as the ratio between the lattice parameter of the stressed state, $a_s$, to the lattice parameter of the unstressed state, $a_0$, where $a_0 = 5.39$ Å (5.53 Å), for the cubic unit cell of Si (GaAs). We use $a_s = \sigma a_0$ as the independent variable to calculate $\mathcal{D}^{\rm z}$ as a function of $\sigma$.

The calculated DSP, $\mathcal{D}^{\rm z}$, as a function of the photon energy for Si at several

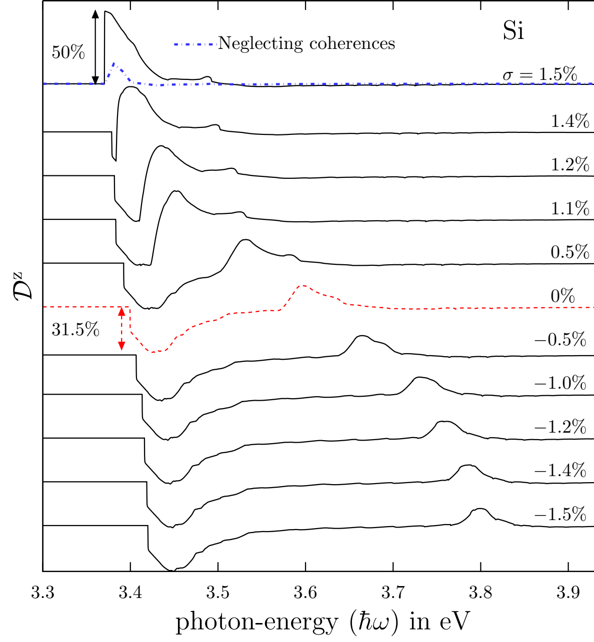


Figure 5.1: Stress modulation of the DSP, $\mathcal{D}^z$, as a function of photon energy for bulk Si. Several spectra for different percentage values of $\sigma$ are shown, where $\sigma > 0$ ($\sigma < 0$) is for expansive (compressive) stresses. The unstressed $\mathcal{D}^z$ ($\sigma = 0\%$) is shown by a red dotted line with a maximum value of $|\mathcal{D}^z| = 31.5\%$. For $\sigma = 1.5\%$, $\mathcal{D}^z|_{\text{max}} = 50\%$. Neglecting the coherences in Eq. (5.2) leads to a wrong spectrum as shown for $\sigma = 1.5\%$ (dash-dotted line). Each spectrum has been offset in the vertical axis for displaying purposes.

values of $\sigma$, including both expansive and compressive strains, along with the unstressed ($\sigma = 0$) result is shown in Fig. 5.1, varying the percentage value of $\sigma$ from $-1.5\%$ to $1.5\%$. The unstressed spectrum shows two main features: one at 3.43 eV, just a few meV above the band gap with a $-31.5\%$ deep, and the other at 3.59 eV with a 15% peak. As we compress the unit cell ($\sigma < 0$) we see that the negative dip remains almost unchanged in magnitude and energy position, however the positive peak moves towards higher energies, keeping almost the same shape and showing a modest reduction to 11% at $\sigma = -1.5\%$. This situation changes radically when we expand the unit cell. Indeed, as $\sigma$ increases the negative gets narrower, it slightly moves to lower energies and then disappears at $\sigma = 1.403\%$. The positive peak, in turn, moves to lower

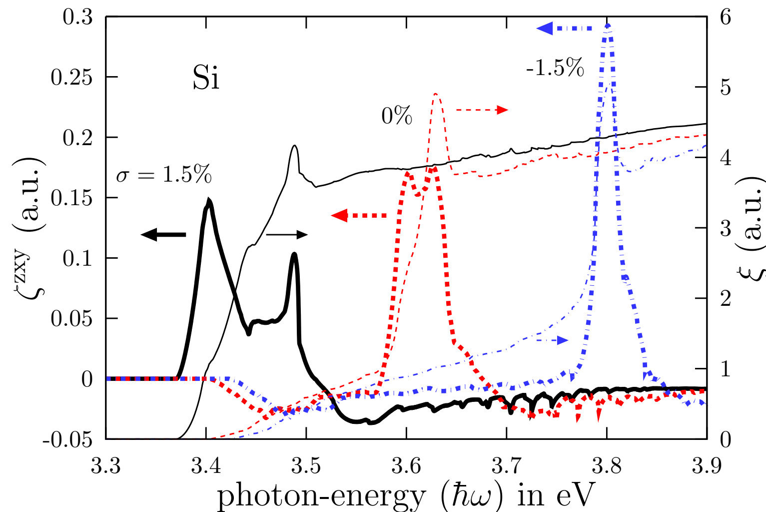


Figure 5.2: Plot of the calculated spectrum of $\zeta^{\rm zxy}(\omega)$ (thick lines) and of the spectrum of $\hbar\xi(\omega)$ (thin lines) for Si as a function of photon energy for three different values of strain $\sigma$. The horizontal arrows point to the corresponding vertical scale of $\zeta^{\rm zxy}(\omega)$ (left) and $\hbar\xi(\omega)$ (right).

energies, increases its height, and its shape changes until rises sharply at the band gap edge with a maximum percentage intensity of 50%. The spectrum at $\sigma = 1.5\%$ of the $\mathcal{D}^{\rm z}$, only shows this positive peak that has the largest $|\mathcal{D}^{\rm z}|$ magnitude of all spectra. Thus, under expansive stress, bulk Si exhibits a quite interesting response: the negative deep and positive peak shown in $\mathcal{D}^{\rm z}$ for the unstressed unit cell coalesce into a single positive peak at the band gap edge with 75% of the spins polarized along the direction of propagation of the optical beam [notf]. We have checked that for $\sigma > 1.5\%$, the $\mathcal{D}^{\rm z}$ only shifts the spectrum to lower energies, retaining the magnitude of the DSP signal peak at 50%. Nevertheless such large expansions may be experimentally more difficult to achieve [notg]. Also, in Fig. 5.1 and only for $\sigma = 1.5\%$, we plot $\mathcal{D}^{\rm z}$ without coherences, that is equivalent to putting $c = c'$ in Eq. (5.2). We see that coherences account for more than 70% of the total spectrum in this calculation, and neglecting them leads to unphysical results.

In Fig. 5.2 we show the spectrum of the spin injection tensor, $\zeta^{\rm zxy}(\omega)$ and the spectrum of carrier injection tensor, $\hbar\xi(\omega)$, for $\sigma = 0, \pm 1.5\%$. We remark that in Gaussian units both tensors are dimensionless quantities. Notice that

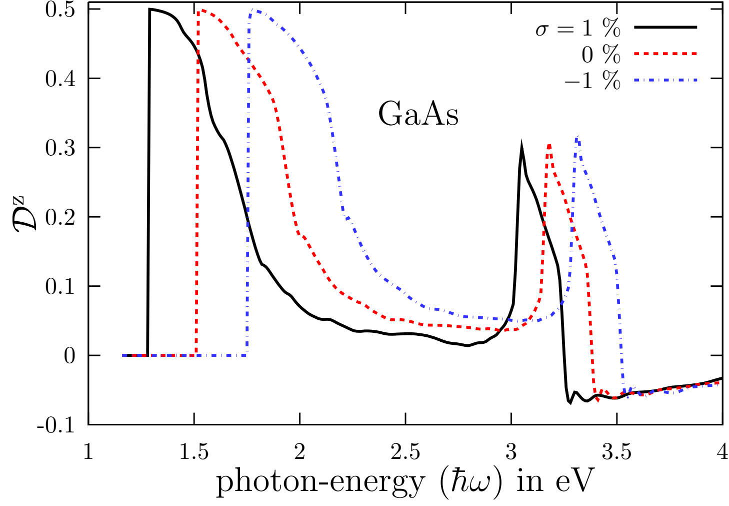


Figure 5.3: Stress modulation of the DSP, $\mathcal{D}^z$, as function of photon energy for bulk GaAs and for three values of strain ($\sigma$).

the onset of the spectra at the band gap edge is red-shifted in energy as $\sigma$ goes from $-1.5\%$ to $1.5\%$. For both $\sigma = 0$ and $-1.5\%$, $\zeta^{zxy}(\omega)$ is negative just around above the onset, whereas it is positive for $\sigma = 1.5\%$ and rises very sharply. For $\hbar\xi(\omega)$ we see that the rise of the signal at the onset also changes with $\sigma$, being rather sharp for $\sigma = 1.5\%$, as it is for $\zeta^{zxy}(\omega)$. From these results, one can understand the line shape of $\mathcal{D}^z$ shown in Fig. 5.1. Indeed, the minimum (maximum) that is present in $\mathcal{D}^z$, for $\sigma = 0, -1.5\%$, comes from the minimum (maximum) in $\zeta^{zxy}(\omega)$, whereas the only maximum of $\mathcal{D}^z$ for $\sigma = 1.5\%$, near the band gap edge comes from the maximum of $\zeta^{zxy}(\omega)$, but then the next local maximum in $\zeta^{zxy}(\omega)$, at around 3.5 eV, is barely seen in $\mathcal{D}^z$ since, as shown in the Fig. 5.2, the corresponding $\hbar\xi(\omega)$ is rather large as compared with $\zeta^{zxy}(\omega)$. In other words, the DSP depends strongly on the fine interplay between the ability of polarizing the spin of the electrons, and the number of electrons that are injected.

The calculated DSP spectrum, $\mathcal{D}^z$ as a function of the photon energy for GaAs at three values of $\sigma$: one for expansive stress ($\sigma = 1.5\%$), one for compressive stress ($\sigma = -1.5\%$) and the unstressed one($\sigma = 0\%$) are shown in Fig. 5.3. The corresponding unstressed spectrum shows two positive peaks, one at 1.5 eV, just at the band gap edge with a value of $\mathcal{D}^z = 50\%$, and the

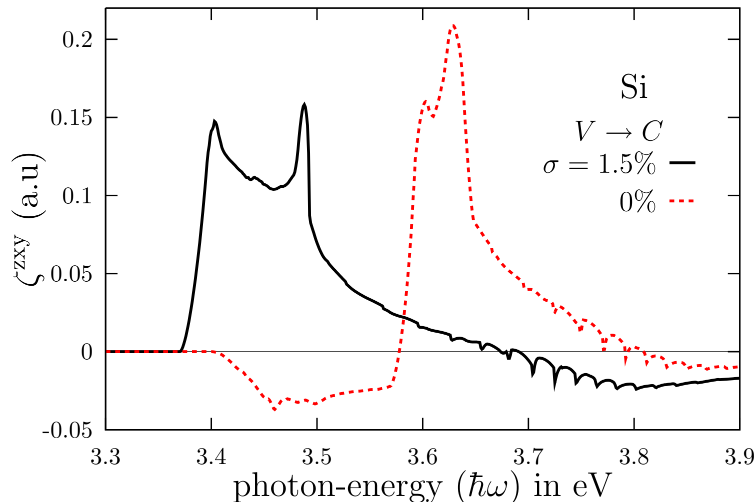


Figure 5.4: Plot of of the spectra of $\zeta^{\mathrm{zxy}}(\omega)$, for Si. The spectra correspond to transitions from the top valence band ($V$) to the bottom conduction band, ($C$) for $\sigma = 1.5\%$ and $\sigma = 0\%$.

other at 3.18 eV with a value of $\mathcal{D}^{\mathrm{z}} = 30\%$. As we expand (compress) the unit cell to $\sigma = 1\%$ ($\sigma = -1\%$) we see that the $\mathcal{D}^{\mathrm{z}}$ spectrum shifts almost rigidly along the energy axis towards lower (higher) energies, with only a very small change in the intensity of the peak at 3.1 eV. This behavior remains valid for larger values of $|\sigma|$. For the unstressed case of GaAs, the 50% value of the $\mathcal{D}^{\mathrm{z}}$ has been confirmed experimentally [BNK+05], and explained theoretically [NRSM+07], thus our calculated results indicate that either compressive or expansive strain will only move the onset of the signal. This also shows that the symmetry of the electronic band structure that leads to the results shown, for $\sigma = 0$, remains basically the same as we apply the stress [NRSM+07], in contrast with Si, where the changes of $\mathcal{D}^{\mathrm{z}}$ are readily noticeable.

To gain an understanding of the rate of spin injection in bulk si we proceed as follows. First we analyze the contribution of the different transitions to the spectrum of $\zeta^{\mathrm{zxy}}(\omega)$. In Fig. 5.4 we show $\zeta^{\mathrm{zxy}}(\omega)$ for the transitions from the top valence band ($V$) to the bottom conduction band ($C$), for $\sigma = 0$ and $\sigma = 1.5\%$. These transitions have the most influential effect on the net spin-injection rate right at the band gap edge. The $V$ ($C$) band is doubly degenerated due to the spin degree of freedom. These transitions for $\sigma =$

0 have a $\zeta^{\mathrm{zxy}}(\omega)$ that is first negative from 3.40 eV util 3.58 eV, and then becomes positive having a peak at around 3.63 and then decays to values to close o zero above 3.86 eV. However, for the same transitions at $\sigma = 1.5\%$, the corresponding $\zeta^{\mathrm{zxy}}(\omega)$ is always positive and goes to almost zero above 3.9 eV. We note that for $\sigma = 0$ the signal shits in 200 meV above the band gap, whereas for $\sigma = 1.5\%$ the signal kicks in just 32 meV above the band gap. This large difference, in turn, gives the $\mathcal{D}^{\mathrm{z}}$ observed in Fig. 5.1, i.e. for $\sigma = 0$ we have a broad minimum at 25 meV above the band gap edge, followed by a broad maximum at 195 meV above the band gap edge, whereas for $\sigma = 1.5\%$ we have a sudden build up of $\mathcal{D}^{\mathrm{z}}$ at the band edge followed by a rapid decrease of the signal to zero.

To further understand the results of the DSP, $\mathcal{D}^z$, we show in Fig. 5.5 the relevant energy bands for Si and GaAs for the corresponding $\mathbf{k}$ values that determine the onset of $\mathcal{D}^z$ for three values of $\sigma$. We show the allowed transitions between the top-valence band ($V$) and the bottom-conduction band ($C$) for an energy range of 50 meV from the corresponding energy gap, $E_g$, of each $\sigma$. Thus, we cover the spectra of $\mathcal{D}^z$ right at the onset (band gap edge) and 50 meV above it. The effect of expanding (compressing) the unit cell gives a value of the band gap, $E_g$, smaller (larger) than the corresponding value of the unstressed unit cell. This, in turn, determines the onset of $\mathcal{D}^z$ seen in the first four figures. We notice that for $\sigma = -1.5\%$ and 0% the allowed transitions for Si are only concentrated around the $\Gamma$ point, whereas for $\sigma = 1.5\%$, besides having a similar allowed transition range around $\Gamma$, there is also a rather wide range of allowed transitions along the $\Lambda$-$\mathbf{k}$ path in the Brillouin zone. This is due to the top-valence and bottom-conduction bands being almost parallel (within 50 meV) for these values of $\mathbf{k}$, a behavior that is absent for $\sigma = 0, -1.5\%$. Thus the expansion of the unit cell changes the band structure in such a way that the bottom conduction band, along $\Lambda$, becomes (almost) parallel to the top-valence band. For compression, the bottom conduction band does not change its curvature and remains the same as the corresponding band of the unstressed unit cell. The top valence band is almost insensitive to the change of the unit cell, at least for the $L$-$\Gamma$ path in the Brillouin zone, but of course this $\mathbf{k}$ range is the only one relevant for the onset of the spin polarized signal. We mention that we do not show the other energy bands, like the spin-orbit split-off band, for a clear presentation of the figure, however all the bands are properly taken into account in the calculation. In Fig. 5.5 we show the value of the $\mathbf{k}$-integrand of Eq. (5.2). We notice that for all three values of $\sigma$, the integrand is negative for values of $\mathbf{k}$ around $\Gamma$, whereas for a large set

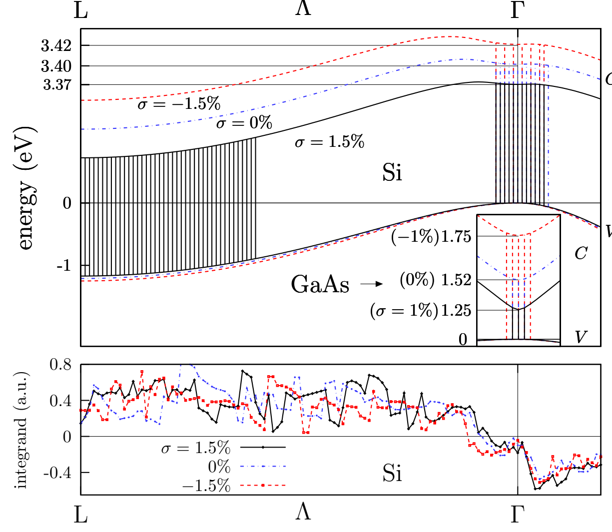


Figure 5.5: The top panel shows the valence, V, and conduction, C, bands for Si and GaAs (inset)for the corresponding **k** values that determine the onset $\mathcal{D}^z$ for three values of $\sigma$. The valence bands are plotted with the same energy scale and the conduction bands are separated in energy for displaying purposes. The vertical lines are the allowed transitions between the top-valence, $(V)$, and bottom-conduction, $(C)$, bands for an energy range of 50 meV from the corresponding energy gap, $E_g$, of each $\sigma$. The vertical axis is not drawn to scale and the $E_g(\sigma)$ is shown for reference. The bottom panel shows the integrand of Eq. (5.2) for Si along the same $\Lambda$-**k** path. Note that no other energy bands are shown, in particular the spin-orbit split-off bands, although all the bands are included in the calculation.

of values of **k** towards $L$ along the $\Lambda$ line, the integrand is positive. Thus, as all the allowed transitions for $\sigma = -1.5\%$ and 0% are concentrated around $\Gamma$ the corresponding values of $\zeta^{zxy}(\omega)$ are negative. In contrast, for $\sigma = 1.5\%$ the number of allowed transitions along the $\Lambda$ line, with a positive integrand, are much greater than those around the $\Gamma$ point, with negative integrand, thus resulting in positive values for $\zeta^{zxy}(\omega)$ and $\mathcal{D}^z$ as shown in Figs. 5.2, 5.4 and 5.1, respectively. On the other hand, as we can see from Fig. 5.5, for GaAs, the all allowed transitions are concentrated around $\Gamma$, and the integrand (not shown) is only positive for the three values of $\sigma$. As a result we observe in Fig. 5.3, an almost rigid shift of the spectrum $\mathcal{D}^z$ as a function of $\sigma$, with no

change of sign, in contrast to Si. A similar analysis could be carried out for any other energy like, for instance, the sudden change of sign seen at $\sim 3.6$ eV in Fig. 5.4, where transitions from other energy bands would be responsible for the signal.

## 5.5 Conclusions

We have presented a study of optical spin injection rate for stressed bulk Si and stressed bulk GaAs. Both compressive and expansive stress can effectively modulate the degree of spin polarization in these materials. For bulk Si, compressive stress shifts the positive peak of $\mathcal{D}^z$ to higher energies and diminishes the signal about 20% of its corresponding value for the unstressed case. On the other hand, the negative dip remains almost unchanged both in energy position and magnitude. On the contrary, for expansive stress we found that the DSP signal just above the band gap is notably enhanced with respect to that of unstressed spectrum. For 1.5% of volumetric change, the line shape of the signal changes from negative deep and a positive peak to two positive peaks, one dip at the band edge with 50% of DSP and the other with an almost negligible magnitude. Thus, expansive strain changes the DSP just above the band gap from a value of $-31.5\%$ of the unstressed case a value of 50%. Further expansion shifts this positive peak to lower energies without changing its magnitude. For bulk GaAs, compressive and expansive stress rigidly shift the spectrum to higher or lower energies, respectively, maintaining the band gap edge peak signal at 50%. The results presented in this chapter show that the application of stress can be employed to tune the material to a suitable photon energy at which the net value of DSP is highest, making this material just as efficient as GaAs. We believe this calculations may motivate researchers to verify experimentally the theoretical results presented here.

Chapter 6

# General conclusions

In the first part of this thesis we have derived the susceptibility tensors with and without the scissors operator by solving the density matrix equation of motion through a perturbative technique. We used two well-known approaches, colloquially referred to as the "velocity gauge" and the "length gauge". New correction terms for the velocity gauge susceptibility related to the non-local nature of the scissors operator were obtained. These terms, not considered before in the literature, are crucial in order to obtain gauge invariance. We have presented numerical results for GaAs using a pseudopotential scheme and an all-electron scheme. Besides providing a numerical verification of gauge invariance for the unscissored and the scissored Hamiltonian calculations, we have shown the kind and size of error when the non-local nature of the pseudopotentials is neglected. From these results we found that it affects both the strength and line shape of the spectrum.

In the second part of this work we developed a layer-by-layer formalism of the injection current in order to calculate it at the surface of semiconductor crystals. Following the layer-by-layer approach we derived the macroscopic response tensor that describes the surface injection current. We performed *ab-initio* calculations in several surfaces, where the layer-by-layer analysis proved to be crucial in order extract the response of each atomic layer. From this work we found that the surface injection current is sensitive to the adsorbates and surface reconstruction. Numerical estimates indicate that the surface injection current should be measurable. Thus, the injection current offers the possibility of using optical coherent control to manipulate the electrons at the surface and a new technique for surface analysis.

In the third part of this thesis we presented a systematic scheme to calculate the degree of spin polarization from semiconductor surfaces, where the contribution of any given layer of a material slab can be calculated. We calculated the degree of spin polarization for several Si(111) surfaces, and showed that these surfaces present very interesting spectra. The highest degree of spin

polarization was estimted to be 36%, at 0.5 eV, for a clean surface, 44% at 2.2 eV, for a As-covered surface, and 52%, at 2.08 eV, for an In-covered surface. All these values are larger than that of bulk Si, which is only 30% at 3.4 eV. Since there is an equal population of spin-up and spin-down electrons in equilibrium, the excess of optically injected spins, accounted for by the degree of spin polarization, should be added to the existing population. Appropriately chosen or designed surfaces are attractive candidates for optical spin injection and, needless to say, one can use this fact either to characterize the surface itself, or to exploit the richness of the effect for practical applications in spintronics.

In the last part of this thesis we presented a study of optical spin injection rate for stressed bulk Si and stressed bulk GaAs. Both compressive and expansive stress can effectively modulate the degree of spin polarization (DSP) in these materials. For bulk Si, compressive stress shifts the positive peak of $\mathcal{D}^{\rm z}$ to higher energies and diminishes the signal about 20% of its value from the unstressed case. Expansive strain changes the DSP from $-31.5\%$ of the unstressed case to 50%. Further expansion shifts this positive peak to lower energies without changing its magnitude. For bulk GaAs, compressive and expansive stress rigidly shift the spectrum of the $\mathcal{D}^{\rm z}$ to higher or lower energies, respectively, maintaining the band gap edge peak signal at 50%. The results obtained in this work shows that the application of stress can be employed to tune the material to a suitable photon energy at which the net value of DSP, for the case of Si, is highest making this material just as efficient as GaAs and a good candidate to build spintronic devices.

Appendix A

# Curriculum Vitae

---

Papers

1. J. L. Cabellos, Bernardo S. Mendoza, M. A. Escobar, F. Nastos and J. E. Sipe, *Effects of nonlocality on second-harmonic generation in bulk semiconductors* Phys. Rev. B, **15** 155205, (2009). Based on Chapter 2.

2. J. L. Cabellos, Cuauhtémoc Salazar, and Bernardo S. Mendoza, *Stress modulated optical spin-injection in bulk Si and GaAs semiconductors* Phys. Rev B, **80** 245204, (2009). Based on Chapter 5.

3. J. L. Cabellos, Cuauhtémoc Salazar, and Bernardo S. Mendoza, *Optical spin injection in semiconductors*, Proceedings of international school of solid state physics, Epioptics (World Scientific) 2008, Erice, Sicily Italy.

4. *Optical Current Injection at Surfaces*, in preparation. Based on Chapter 3, to be submitted to Phys. Rev. B.

5. *One photon spin injection at surfaces*, in preparation. Based on Chapter 4, to be submitted to Phys. Rev. B.

Scientific Meetings

1. J. L. Cabellos, Bernardo S. Mendoza, F. Nastos and J. E. Sipe, *Contribucion del pseudopotencial no local a los elementos de matriz del operador momento*, XLIX Congreso Nacional de Física, presentación oral, Octubre 2006, San Luis Potosi.

2. J. L. Cabellos, Bernardo S. Mendoza, F. Nastos and J. E. Sipe, *Optical injection current in semiconductor surfaces*, L Congreso Nacional de Física, presentación mural, Noviembre 2007, Veracruz, Ver.

3. J. L. Cabellos, Bernardo S. Mendoza, M. A. Escobar, F. Nastos and J. E. Sipe, *Longitudinal versus transversal gauge theory of second harmonic generation for semiconductors*, LI Congreso Nacional de Física, presentación mural, Octubre 2008, Zacatecas, Zac.

4. J. L. Cabellos, Bernardo S. Mendoza, N. Arzate, F. Nastos and J. E. Sipe, *Optical spin injection in Si(111) surfaces*, Talk, Optics of Surfaces and Interfaces, June 2007, Wyoming, USA.

# Bibliography

[AB98] B. Adolph and F. Bechstedt. Ab initio second-harmonic susceptibilities of semiconductors: Generalized tetrahedron method and quasiparticle effects. *Phys. Rev. B*, 57(11):6519, Mar 1998. 7, 27

[AS95] Claudio Aversa and J. E. Sipe. Nonlinear optical susceptibilities of semiconductors: Results with a length-gauge analysis. *Phys. Rev. B*, 52(20):14636, Nov 1995. 6, 7, 21, 29, 35

[AS96] Claudio Aversa and J. E. Sipe. Coherent current control in semiconductors: a susceptibility perspective. *Quantum Electronics, IEEE Journal of*, 32(20):1570–1573, Sep 1996. 35

[Asp72] D. E. Aspnes. Energy-band theory of the second-order nonlinear optical susceptibility of crystals of zinc-blende symmetry. *Phys. Rev. B*, 6(12):4648–4659, Dec 1972. 6

[BD03] S. Bergfeld and W. Daum. Second-harmonic generation in GaAs: Experiment versus theoretical predictions of $\chi^{xyz}$. *Phys. Rev. Lett.*, 90(3):036801, Jan 2003. 27, 28, 96

[Blo62] E. I. Blount. *Solid State Physics.* Edited by F. Seitz and D. Turnbull, Vol. 13, pp. 305, 1962. 29

[BM63] P. N. Butcher and T. P. McLean. The non-linear constitutive relation in solids at optical frequencies. *Proc. Phys. Soc.*, 81(2):219, Oct 1963. 6

[BNK+05] R. D. R. Bhat, P. Nemec, Y. Kerachian, H. M. van Driel, J. E. Sipe, and Arthur L. Smirl. Two-photon spin injection in semiconductors. *Physical Review B*, 71(3):035209, 2005. 74, 82

[Boo57] Book, 1957. With this approximation, the expectation of any single particle operator leads to the same result obtained by a many body formulation, see W. Kohn and J. Luttinger, Phys. Rev. 108, 590 (1957). 58

[BSM+01] P. Blaha, K. Schwarz, G. K. H. Madsen, D. Kvasnicka, and J. Luitz. *WIEN2K*, an augmented plane wave + local orbitals

program for calcualting crystal properties. *WIEN2K, An Augmented Plane Wave + Local Orbitals Program for Calculating Crystal Properties*, 2001. (Karlheinz Schwartz, Techn. Universität Wien, Austria). 22, 23, 28

[cab] J. L. Cabellos, private communication. 18

[CCSC84] P. Chiaradia, A. Cricenti, S. Selci, and G. Chiarotti. Differential reflectivity of Si(111)$2 \times 1$ surface with polarized ligh: A test for surface structure. *Phys. Rev. Lett.*, 52:1145–1147, 1984. 65

[CFD$^+$99] D. Côté, J. M. Fraser, M. Decamp, P. H. Bucksbaum, and H. M. van Driel. Thz emission from coherently controlled photocurrents in GaAs. *Applied Physics Letters*, 75(25):3959–3961, 1999. 46, 48

[CLvD02] D. Côté, N. Laman, and H. M. van Driel. Rectification and shift currents in GaAs. *Applied Physics Letters*, 80(6):905–907, 2002. 46

[CME$^+$09] J. L. Cabellos, Bernardo S. Mendoza, M. A. Escobar, F. Nastos, and J. E. Sipe. Effects of nonlocality on second-harmonic generation in bulk semiconductors. *Phys. Rev. B*, 80(15):155205, 2009. 42, 65, 78

[CMN$^+$] J.L. Cabellos, B.S. Mendoza, F. Nastos, A. Shkrebtii, and J.E. Sipe. Optical current injection at surfaces, in preparation. 56, 58, 61

[CMS$^+$03] C. Castillo, Bernardo S. Mendoza, W. G. Schmidt, P. H. Hahn, and F. Bechstedt. Layer-by-layer analysis of surface reflectance anisotropy in semiconductors. *Phys. Rev. B*, 68(4):041310, Jul 2003. 36, 56, 58

[CvSK06] Athanasios N. Chantis, Mark van Schilfgaarde, and Takao Kotani. *Ab Initio* prediction of conduction band spin splitting in zinc blende semiconductors. *Physical Review Letters*, 96(8):086405, 2006. 58

[DMG01] M.C. Downer, Bernardo S. Mendoza, and V.I. Gavrilenko. Optical second harmonic spectroscopy of semiconductor surfaces: advances in microscopic understanding. *Surf. Interface Anal.*, 31:966, Apr 2001. 34

[DP84] M. I. Dyakonov and V. I. Perel. *Optical Orientation*. Edited by F. Meier and B. P. Zakharchenya (Elsevier, Amsterdam) chap. 2, pp. 11-71, 1984. 56, 59, 76, 77

[Dre55] G. Dresselhaus. Spin-orbit coupling effects in zinc blende structures. *Phys. Rev.*, 100(2):580, Oct 1955. 58

[DSG93] R. Del Sole and Raffaello Girlanda. Optical properties of semiconductors within the independent-quasiparticle approximation. *Phys. Rev. B*, 48(16):11789–11795, Oct 1993. 12, 65

[ETP+01] L. A. Eyres, P. J. Tourreau, T. J. Pinguet, C. B. Ebert, J. S. Harris, M. M. Fejer, L. Becouarn, B. Gerard, and E. Lallier. All-epitaxial fabrication of thick, orientation-patterned GaAs films for nonlinear optical frequency conversion. *Applied Physics Letters*, 79(7):904–906, 2001. 26

[GBC+02] X. Gonze, J.M. Beuken, R. Caracas, F. Detraux, M. Fuchs, G.-M. Rignanese, L. Sindic, M. Verstraete, G. Zerah, F. Jollet, M. Torrent, A. Roy, M. Mikami, Ph. Ghosez, J.-Y. Raty, and D.C. Allan. First-principles computation of material properties : the abinit software project. *Computational Materials Science*, 25:478, 2002. (URL http://www.abinit.org). 23, 28, 78

[GMS91] Ed Ghahramani, D. J. Moss, and J. E. Sipe. Full-band-structure calculation of second-harmonic generation in odd-period strained $(\mathrm{Si})_n/(\mathrm{Ge})_n$ superlattices. *Phys. Rev. B*, 43(11):8990–9002, Apr 1991. 6, 7, 14, 17, 18, 19

[GSS86] R. W. Godby, M. Schlüter, and L. J. Sham. Accurate exchange-correlation potential for silicon and its discontinuity on addition of an electron. *Phys. Rev. Lett.*, 56(22):2415, Jun 1986. 64

[GTH96] S. Goedecker, M. Teter, and J. Hutter. Separable dual-space gaussian pseudopotentials. *Phys. Rev. B*, 54(3):1703, Jul 1996. 41, 63, 78

[HDSO03] Conor Hogan, Rodolfo Del Sole, and Giovanni Onida. Optical properties of real surfaces from microscopic calculations of the dielectric function of finite atomic slabs. *Phys. Rev. B*, 68(3):035405, Jul 2003. 36, 56, 58

[HGH98] C. Hartwigsen, S. Goedecker, and J. Hutter. Relativistic separable dual-space gaussian pseudopotentials from H to Rn. *Phys. Rev. B*, 58(7):3641, Aug 1998. 41, 63, 78

[HL86] Mark S. Hybertsen and Steven G. Louie. Electron correlation in semiconductors and insulators: Band gaps and quasiparticle energies. *Phys. Rev. B*, 34(8):5390–5413, Oct 1986. 10

[HS96] James L. P. Hughes and J. E. Sipe. Calculation of second-order optical response in semiconductors. *Phys. Rev. B*, 53(16):10751–10763, Apr 1996. 6, 27

[HT02] D. J. Hilton and C. L. Tang. Optical orientation and femtosecond relaxation of spin-polarized holes in GaAs. *Phys. Rev. Lett.*, 89(14):146601, Sep 2002. 59, 78

[JG89] R. O. Jones and O. Gunnarsson. The density functional formalism, its applications and prospects. *Rev. Mod. Phys.*, 61(3):689, Jul 1989. 64

[KS65] W. Kohn and L. J. Sham. Self-consistent equations including exchange and correlation effects. *Phys. Rev.*, 140(4A):A1133–A1138, Nov 1965. 10

[KS97] Hiroyuki Kageshima and Kenji Shiraishi. Momentum-matrix-element calculation using pseudopotentials. *Phys. Rev. B*, 56(23):14985, Dec 1997. 64, 78

[LA89] Zachary H. Levine and Douglas C. Allan. Linear optical response in silicon and germanium including self-energy effects. *Phys. Rev. Lett.*, 63(16):1719–1722, Oct 1989. 12

[LA91] Zachary H. Levine and Douglas C. Allan. Optical second-harmonic generation in III-V semiconductors: Detailed formulation and computational results. *Phys. Rev. B*, 44(23):12781–12793, Dec 1991. 12

[lam] The bulk analog of the phenomenon we discuss here was studied in the Ref. [LSSvD99]. 34

[Lam68] Georges Lampel. Nuclear dynamic polarization by optical electronic saturation and optical pumping in semiconductors. *Phys. Rev. Lett.*, 20(10):491, Mar 1968. 56, 76

[las] For instance in M. Alouani and J.M. Wills, Phys. Rev. B. **54**, 2480 (1996), it is found that the non simultaneous fulfilment of both the $f$-sum rule and the sum rule satisfied by the imaginary part of the linear dielectric function is an indication of the limitation for the scissors Hamiltonian. Indeed they concluded that the scissors correction well describes the low-lying excited states that include the $E_1$ and $E_2$ bulk critical-points, and that the higher excited states are better described by the LDA Hamiltonian alone. However, they used the usual procedure to scissors the linear response. In view of the new (and correct) way of including the scissored Hamiltonian, the sum rules for both the linear and the nonlinear response ought to be reconsidered to understand their possible implications in the optical response. 14

[Lax01] Melvin Lax. *Symmetry Principles in Solid State and Molecular Physics*. Dover Publications, 2001. Chap. 10. 97

[LDE+00] D. Lim, M. C. Downer, J. G. Ekerdt, N. Arzate, Bernardo S. Mendoza, V. I. Gavrilenko, and R. Q. Wu. Optical second harmonic spectroscopy of boron-reconstructed si(001). *Phys. Rev. Lett.*, 84(15):3406–3409, Apr 2000. 34

[Lev94] Zachary H. Levine. Optical second-harmonic susceptibilities: Frequency-dependent formulation with results for GaP and GaAs. *Phys. Rev. B*, 49(7):4532–4538, Feb 1994. 6

[LSHB05] R. Leitsmann, W. G. Schmidt, P. H. Hahn, and F. Bechstedt. Second-harmonic polarizability including electron-hole attraction from band-structure theory. *Phys. Rev. B*, 71(19):195209, May 2005. 6, 23, 27

[LSSvD99] N. Laman, A. I. Shkrebtii, J. E. Sipe, and H. M. van Driel. Quantum interference control of currents in CdSe with a single optical beam. *Applied Physics Letters*, 75(17):2581–2583, 1999. 46, 47, 94

[MAVN08] Bernardo S. Mendoza, N. Arzate, and R.A. Vázquez-Nava. Theoretical study of the optical response of the adsorption of Sb on the GaAs(110) surface. *phys. stat. sol. (c)*, 5(8):2604–2609, 2008. 36

[MGDS98] Bernardo S. Mendoza, Andrea Gaggiotti, and Rodolfo Del Sole. Microscopic theory of second harmonic generation at si(100) surfaces. *Phys. Rev. Lett.*, 81(17):3781–3784, Oct 1998. 7

[MNAS06] Bernardo S. Mendoza, F. Nastos, N. Arzate, and J. E. Sipe. Layer-by-layer analysis of the linear optical response of clean and hydrogenated Si(100) surfaces. *Phys. Rev. B*, 74(7):075318, 2006. 23, 25, 26, 36, 37, 38, 41, 42, 48, 56, 58, 59, 64, 78

[MPODS01] Bernardo S. Mendoza, Maurizia Palummo, Giovanni Onida, and Rodolfo Del Sole. Ab initio calculation of second-harmonic-generation at the Si(100) surface. *Phys. Rev. B*, 63(20):205406, April 2001. 7

[MSM04] J.E. Mejía, C. Salazar, and B.S. Mendoza. Layer-by-layer analysis of second harmonic generation at a simple surface. *Revista Mexicana de Física*, 50(2):134–139, Apr 2004. 36

[MZ84] F. Meier and B. P. Zakharchenya. *Optical Orientation, Modern Problems in Condensed Matter Physics.* North Holland, 1984. 60

[nas] F. Nastos and J.E. Sipe, in preparation. 34, 35, 97

[NBS03] Ali Najmaie, R. D. R. Bhat, and J. E. Sipe. All-optical injection and control of spin and electrical currents in quantum wells. *Phys. Rev. B*, 68(16):165348, Oct 2003. 60, 97

[NOSS05] F. Nastos, B. Olejnik, K. Schwarz, and J. E. Sipe. Scissors implementation within length-gauge formulations of the frequency-dependent nonlinear optical response of semiconductors. *Phys. Rev. B*, 72(4):045223, 2005. 7, 11, 12, 15, 20, 22, 24, 26, 27, 29, 34, 35, 42, 65, 78, 97

[nota] The crystal class of GaAs, F-43m, gives only one independent component for the susceptibility tensor $\chi^{abc}$, i.e. $\chi^{xyz} = \chi^{zxy} = \chi^{yzx}$. The intrinsic permutation symmetry $\chi^{abc} = \chi^{acb}$ is satisfied. 24

[notb] We have taken $E_{\text{mod}} = a + bE_{\text{orig}}$, where $a$ and $b$ are fitted such that the theoretical values of the bulk critical points $E_1$ and $E_2$ of the linear response coincide with the experimental values of $E_1 = 2.91$ eV and of $E_2 = 4.96$ eV.[BD03]. 27, 28

[notc] For example, in the CW limit $J^a_{sh} \propto \cos(\phi_b - \phi_c)$ while $dJ^a_{inj}/dt \propto \sin(\phi_b - \phi_c)$, where $E^{b,c}(\omega) = |E^{b,c}(\omega)|e^{i\phi_{b,c}}$.[NOSS05, nas]. 35

[notd] One has to add the $\mathbf{k}$ and $-\mathbf{k}$ terms in the integral over $\mathbf{k}$, and use following results from time reversal symmetry,[Lax01, NBS03] $\omega_n(-\mathbf{k}) = \omega_n(\mathbf{k})$, $r_{nm}(-\mathbf{k}) = r_{mn}(\mathbf{k})$, $\mathcal{R}_{nm}(-\mathbf{k}) = \mathcal{R}_{mn}(\mathbf{k})$ and $S^a_{mn}(-\mathbf{k}) = -S^a_{nm}(\mathbf{k})$. 60

[note] One has to use Eq. (4.11) and Eq. (4.9) with $\mathcal{R}^{\ell,a}_{nm} \to r^a_{nm}$ to get $\xi^{B,bc}_{\rm i}$ and $\zeta^{B,abc}_{\rm i}$, respectively, where the calculation is done for a "true" bulk system. 62

[notf] Since in equilibrium there is an equal population of spin-up and spin-down electrons, the excess of optically injected spins, accounted for by $\mathcal{D}^z$, should be added to the existing population. 80

[notg] In the continuous limit of $\mathbf{k}$ we have that $(1/\Omega)\sum_{\mathbf{k}} \to \int d^3k/(8\pi^3)$. 80

[NRSM+07] F. Nastos, J. Rioux, M. Strimas-Mackey, Bernardo S. Mendoza, and J. E. Sipe. Full band structure LDA and $\mathbf{k}\cdot\mathbf{p}$ calculations of optical spin injection. *Phys. Rev. B*, 76(1):205113, Jul 2007. 41, 56, 58, 60, 61, 63, 68, 72, 74, 76, 77, 82

[Pan82] K. C. Pandey. Reconstruction of semiconductor surfaces: Buckling, ionicity, and $\pi$-bonded chains. *Phys. Rev. Lett.*, 49(3):223, Jul 1982. 44, 65

[PODSS98] Olivia Pulci, Giovanni Onida, Rodolfo Del Sole, and Anatoli J. Shkrebtii. Ab initio calculation of the reflectance anisotropy of gaas(110). *Phys. Rev. B*, 58(4):1922–1927, Jul 1998. 23, 25

[RDSCP94] Lucia Reining, R. Del Sole, M. Cini, and Jiang Guo Ping. Microscopic calculation of second-harmonic generation at semiconductor surfaces: As/Si(111) as a test case. *Phys. Rev. B*, 50(12):8411–8422, Sep 1994. 7

[Ric96] W. Richter. Reflectance anisotropy spectroscopy and other anisotropy based spectroscopies. *World Scientific*, 81:2013, 1996. 34

[RL99] M. Rohlfing and S. G. Louie. Optical reflectivity of the Si(1 1 1)-(2 × 1) surface-the role of the electron-hole interaction. *physica status solidi (a)*, 175(1):17–22, 1999. 36, 44, 65

[RLS98] Sergey N. Rashkeev, Walter R. L. Lambrecht, and Benjamin Segall. Efficient ab initio method for the calculation of frequency-dependent second-order optical response in semiconductors. *Phys. Rev. B*, 57(7):3905–3919, Feb 1998. 6, 27

[RN91] A. J. Read and R. J. Needs. Calculation of optical matrix elements with nonlocal pseudopotentials. *Phys. Rev. B*, 44(23):13071, Dec 1991. 64, 78

[Sau96] E.G. Sauter. *Nonlinear Optics*. John Wiley, 1996. 40

[SCC+87] Selci, F. Ciccacci, A. Cricenti, A. C. Felici, C. Goletti, and P. Chiaradia. Polarization dependence of optical transitions in GaP(1 1 0) and GaAs(1 1 0) surfaces studied with surface differential reflectivity. *Solid State Communications*, 62(8):833–834, Jun 1987. 36

[SDAD03] S. Sharma, J. K. Dewhurst, and C. Ambrosch-Draxl. Linear and second-order optical response of III-V monolayer superlattices. *Phys. Rev. B*, 67(16):165332, Apr 2003. 7

[SS00] J. E. Sipe and A. I. Shkrebtii. Second-order optical response in semiconductors. *Phys. Rev. B*, 61(8):5337–5352, Feb 2000. 15, 34, 35, 37, 40, 53

[SSP98] J.E. Sipe, A.I. Shkrebtii, and O. Pulci. Issues concerning the calculation of the optical response of semiconductors. *phys. stat. sol (a)*, 170(2):431–442, 1998. 38, 43

[Sta71] Anthony F. Starace. Length and velocity formulas in approximate oscillator-strength calculations. *Phys. Rev. A*, 3(4):1242–1245, Apr 1971. 23

[Stu92] Paul J. Sturman. *Photovoltaic and Photo-refractive Effects in Noncentrosymmetric Materials*. CRC, 1992. 35

[tur] Stefan Turneaure, private communication. 76

[WMCF05] P. Weightman, D.S. Martin, R.J. Cole, and T. Farrell. Reflection anisotropy spectroscopy. *Rep. Prog. Phys.*, 68:1251, 2005. 34

[XBC+02] X.Gonze, J.-M. Beuken, R. Caracas, F. Detraux, M. Fuchs, G.-M. Rignanese, L. Sindic, M. Verstraete, G. Zerah, F. Jollet, M. Torrent, A. Roy, M. Mikami, Ph. Ghosez, J.-Y. Raty, and D.C. Allan. First-principles computation of material properties : the abinit software project. *Computational Materials Science*, 25:478, 2002. (URL http://www.abinit.org). 41, 63

[ZFS04] Igor Zutic, Jaroslav Fabian, and S. Das Sarma. Spintronics: Fundamentals and applications. *Reviews of Modern Physics*, 76(2):323, 2004. 76